CDF/ANAL/BOTTOM/CDFR/11106
Version 4.0
September 4, 2014

Measurement of effective-lifetime CP-violating asymmetry in two-body charm meson decays

A. Di Canto[2], S. Leo[1], P. Maestro[3], K. Pitts[1], and D. Tonelli[2]

[1]University of Illinois at Urbana-Champaign; [2]CERN; [3]Università di Siena

Abstract

We report on a search for indirect CP violation in $D^0 \to \pi^+\pi^-$ and $D^0 \to K^+K^-$ decays using the full Run II data set, corresponding to $9.7\,\text{fb}^{-1}$ of integrated luminosity and collected by the trigger on displaced tracks. By fitting the signal yields as functions of decay time, we measure in each decay mode the asymmetry between the effective lifetimes of charm and anticharm decays, A_Γ, exploiting the strong $D^{\star+} \to D^0\pi^+$ decays ("$D^\star$ tag") to identify the flavor of the charmed meson at production time. The results, $A_\Gamma(\pi^+\pi^-) = \left[-0.1 \pm 1.8\ (stat.) \pm 0.3\ (syst.)\right] \times 10^{-3}$, $A_\Gamma(K^+K^-) = \left[-1.9 \pm 1.5\ (stat.) \pm 0.4\ (syst.)\right] \times 10^{-3}$, are among the most precise measurements to date and are consistent with CP symmetry.

1 Introduction

Nonconservation of charge-parity (CP) symmetry has been extensively tested in decays of neutral and charged K and B mesons. Less information is available for D mesons. Only recently the experimental precision has reached the 10^{-3} level that may allow first discrimination between standard model (SM) or non-SM manifestations of the phenomenon. To date, no observation of CP violation has been reported in charm decays [1]. In the SM CP violation in charm decays is predicted to be negligibly small, since the dynamics of these decays, at leading order, only involves the first two quark generations [2].

1.1 Phenomenology of CP violation in neutral D mesons

Neutral D mesons are linear combinations of two eigenstates, $|D_{1,2}\rangle = p\,|D^0\rangle \pm q\,|\overline{D}^0\rangle$ (where p and q are complex parameters satisfying $|p|^2 + |q|^2 = 1$), that have well defined masses, $m_{1,2}$, and widths, $\Gamma_{1,2}$. Hence, $D^0 - \overline{D}^0$ mixing occurs in the case that at least one of the parameters $x = (m_1 - m_2)\Gamma$ and $y = (\Gamma_1 - \Gamma_2)/2\Gamma$ (where $\Gamma = (\Gamma_1 + \Gamma_2)/2 = 1/\tau$) is different than zero.

A neutral D meson decays to a multi-particle final state f and/or to its CP-conjugate $\bar{f}$ through the following decay amplitudes:

$$A_f = \langle f|\mathcal{H}|D^0\rangle, \qquad \overline{A}_f = \langle f|\mathcal{H}|\overline{D}^0\rangle, \qquad A_{\bar{f}} = \langle \bar{f}|\mathcal{H}|D^0\rangle, \quad \overline{A}_{\bar{f}} = \langle \bar{f}|\mathcal{H}|\overline{D}^0\rangle,$$

where $\mathcal{H}$ is the decay Hamiltonian.

As mixing and decay can interfere, it is useful to also define:

$$\lambda_f = \frac{q}{p}\,\frac{\overline{A}_f}{A_f}.$$

The time–dependent decay rate for $D^0 \to f$ and $\overline{D}^0 \to f$ can then be written as

$$\frac{d\Gamma}{dt}(D^0(t) \to f) \propto |A_f|^2 \Bigg[(1 - |\lambda_f|^2)\cos\left(\frac{xt}{\tau}\right) + (1 + |\lambda_f|^2)\cosh\left(\frac{yt}{\tau}\right) - 2\Im\mathrm{m}(\lambda_f)\sin\left(\frac{xt}{\tau}\right) + 2\Re\mathrm{e}(\lambda_f)\sinh\left(\frac{xt}{\tau}\right)\Bigg];$$

$$\frac{d\Gamma}{dt}(\overline{D}^0(t) \to f) \propto |\bar{A}_f|^2 \Bigg[(1 - |\lambda_f^{-1}|^2)\cos\left(\frac{xt}{\tau}\right) + (1 + |\lambda_f^{-1}|^2)\cosh\left(\frac{yt}{\tau}\right) - 2\Im\mathrm{m}(\lambda_f^{-1})\sin\left(\frac{xt}{\tau}\right) + 2\Re\mathrm{e}(\lambda_f^{-1})\sinh\left(\frac{yt}{\tau}\right)\Bigg].$$

Decay rates to the CP–conjugate final state are obtained through the substitutions $A_f \to A_{\bar{f}}$ and $\overline{A}_f \to \overline{A}_{\bar{f}}$ in the above equations.

CP-violating effects occur in three different forms:

1. *CP* violation in the decay (or *direct CP* violation) if $|\overline{A}_{\bar{f}}/A_f| \neq 1$;

2. *CP* violation in the mixing if $|q/p| \neq 1$;

3. *CP* violation in the interference between a decay without mixing, $D^0 \to f$, and a decay following mixing, $D^0 \to \overline{D}^0 \to f$, if $\Im\mathrm{m}(\lambda_f) \neq 0$. This effect only occurs in decays to final states that are common to both D^0 and $\overline{D}^0$, including all *CP* eigenstates.

Phenomena of type 2 and 3 are collectively referred as manifestation of *indirect CP* violation.

1.2 Indirect *CP* violation in decays to *CP* eigenstates

Indirect *CP* violation can manifest itself through a time-dependent asymmetry between the rates of flavor-tagged charm decays to *CP* eigenstates,

$$A_{CP}(D^0 \to f;t) = \frac{d\Gamma(D^0(t) \to f)/dt - d\Gamma(\overline{D}^0(t) \to f)/dt}{d\Gamma(D^0(t) \to f)/dt + d\Gamma(\overline{D}^0(t) \to f)/dt}, \tag{1}$$

which, owing to the low mixing rate of charm mesons, can be approximated to first order in t/τ as the sum of two terms,

$$A_{CP}(D^0 \to f;t) \approx A_{CP}^{\mathrm{dir}}(D^0 \to f) + \frac{t}{\tau}\, A_{CP}^{\mathrm{ind}}(D^0 \to f) \quad (|x|,|y| \ll \tau/t) \tag{2}$$

where A_{CP}^{dir} and A_{CP}^{ind} represents direct and indirect *CP*-violating asymmetries, respectively:

$$A_{CP}^{\mathrm{dir}}(D^0 \to f) = \frac{1-\left|\overline{A}_f/A_f\right|^2}{1+\left|\overline{A}_f/A_f\right|^2}, \tag{3}$$

$$A_{CP}^{\mathrm{ind}}(D^0 \to f) = \frac{1}{2}\left[y\ \Re\mathrm{e}(\lambda_f - \lambda_f^{-1}) - x\ \Im\mathrm{m}(\lambda_f - \lambda_f^{-1})\right]. \tag{4}$$

It is worth to notice that the term A_{CP}^{ind} may receive also contributions from direct *CP* violation [3], which is measured to be small compared to the precision on A_{CP}^{ind} available so far [1].

Indirect *CP* violation would also manifest itself as a nonzero asymmetry between the effective lifetimes, $\hat{\tau}$, of D^0 and $\overline{D}^0$ mesons decaying to *CP* eigenstates:

$$A_{\Gamma}(D^0 \to f) = \frac{\hat{\tau}(\overline{D}^0 \to f) - \hat{\tau}(D^0 \to f)}{\hat{\tau}(\overline{D}^0 \to f) + \hat{\tau}(D^0 \to f)}. \tag{5}$$

Here, effective lifetimes refer to lifetimes measured using a signle-exponential model in a specific decay mode where in general also mixing can occur. It can be shown with simple algebra that $A_{CP}^{\mathrm{ind}} = -A_{\Gamma}$.

Measuring indirect *CP* violation through the first order t/τ approximation of Eq. (2), or equivalently through Eq. (5), provides a sensitive null test of the SM. Since the SM predicts $A_\Gamma < 10^{-4}$ [2], any measurement of a significant nonzero value could suggest CP violating contributions from possible non-SM sources. In the SM, A_Γ is universal for all final states with same CP-parity, but again contribution to new physics processes may lead to different result. To date, all experiments report A_Γ values consistent with CP symmetry at the few permil level [1]. The Belle and BaBar collaborations combined the K^+K^- and $\pi^+\pi^-$ CP–even final states, reporting $A_\Gamma = (-0.3 \pm 2.0 \pm 0.8) \times 10^{-3}$ [4] and $A_\Gamma = (0.9 \pm 2.6 \pm 0.6) \times 10^{-3}$ [5], respectively. The most precise results have been reported by the LHCb collaboration separately for the two channels: $A_\Gamma(\pi^+\pi^-) = (0.33 \pm 1.06 \pm 0.14) \times 10^{-3}$ and $A_\Gamma(K^+K^-) = (-0.35 \pm 0.62 \pm 0.12) \times 10^{-3}$ [6]. Any independent measurement of comparable precision could further constrain the phenomenological bounds and improve the knowledge of CP violation in the charm sector.

1.3 Overview of the measurement

Singly–Cabibbo–suppressed decays into CP–eigenstates, such as $D^0 \to \pi^+\pi^-$ and $D^0 \to K^+K^-$ (collectively referred to as $D^0 \to h^+h^-$) are convenient channels for pursuing a measurement of lifetime asymmetry. Their final states can be fully reconstructed, providing a precise determination of the decay time, and the decays have significant signal yields and moderate backgrounds, allowing for reduced systematic uncertainties. With the full data set of $9.7\,\mathrm{fb}^{-1}$ of data, CDF can aim to a sensitivity of $\mathcal{O}(10^{-3})$, comparable with other experiments' sensitivities. While the decay-time distribution is biased by the online selection on impact parameters and transverse decay lengths, the effect of the bias cancels to a high level of accuracy in the asymmetry between distributions associated with the same final state and any residual effects can be checked against in control samples with similar kinematic properties.

In order to extract A_Γ, we determine separately the yields of primary $D^0 \to h^+h^-$ and $\overline{D}^0 \to h^+h^-$ decays as functions of reconstructed D decay time. The analysis uses only candidates populating a narrow range centered around the known D^0 meson mass. The flavor at production is identified by the charge of the low-momentum pion in the strong-interaction decay $D^{\star +} \to D^0\pi^+$. We fit the $D^0\pi$ mass distribution of events restricted to each decay time bin and meson flavor. The results of this fit are used to form the impact parameter distribution of signal-only D decays, from which the yield of primary D decays is extracted in each bin and for each flavor. This allows a statistical rejection of charm mesons originated from b–hadron decays (secondary D), whose decay-time distribution is biased by the additional decay length of the b–hadron. We combine the primary D signal yields resulting from the impact-parameter fit into an asymmetry, which is fit with the function

$$A(t) = \frac{N_{D^0}(t) - N_{\bar{D}^0}(t)}{N_{D^0}(t) + N_{\bar{D}^0}(t)} \approx A(0) - \frac{t}{\tau} A_\Gamma, \tag{6}$$

where the asymmetry at $t = 0$, $A(0)$, includes contributions from the direct CP violation and any possible detector-induced spurious asymmetries, which is assumed to be constant versus decay time. The size of a possible decay-time dependence of the detector asymmetry is constrained using high–statistics control samples of Cabibbo–favored $D^0 \to K^-\pi^+$ decays where CP violation is not present. Several portions of the analysis such as the sample selection, background composition, and fit model are inherited from previous measurements of time-integrated CP asymmetries performed using the same samples [7].

We describe the sample selection in Sec. 2 and the fit strategy in Secs. 3–5. Systematic uncertainties and further checks are discussed in Sec. 6 before the final results are presented in Sec. 7.

2 Sample selection

We use the whole CDF Run II data set, corresponding to about $9.7\,\text{fb}^{-1}$ of integrated luminosity after applying standard good runs requirements (goodrun list version 45, with no requirements on calorimeter and muon bits). The online data selection follows requirements imposed by the `B_CHARM` trigger paths, which accept events based on the presence of pairs of charged particles originated in a space-point displaced from the beam.

In the offline reconstruction, pairs of tracks consistent with those that have fired the trigger are combined with charged pion mass assignments to reconstruct neutral charm decay candidates. These are then combined with a low–momentum charged particle with pion mass hypothesis ("soft-pion", π_s) to form a $D^{\star +}$ (or $D^{\star -}$) candidate. The flavor of the charmed meson is unambiguously determined from the charge of the pion in the strong $D^{\star +} \to D^0\pi_s^+$ (or $D^{\star -} \to \overline{D}^0\pi_s^-$) decay.

To further increase the signal-to-background ratio, while fitting the decay topology, the D^* vertex position is constrained to lie on the beam-line. As the D^* mass resolution is dominated by the uncertainties on the soft pion's track parameters, this additional constraint provides an improvement of about 25% in signal mass resolution, as shown in Fig. 1. The resulting increase in signal-to-background ratio, S/B, at the peak goes from ≈ 25 to ≈ 35.

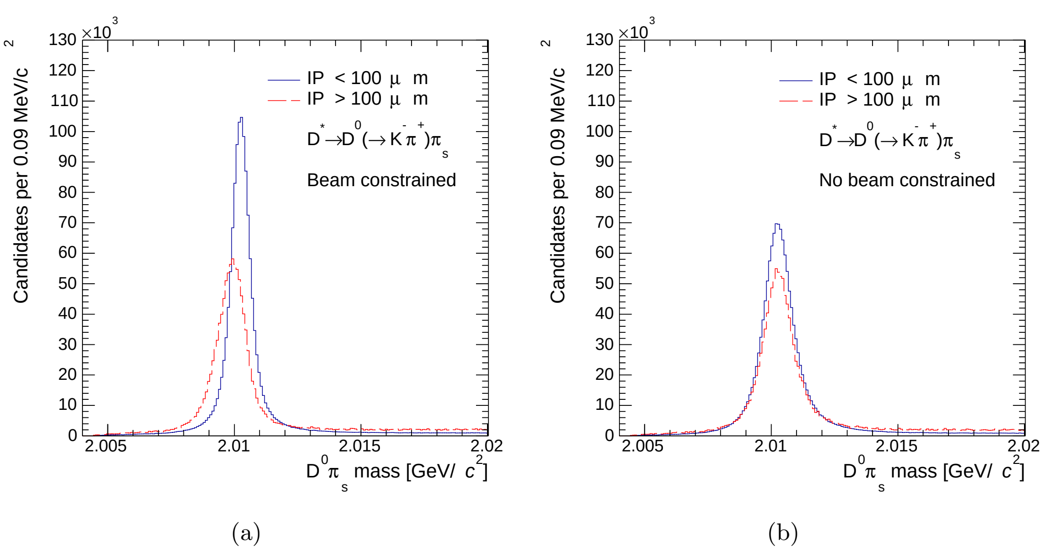

Figure 1: Comparison between $D^0\pi_s$–mass distributions of $D^{\star +} \to D^0(\to K^-\pi^+)\pi_s^+$ candidates reconstructed (a) with and (b) without beam constraint for different D^0 impact parameter requirements.

The beam-line constraint, however, distorts the $D^0\pi_s$–mass distribution as one can notice from the presence of an asymmetric low-mass tail which is not visible in the standard reconstruction (see Fig. 1). This low mass tail is caused by the background of secondary $D^\star$ mesons produced in the decay of a long-lived b-hadron which is well separated by the primary vertex. For these events the primary vertex constraint causes a bias in the reconstructed mass since it moves the fitted vertex towards the primary interaction point, reducing the decay opening angle, which finally reflects in a smaller measured mass. Since the amount of secondaries increases with decay time, we expect to have a decay-time-dependent signal shape where the relative size of the low mass tail also increases with decay time. This is however not a concern for our measurement where we determine an asymmetry between candidates of different flavor and where, as detailed in the following section, the signal mass shape is determined from high-statistics extremely-clean distributions of $D^0 \to K^-\pi^+$ candidates, that are expected to be polluted by the same amount of secondary background.

Tracks	Units	Requirement
Total silicon hits	–	≥ 3
Axial COT hits	–	≥ 10
Stereo COT hits	–	≥ 10
Total COT hits	–	≥ 30
p_T	GeV/c	> 2
$\lvert\eta\rvert$	–	< 1.2
Impact parameter	μm	$[100,\ 1000]$
D^0 candidates		
Decay time	τ	< 20
Transverse decay length (L_{xy})	μm	> 200
Scalar sum of p_T	GeV/c	> 4.5
χ^2 of the 3D vertex fit	–	< 30
χ^2_{xy} of the 2D vertex fit	–	< 15
Azimuthal separation	degrees	$[2^\circ,\ 90^\circ]$
$M(\pi\pi)$	GeV/c^2	$[1.2,\ 2.4]$
Soft pion for D^* candidates		
Silicon hits	–	≥ 1
COT hits	–	≥ 30
p_T	MeV/c	> 400
$\lvert\eta\rvert$	–	< 1.2
Impact parameter	μm	< 600
$\lvert z_0\rvert$ from primary vertex	cm	< 1.5
$M(D^0\pi_s)$	GeV/c^2	< 2.03

Table 1: Summary of the selection cuts for $D^\star$–tagged $D^0 \to h^+h^-$ decays.

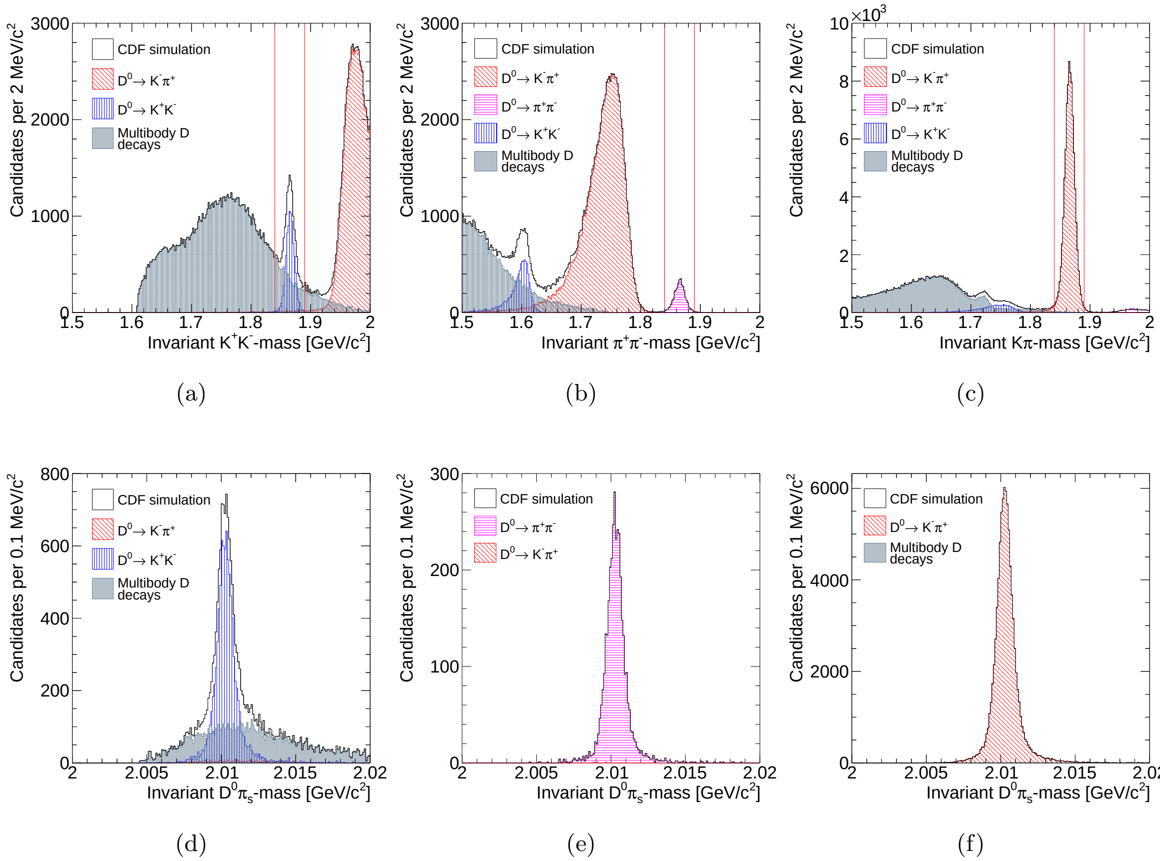

Figure 2: Distributions of K^+K^- (a), $\pi^+\pi^-$ (b) and $K^-\pi^+$ (c) mass for a simulated sample of inclusive charm decays. Regions used to define the three samples are indicated by two vertical lines. Distributions of $M(D^0\pi_s)$ for the selected K^+K^- (d), $\pi^+\pi^-$ (e) and $K^-\pi^+$ (f) mass regions.

The offline criteria used to select the $D^\star \to D^0\pi_s$ candidates are summarized in Tab. 1 and follow what used in Ref. [7]. In addition, we retain only candidates having decay time $t = L_{xy}m_{D^0}/p_T$, with m_{D^0} being the known D^0 mass [8], smaller than 20 D^0 lifetimes [8].

The three D^0 decay channels considered ($D^0 \to K^+K^-$, $D^0 \to \pi^+\pi^-$ and $D^0 \to K^-\pi^+$) are separated by requiring the selected D^0 candidates to have the relevant two-body mass within about 3σ of the known D^0 mass ($|M(h^+h'^-) - m_{D^0}| < 24\,\text{MeV}/c^2$), as shown for simulated events in Fig. 2, where it is also plot the expected $D^0\pi_s$ mass distribution for the selected candidates.

After all selection cuts, we reconstruct a total of ≈ 1.25M $D^0 \to K^+K^-$, ≈ 590k $D^0 \to \pi^+\pi^-$ and ≈ 13M $D^0 \to \pi^+K^-$ $D^\star$–tagged signal decays. These allow to define 30 variable-width bins in decay time, each with sufficient number of signal candidates, that are then used for the measurement of the decay-time-dependent asymmetry.

3 Mass fit

The time- and flavor-integrated[1] $D^0\pi_s$–mass distributions for the K^+K^-, $\pi^+\pi^-$ and $K^-\pi^+$ samples are shown in Fig. 3. A clean D^* signal is visible superimposed on background components that are different in each D^0 channel. In $D^0 \to \pi^+\pi^-$ and $D^0 \to K^-\pi^+$ decays, the background is mainly due to random pions associated with a real D^0 candidate. In the $D^0 \to K^+K^-$ case, there is also a substantial contribution from mis–reconstructed multibody neutral charmed decays that yields a broader enhancement underneath the signal peak.

The D^* mass signal is described by a Johnson function [9],

$$\mathscr{J}(x|\mu,\sigma,\delta,\gamma) = \frac{1}{\mathscr{N}_J}\, \frac{e^{-\frac{1}{2}\left[\gamma\, +\, \delta\ \sinh^{-1}\left(\frac{x-\mu}{\sigma}\right)\right]^2}}{\sqrt{1+\left(\frac{x-\mu}{\sigma}\right)^2}},$$

which reproduces satisfactorily the asymmetric tails and two Gaussians,

$$\mathscr{G}(x|\mu,\sigma) = \frac{1}{\mathscr{N}_G}\ e^{\frac{1}{2}\left(\frac{x-\mu}{\sigma}\right)^2},$$

which represent the core of the distribution:

$$\begin{aligned}\wp_{\rm sgn}(m|\vec{\theta}_{sgn}) = f_J \mathscr{J}(m|m_{D^*}+\mu_J,\sigma_J,\delta_J,\gamma_J) \\ + (1-f_J)\left[f_{G1}\mathscr{G}(m|m_{D^*}+\mu_{G1},\sigma_{G1})\right. \\ \left. +(1-f_{G1})\mathscr{G}(m|m_{D^*}+\mu_{G2},\sigma_{G2})\right].\end{aligned}$$

[1]Meaning summing D^0 and $\overline{D}^0$ together.

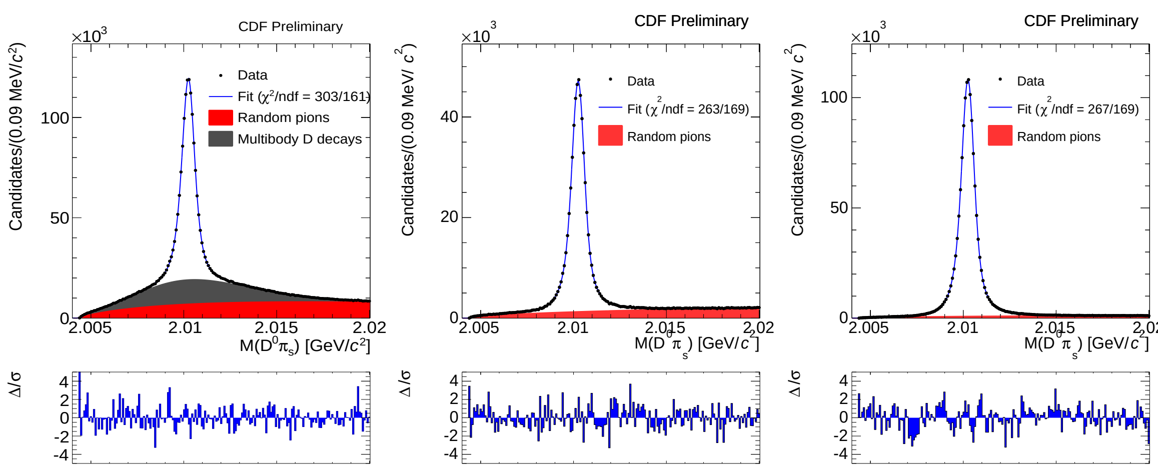

(a) (b) (c)

Figure 3: $D^0\pi_s$–mass distributions of the selected $D^* \to D^0\pi$ candidates for (a) $D^0 \to K^+K^-$, (b) $D^0 \to \pi^+\pi^-$ and (c) $D^0 \to K^-\pi^+$ decays (for the latter only 1/10th of the full statistics is used) in comparison with corresponding distributions from the simulated events.

The signal parameters $\vec{\theta}_{sgn}$ include the relative fraction, f_J, between the Johnson and the Gaussian components; the shift from the nominal $D^{*\pm}$ mass [8] of the Johnson distribution's core, μ_J, and the two Gaussians, $\mu_{G1(2)}$; the widths of the Johnson distribution's core, σ_J, and the two Gaussians, $\sigma_{G1(2)}$; the parameters δ_J and γ_J determine, instead, the asymmetry in the Johnson distribution's tails.

For the random pion background model, we use an empirical shape form extracted from data by forming an artificial random combination of a well-reconstructed D^0 meson from each event combined with pions from other events [7]:

$$\wp_{\rm bkg}(m|\vec{\theta}_{\rm bkg}) = \mathscr{B}(m|m_{D^0} + m_{\pi_s}, b_{\rm bkg}, c_{\rm bkg})$$

with

$$\mathscr{B}(x|a,b,c) = \frac{1}{\mathscr{N}_B}\ (x-a)^b e^{-c(x-a)}.$$

The total function used for the $D^0 \to \pi^+\pi^-$ and $D^0 \to K^-\pi^+$ fits is then

$$N_{\rm sgn}\wp_{\rm sgn}(m|\vec{\theta}_{\rm sgn}) + N_{\rm bkg}\wp_{\rm bkg}(m|\vec{\theta}_{\rm bkg}).$$

In the $D^0 \to K^+K^-$ fit, the additional background component from mis–reconstructed multibody decays is described by

$$\begin{aligned}\wp_{\rm mbd}(m|\vec{\theta}_{\rm mbd}) = f_{\rm mdb} J(m|m_{D^*} + \mu_{\rm mbd}, \sigma_{\rm mbd}, \delta_{\rm mbd}, \gamma_{\rm mbd}) \\ + (1 - f_{\rm mbd})\mathscr{B}(m|m_{D^0} + m_\pi, b_{\rm mbd}, c_{\rm mbd}).\end{aligned}$$

The total function used to fit the K^+K^- sample is then

$$N_{\rm sgn}\wp_{\rm sgn}(m|\vec{\theta}_{\rm sgn}) + N_{\rm bkg}\wp_{\rm bkg}(m|\vec{\theta}_{\rm bkg}) + N_{\rm mbd}\wp_{\rm mbd}(m|\vec{\theta}_{\rm mbd}).$$

Each function is defined only above the threshold value of $m_{D^0} + m_{\pi_s} \approx 2.0044\,{\rm GeV/c^2}$ [8] and is normalized in the fit range, which extends from the threshold up to $2.02\,{\rm GeV/c^2}$, through the coefficients $\mathscr{N}_J$, $\mathscr{N}_G$ and $\mathscr{N}_B$.

In each decay-time bin, and for each flavor, the $D^0\pi_s$ mass distribution is fit to determine the relative normalization between signal and background candidates. The shapes for the signal are determined separately for charm and anticharm events and in each decay-time bin by using the larger sample of $D^0 \to K^-\pi^+$ decays and fixed for the fit of the $\pi^+\pi^-$ and K^+K^- samples. The background shapes (random pions in the $\pi^+\pi^-$ sample and random pions plus multibody components in the K^+K^- sample) are allowed to float and so extracted directly from the fit on data, again independently in each decay-time bin and for each flavor.

Figure 4 reports examples of fit projections for the K^+K^- and $\pi^+\pi^-$ samples in the decay-time bin $2.00\tau < t < 2.08\tau$. Appendix A reports all the others.

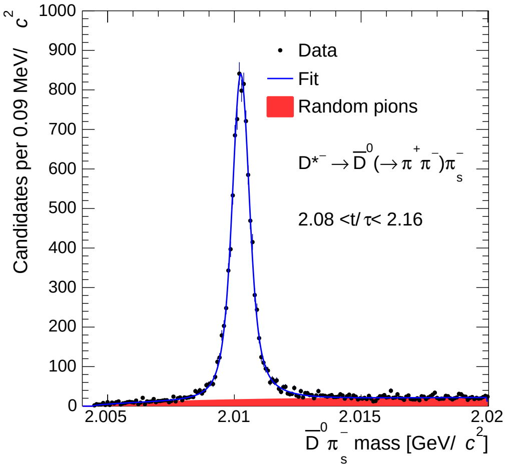

(a)

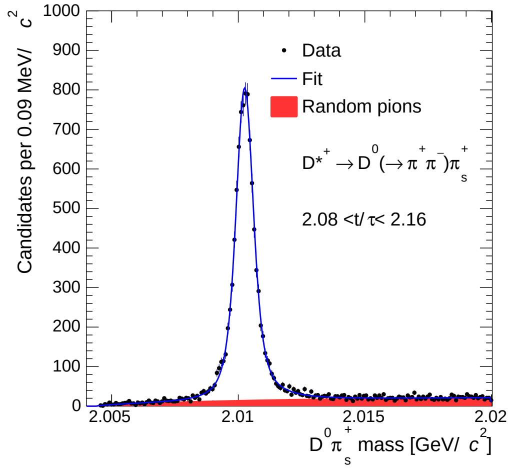

(b)

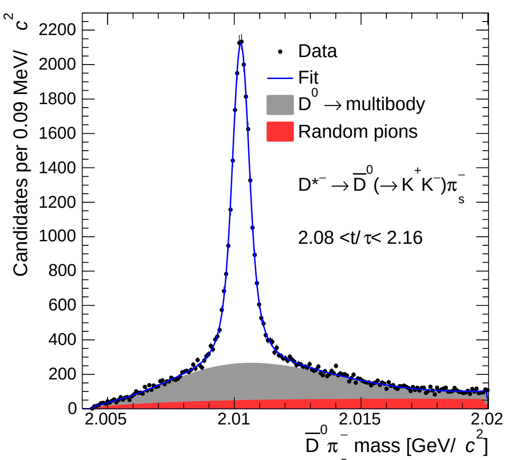

(c)

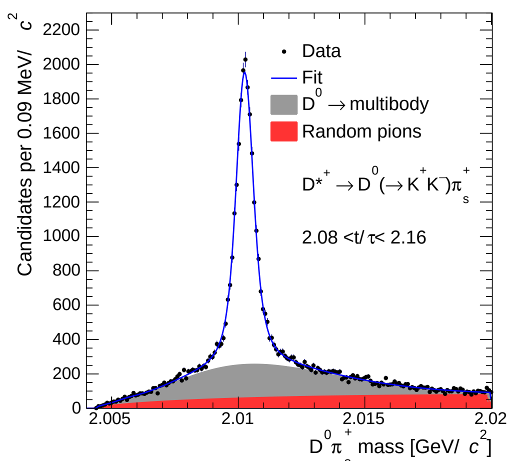

(d)

Figure 4: Example $D^0\pi_s$–mass distributions of (a) $D^{*-} \to \overline{D}^0(\to \pi^+\pi^-)\pi_s^-$, (b) $D^{*+} \to D^0(\to \pi^+\pi^-)\pi_s^+$, (c) $D^{*-} \to \overline{D}^0(\to K^+K^-)\pi_s^-$ and (d) $D^{*+} \to D^0(\to K^+K^-)\pi_s^+$ candidates restricted in the decay-time bin 11 ($2.00\tau < t < 2.08\tau$), with fit projections overlaid.

The results of this mass fit are used to estimate the amount of background in the signal region $|M(D^0\pi_s) - m_{D^*}| < 2.4\,\mathrm{MeV}/c^2$. Background candidates from sidebands are then normalized to that expected under the signal peak when constructing a background-subtracted distribution of D^0 impact parameter, which is then fit as described in the following section. As $D^0 \to \pi^+\pi^-$ and $D^0 \to K^+K^-$ decays are polluted by different background categories, different sidebands are choosen for the two decay modes. For $\pi^+\pi^-$ decay the main background polluting the signal region is made of random pions; the sideband is then defined as the high $D^0\pi_s$–mass region [2.015, 2.02] GeV/c^2. For K^+K^- decay the background polluting the signal region is made of both random pions and multibody charm decays; the sideband is then defined as the low K^+K^-–mass region $[m_{D^0} - 64\,\mathrm{MeV/c^2},\ m_{D^0} - 40\,\mathrm{MeV/c^2}]$ of the candidates within the $M(D^0\pi_s)$ signal window, where similar proportions of multibody and random pions events are observed [7].

4 Impact parameter fit

To determine the yields of genuine $D^\star$ decays produced in the primary interaction, we fit the signal-only D^0 impact parameter distribution separately for charm and anticharm and in each decay-time bin. The impact parameter of the neutral charmed meson is that determined when vertexing the D^0 decay only, prior to any $D^\star$ reconstruction (and thus without any beam-line constraint). This ensures a flavor-unbiased estimate of D^0 impact parameter, which makes the measurement of the yield asymmetry insensitive to possible charm-anticharm differences in the impact parameter distribution due to the presence of the soft pion.

The impact parameter shape for primary decays is described by a sum of two Gaussian distributions, as derived from flavor-integrated decays with $t < 1.18\tau$ (see Fig. 5). In this first decay-time bin the contamination from secondary decays (estimated to be $\sim 2\%$ using a simulation of inclusive $B \to DX$ decays) can be neglected because it would marginally bias the measurement, as these secondaries travel so little that they effectively looks very much like primary charm. The impact parameter distribution of primary decays is expected to be independent of decay time, being its width dominated by the transverse size of the luminous region. Hence, the shape extracted from the first bin is kept fixed and common to all other decay-time bins.

Contrarily, the impact parameter distribution of secondary decays is expected to depend on decay time, providing larger tails at larger values of t/τ. We then describe the secondary component by a sum of two Gaussian distributions with common means, where both widths

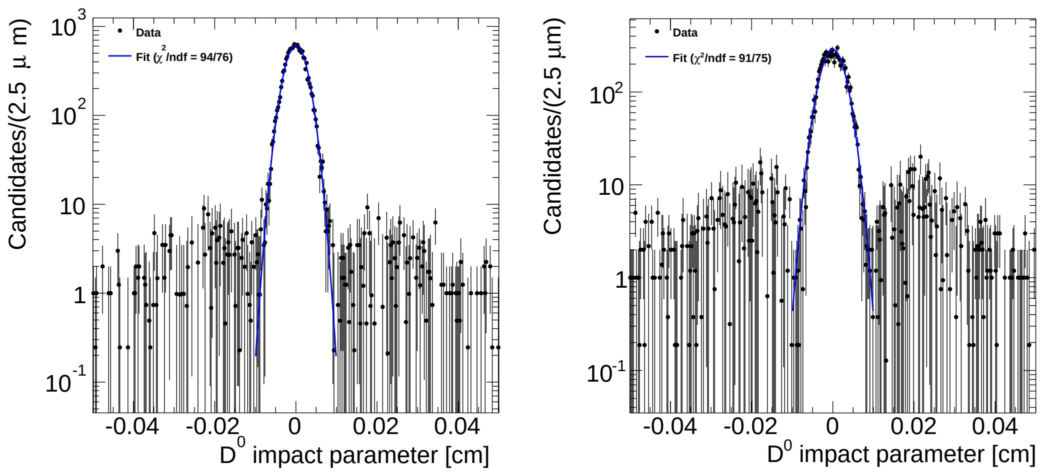

(a) (b)

Figure 5: Impact parameter distributions of flavor-integrated (a) $D^0 \to \pi^+\pi^-$ and (b) $D^0 \to K^+K^-$ candidates with $t < 1.18\tau$, with prompt-shape fit projection overlaid.

and the relative proportion of the two Gaussian functions are determined by the fit independently in each decay-time bin. This fitting strategy is inspired by Ref. [10].

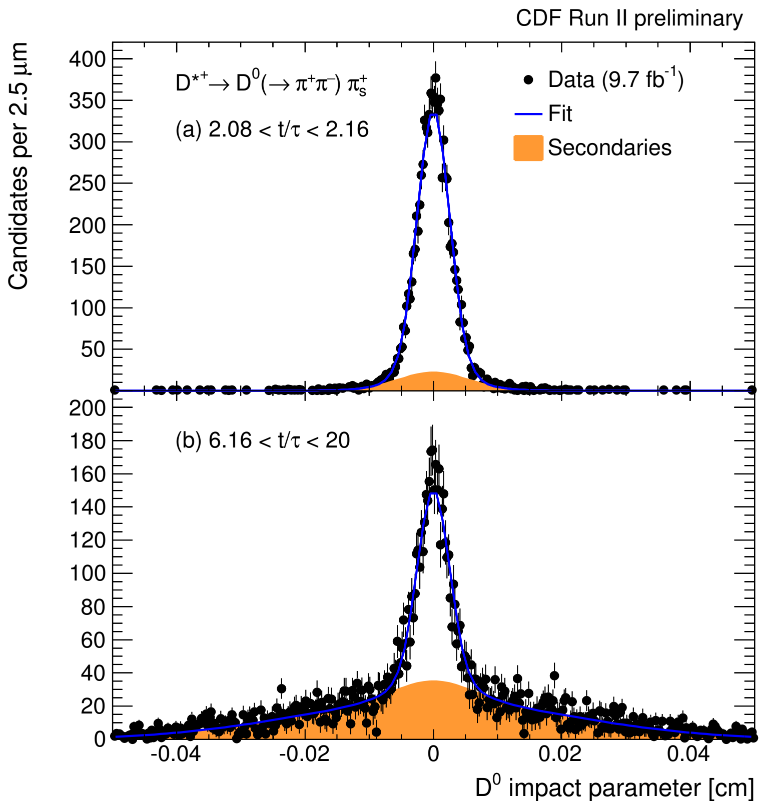

Figure 6: Example impact parameter fits of $D^{*+} \to D^0(\to \pi^+\pi^-)\pi_s^+$ candidates restricted in the decay-time bin (a) $2.08 < t/\tau < 2.16$ and (b) $6.16 < t/\tau < 20$, with fit projections overlaid.

Examples of impact parameter fit projections are shown in Fig. 6 for the $D^0 \to \pi^+\pi^-$ sample. All other impact parameter fit projections are reported in App. B.

5 Effective-lifetime asymmetry fit

The fit to the impact parameter distributions determines the events yields in each decay-time bin and for each flavor (see Tab. 2), which are used to form the asymmetry distribution versus decay time from where A_Γ is measured.

In each bin i the observed yield asymmetry A_i correspond to the integral of the time-dependent asymmetry of Eq. (6) over the corresponding normalized decay-time distribution for unmixed decays $D_i(t)$:

$$A_i = \int_{D_i} A(t)dt = A(0) - A_\Gamma \int D_i(t)\frac{t}{\tau}\ dt = A(0) - A_\Gamma \frac{\langle t \rangle_i}{\tau}. \quad (7)$$

Here $\langle t \rangle_i$ represents simply the average value of the decay time in bin i and defines the x-axis coordinate where the asymmetry point is plot in Fig. 7. As in Eq. (7) the integration is performed over the observed decay-time distribution in the bin, this procedure fully accounts for the non-uniform decay-time acceptance of the CDF detector and trigger.

We determine the values of $\langle t \rangle_i$ from the observed (sideband-subtracted) $D^0 \to K^-\pi^+$ decay-time distribution. Because of the much larger statistics of the $K^-\pi^+$ sample with respect to the K^+K^- and $\pi^+\pi^-$ ones, the statistical uncertainty on the determination of $\langle t \rangle_i$ can be neglected. By studying the variation of $\langle t \rangle_i$ in samples satisfying different requirements on the D^0 impact parameter, we found that the small contamination of secondary decays present can also be ignored.

The prompt signal yields, separately for different flavors and different final states, and the estimated $\langle t \rangle$ for each bin are reported in Tab. 2.

The time-dependent asymmetry is finally fit to Eq. (6) and the following values with statistical only uncertainties are determined:

$$A_\Gamma(K^+K^-) = (-1.89 \pm 1.49) \times 10^{-3};$$
$$A_\Gamma(\pi^+\pi^-) = (-0.11 \pm 1.81) \times 10^{-3}.$$

The data are also fit with a constant and the $\Delta\chi^2$ is used to quantify the compatibility with the null hypothesis. The date is found to be consistent with no indirect CP with p-values of 15% and 87% for K^+K^- and $\pi^+\pi^-$ decays, respectively.

The data and the fit projections are shown in Fig. 7. The $\approx -2\%$ offset with respect to zero is due to the known detector-induced asymmetry in the soft pion reconstruction efficiency, and is compatible with what estimated in Ref. [7].

Bin	$\langle t \rangle$	$N(\overline{D}^0 \to K^+K^-)$	$N(D^0 \to K^+K^-)$	$N(\overline{D}^0 \to \pi^+\pi^-)$	$N(D^0 \to \pi^+\pi^-)$
0	1.08995 ± 0.00018	$4\,207 \pm 100$	$4\,146 \pm 101$	$8\,198 \pm 104$	$8\,034 \pm 102$
1	1.25629 ± 0.00007	$10\,607 \pm 155$	$10\,054 \pm 152$	$10\,597 \pm 114$	$9\,994 \pm 110$
2	1.37196 ± 0.00005	$12\,729 \pm 166$	$11\,984 \pm 162$	$9\,983 \pm 110$	$9\,758 \pm 109$
3	1.47127 ± 0.00004	$16\,911 \pm 193$	$16\,183 \pm 185$	$11\,715 \pm 119$	$11\,153 \pm 116$
4	1.56054 ± 0.00003	$15\,906 \pm 187$	$14\,873 \pm 181$	$9\,836 \pm 109$	$9\,702 \pm 109$
5	1.64034 ± 0.00003	$17\,749 \pm 201$	$17\,007 \pm 195$	$10\,330 \pm 111$	$9\,851 \pm 109$
6	1.72023 ± 0.00003	$18\,655 \pm 210$	$17\,837 \pm 203$	$10\,491 \pm 112$	$10\,019 \pm 109$
7	1.80012 ± 0.00003	$19\,791 \pm 219$	$18\,988 \pm 213$	$10\,887 \pm 114$	$10\,308 \pm 111$
8	1.87998 ± 0.00003	$20\,475 \pm 221$	$19\,293 \pm 218$	$10\,683 \pm 113$	$10\,177 \pm 110$
9	1.96000 ± 0.00003	$19\,975 \pm 227$	$19\,199 \pm 223$	$10\,279 \pm 112$	$9\,985 \pm 110$
10	2.03990 ± 0.00003	$20\,492 \pm 225$	$19\,563 \pm 222$	$10\,117 \pm 111$	$9\,740 \pm 109$
11	2.11981 ± 0.00003	$20\,519 \pm 227$	$18\,969 \pm 222$	$9\,849 \pm 109$	$9\,634 \pm 108$
12	2.19973 ± 0.00003	$19\,547 \pm 229$	$18\,469 \pm 225$	$9\,628 \pm 108$	$8\,950 \pm 105$
13	2.28967 ± 0.00004	$24\,122 \pm 252$	$22\,211 \pm 246$	$11\,320 \pm 117$	$10\,885 \pm 111$
14	2.38962 ± 0.00004	$22\,780 \pm 247$	$21\,234 \pm 243$	$10\,648 \pm 114$	$10\,347 \pm 112$
15	2.48951 ± 0.00004	$21\,493 \pm 242$	$20\,229 \pm 238$	$9\,996 \pm 110$	$9\,560 \pm 108$
16	2.58945 ± 0.00004	$19\,993 \pm 238$	$19\,427 \pm 229$	$9\,401 \pm 107$	$9\,118 \pm 102$
17	2.69918 ± 0.00005	$22\,579 \pm 249$	$21\,612 \pm 242$	$10\,504 \pm 114$	$10\,058 \pm 110$
18	2.81922 ± 0.00005	$20\,812 \pm 243$	$19\,656 \pm 238$	$9\,520 \pm 109$	$9\,442 \pm 108$
19	2.93924 ± 0.00005	$19\,090 \pm 231$	$17\,967 \pm 228$	$8\,880 \pm 104$	$8\,326 \pm 102$
20	3.06884 ± 0.00006	$19\,764 \pm 242$	$19\,172 \pm 236$	$9\,348 \pm 107$	$9\,137 \pm 107$
21	3.20877 ± 0.00006	$18\,049 \pm 226$	$17\,846 \pm 224$	$8\,359 \pm 102$	$8\,049 \pm 100$
22	3.35843 ± 0.00007	$18\,438 \pm 229$	$17\,180 \pm 228$	$8\,681 \pm 104$	$8\,304 \pm 102$
23	3.52802 ± 0.00008	$17\,327 \pm 229$	$16\,626 \pm 225$	$8\,347 \pm 103$	$8\,225 \pm 103$
24	3.71737 ± 0.00009	$16\,058 \pm 226$	$15\,921 \pm 219$	$7\,960 \pm 101$	$7\,827 \pm 100$
25	3.92685 ± 0.00010	$14\,911 \pm 217$	$14\,468 \pm 211$	$7\,622 \pm 100$	$7\,230 \pm 98$
26	4.16566 ± 0.00012	$14\,250 \pm 213$	$13\,672 \pm 207$	$7\,445 \pm 100$	$7\,011 \pm 97$
27	4.61044 ± 0.00024	$20\,458 \pm 267$	$19\,479 \pm 259$	$11\,119 \pm 123$	$10\,657 \pm 121$
28	5.47981 ± 0.00044	$17\,171 \pm 250$	$16\,244 \pm 245$	$10\,344 \pm 125$	$9\,717 \pm 120$
29	7.40203 ± 0.00229	$12\,834 \pm 261$	$12\,420 \pm 252$	$9\,063 \pm 126$	$9\,022 \pm 125$

Table 2: Prompt D^0 yields for all decay-time bins.

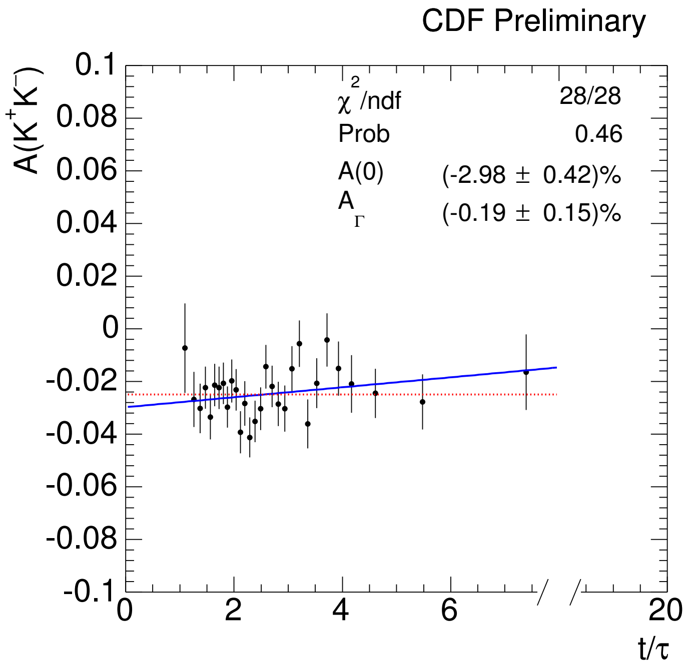

(a)

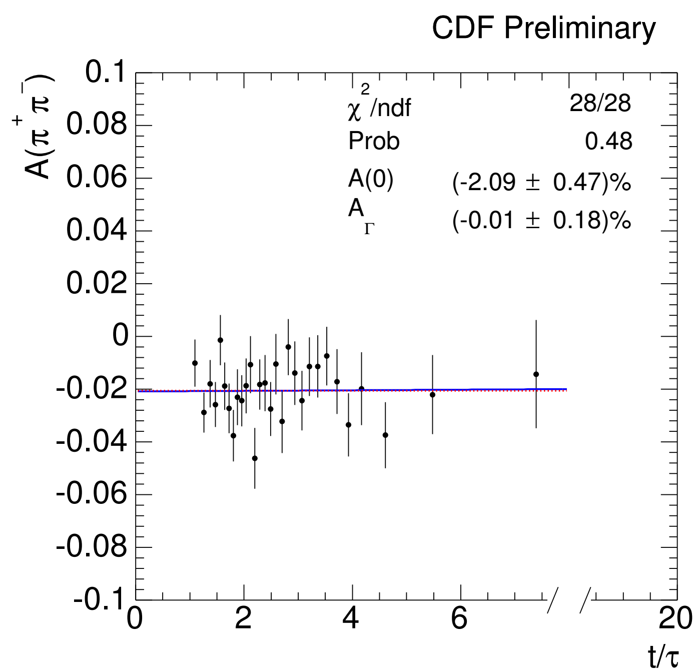

(b)

Figure 7: Time-dependent asymmetry from (a) $D^0 \to K^+K^-$ and (b) $D^0 \to \pi^+\pi^-$ candidates, with fit projections overlaid.

6 Systematic uncertainties

In the following we describe potential sources of systematic biases for the measurement and for each quantify a systematic uncertainty. A summary is then given in Tab. 3 before the final results are presented in Sec. 7.

6.1 Fit bias study

The fit procedure outlined in Secs. 3–5 is tested using data candidates where the flavor of the neutral D meson, instead of being determined by the charge of the soft pion, is randomly generated. A result compatible with $A_\Gamma = 0$ is expected in this data-based null test; any significant deviation from zero allows to assessing systematic uncertainties due to possible small biases.

Figure 8(a) reports the result for the $D^0 \to \pi^+\pi^-$ case, where, as expected, the slope resulting from the straight-line fit is found consistent with zero. Figure 8(b), shows the pull distribution resulting from 90 randomly-tagged $D^0 \to \pi^+\pi^-$ samples, proving that the measurement procedure is free of any bias and gives a proper estimation of the statistical uncertainty. These results are also valid for the $D^0 \to K^+K^-$ case. No systematic uncertainty is assigned.

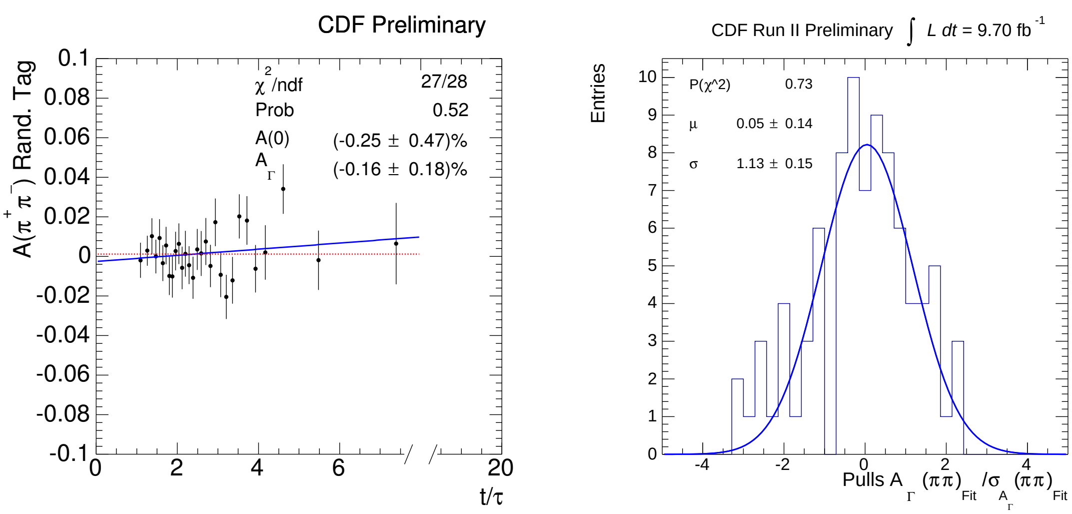

(a) (b)

Figure 8: (a) Time-dependent asymmetry from randomly-tagged $D^0 \to \pi^+\pi^-$ candidates. (b) Pull distributions resulting from 90 randomly-tagged samples.

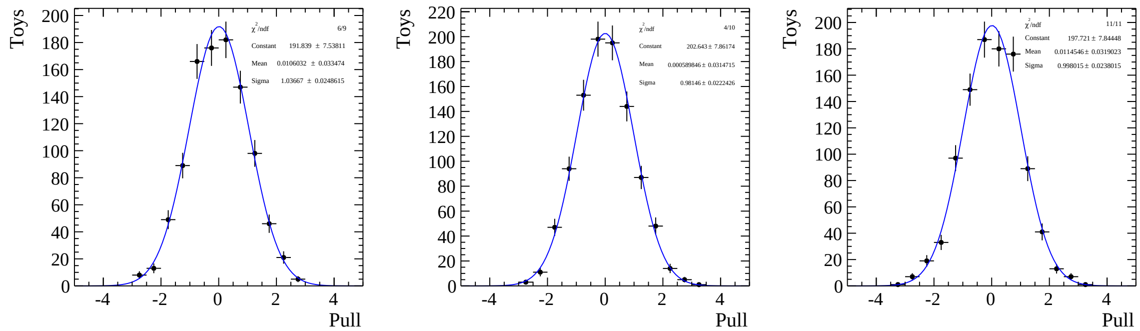

(a) (b) (c)

Figure 9: Pull distributions resulting from pseudoexperiments generated including the effect of decay-time resolution (0.19τ) and acceptance, and assuming A_Γ to be (a) -1%, (b) 0 and (c) $+1\%$.

6.2 Finite decay-time resolution

The time-dependent fit does not account for the finite decay-time resolution, as we assume that it can be neglected with our binning choice. This assumption is checked by fitting pseudoexperiments where only signal is generated and where the effect of both the decay-time resolution (corresponding to $\sigma_t \approx 0.19\tau$) and the decay-time acceptance, as derived from fully simulated $D^\star$-tagged $D^0 \to \pi^+\pi^-$ decays, is introduced. Figure 9 shows the pull distributions from 1 000 pseudoexperiments, each with about 600 000 signal events, and for $A_\Gamma = -1,\ 0,\ +1\%$. No bias is observed, then we conclude that neglecting the resolution has negligible impact on the determination of A_Γ e no systematic uncertainty is associated.

To account for a possible underestimation of the decay-time resolution in simulated events, we generated additional pseudoexperiments, using $\sigma_t = 0.4\tau$. The results, see Fig. 10, show that no significant bias would be visible even if the real resolution would be twice larger than in simulation.

6.3 Time-dependent detector-induced asymmetries

Detector-induced asymmetries that depend on the decay time could bias the result. Because the final state used in the D^0 reconstruction is common to the charm and anticharm samples and consists of a pair of opposite-sign charged particles of the same type, we expect no spurious asymmetry associated with the D^0 reconstruction. The only difference in the reconstruction concerns the presence of a positively-charged soft pion associated with the charm meson, and a negatively-charged soft pion for the anticharm meson. While percent level detection asymmetries do arise in the reconstruction of soft pions of opposite sign, these are

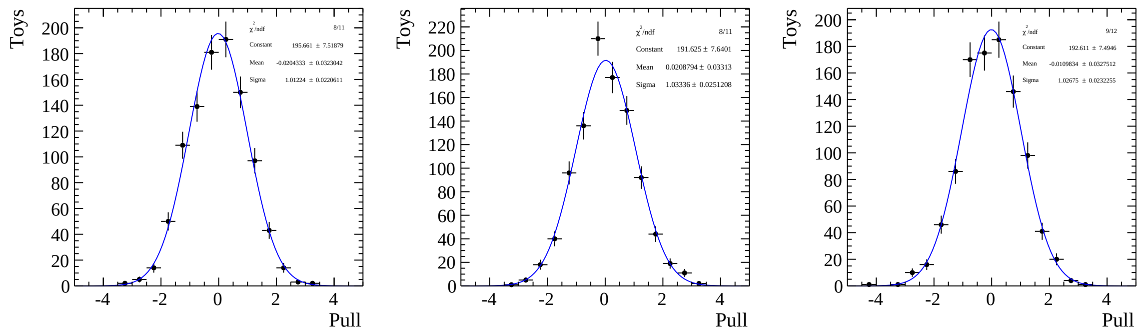

Figure 10: Pull distributions resulting from pseudoexperiments generated including the effect of decay-time resolution (0.4τ) and acceptance, and assuming A_Γ to be (a) -1%, (b) 0 and (c) $+1\%$.

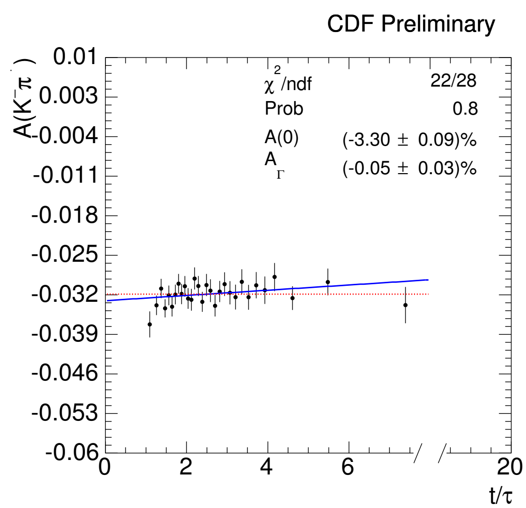

Figure 11: Time-dependent asymmetry from $D^0 \to K^-\pi^+$ candidates.

very unlikely to depend on the decay time of the charm candidate. However, to check against such effects, we perform the measurement on the sample of $D^{\star +} \to D^0(\to K^-\pi^+)\pi_s^+$ decays, where no *CP* violation occurs. Hence, the quantity A_Γ cannot be defined in a physically meaningful way and should be measured to be consistent with zero.

Figure 11 shows a straight-line fit to the asymmetry measured in $K^-\pi^+$ decays, showing no evidence of decay-time-dependent structures. The $\approx -3\%$ offset with respect to zero is constant as function of time and is attributed to the differences in detection of the D^0 daughters and to the soft pion reconstruction asymmetry [7].

Additionally, since we known that the soft pion detection asymmetry depends on mo-

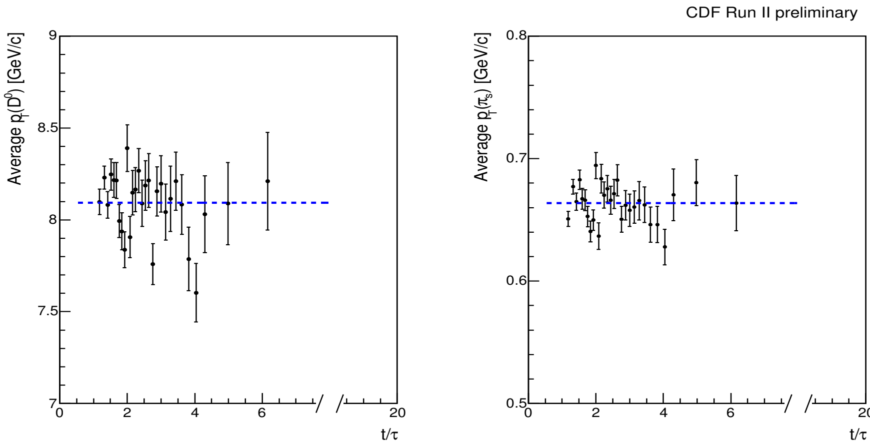

Figure 12: Average transverse momentum of D^0 and π_s candidates as function of D^0 decay time.

mentum [7], we looked for the presence of possible correlations between π_s/D^0 momentum and D^0 decay time directly in the $\pi^+\pi^-$ sample. Figure 12 shows the average D^0 and π_s momenta in the different decay-time bins of the analysis. No time-dependent structure is observed, proving that the momentum-dependent detection asymmetry of the soft pion cannot introduce any time-dependent effect.

6.4 Background subtraction procedure

The mass fits are used to normalize the background from the sideband data to that expected under the signal peak when performing the background subtraction. Signal and background shapes are determined independently in each bin and directly from data when performing the fit. To asses the impact of the specific choice of shapes used on the final result, we repeat the analysis by performing the background subtraction using a single normalization scale factor obtained from the time-integrated $D^0\pi_s$–mass distribution. The absolute variations in the resulting A_Γ values, 0.005% (0.023%) for $\pi^+\pi^-$ (K^+K^-), are used as systematic uncertainty associated with the mass shapes.

In the $\pi^+\pi^-$ and $K^-\pi^+$ channels we expect the background in $M(D^0\pi_s)$ to be dominated by combinations of real D^0 candidates and random soft pions, hence we expect the background shape to be the same in the two cases. We then repeat the mass fits after fixing the $\pi^+\pi^-$ background shape to that obtained when fitting the $K^-\pi^-$ distributions. The variation in the determination of $A_\Gamma(\pi^+\pi^-)$ (0.018%) is used as an additional systematic uncertainty associated with the mass shape.

The background subtraction procedure also assumes that the background impact parameter distribution in the sideband is the same as under the signal. To assign a systematic un-

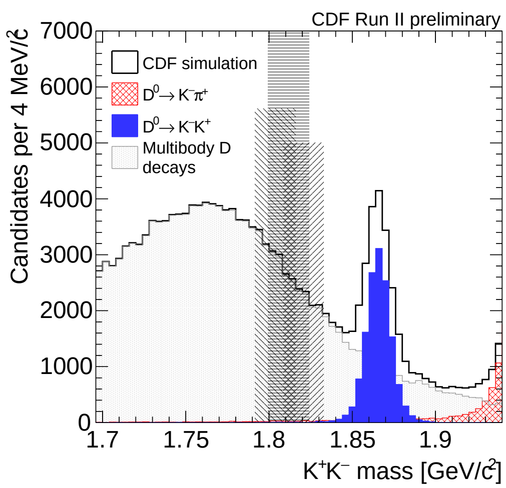

(a)

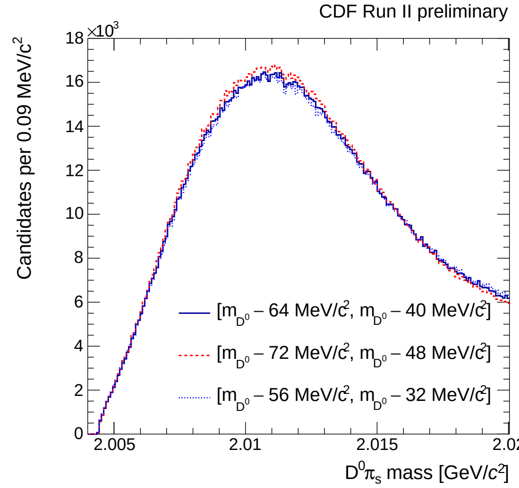

(b)

Figure 13: (a) Simulated events with definition of the three sideband regions used for the background subtraction in the K^+K^- channel and (b) corresponding $M(D^0\pi_s)$ distributions from data.

certainty to this assumption, we repeat the analysis with alternate definitions of the sideband regions. For the $\pi^+\pi^-$ case the $M(D^0\pi_s)$ sideband is changed from [2.015, 2.02] GeV/c^2 to [2.02, 2.025] GeV/c^2 and to [2.025, 2.030] GeV/c^2. For the K^+K^- case the $M(K^+K^-)$ sideband is changed from $[m_{D^0} - 64\,\text{MeV/c}^2, m_{D^0} - 40\,\text{MeV/c}^2]$ to $[m_{D^0} - 72\,\text{MeV/c}^2, m_{D^0} - 48\,\text{MeV/c}^2]$ and $[m_{D^0} - 56\,\text{MeV/c}^2, m_{D^0} - 32\,\text{MeV/c}^2]$ (see Fig. 13). The maximum absolute variations in the fitted values of A_Γ, 0.009% (0.030%) for $\pi^+\pi^-$ (K^+K^-), are used as systematic uncertainties associated with the choice of the sideband.

Contrary to the K^+K^- case, the mass fits for the $\pi^+\pi^-$ sample assume negligible background from mis-reconstructed charm decays peaking in $D^0\pi_s$ mass. Using simulation we estimate that a 0.93% contamination from physics backgrounds enters the $\pm 24\,\text{MeV}/c^2$ $\pi^+\pi^-$ signal range, dominated by the high-mass tail of the $D^0 \to K^-\pi^+$ decays [7]. As already explained, these decays are expected to have a null A_Γ value and then cannot bias the value of $A_\Gamma(\pi^+\pi^-)$. In addition, the results presented in the previous section show that the contribution to $A_\Gamma(\pi^+\pi^-)$ by this contamination would be totally negligible, as it would be equal to the product of the fraction of the contaminant and the value determined from the $K^-\pi^+$ fit: $0.93\% \times 0.05\% = 5 \times 10^{-6}$.

The total systematic uncertainty associated with the background subtraction procedure is obtained by summing the above components in quadrature. They result to be 0.010% for $A_\Gamma(\pi^+\pi^-)$ and 0.038% for $A_\Gamma(K^+K^-)$.

6.5 Impact parameter fit and secondary contamination

The impact parameter distribution of primary charm decays can be unambiguously determined from the first decay-time bin where the contamination from secondary charm produces negligible biases. From simulated events (see Fig. 14(a)) we also checked that assuming the prompt component to be independent of decay time is a good approximation up to 0.5% relative variation in the distribution width. Introducing such a small variation in our fit model produces completely negligible ($< 10^{-6}$) variations in the resulting A_Γ value.

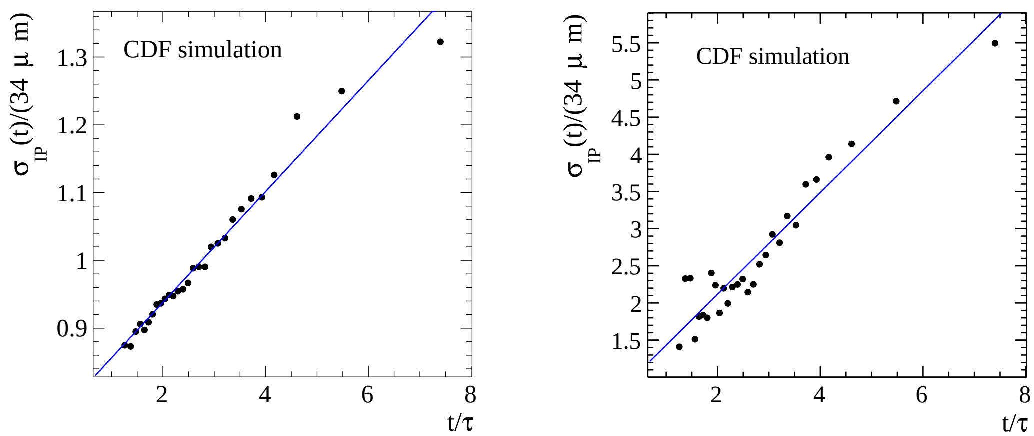

(a) (b)

Figure 14: Relative decay-time variation of the impact parameter distribution's width for a simulated sample of (a) D^*-tagged $D^0 \to \pi^+\pi^-$ and (b) inclusive $B \to DX$ decays.

On the other hand, the knowledge of the actual impact parameter distribution of secondary charm (and in particular how much it peaks below the prompt peak) is much more uncertain as this distribution also evolves with decay time. To check the stability of the result against the assumed secondary shape we repeat the fit changing the double Gaussian model to

1. an exponential function symmetric around zero, this model being inspired by the study of an inclusive sample of $B \to D^{*-}\mu^+ X$ decays, built by combining of our D^* candidates with good quality muons found in the event; and to

2. a single Gaussian, whose width is bound to follow the same decay-time dependence observed in the simulated sample of inclusive $B \to DX$ decays, $\sigma = \sigma_p \times [0.75 + 0.68 \times (t/\tau)]$ where $\sigma_p \approx 34\,\mu$m is the width of the prompt peak (see Fig. 14(b)).

In addition, we also estimate the decay-time variation of the secondary contamination with a fit to the decay-time distribution obtained from the yields of Tab. 2, using histogram templates from simulation to describe the prompt and secondary shapes shapes, as was done for the time-integrated asymmetry analyses [7].

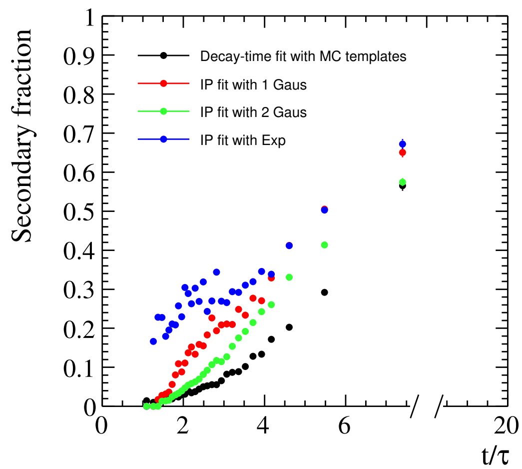

Figure 15: Comparison of the contamination fraction from secondary decays versus decay time from the different methods used.

Figure 15 shows the comparison between the resulting fractions, as a function of decay time, from the different methods for the $\pi^+\pi^-$ case. While the exponential model seems to overestimate the secondary fraction, the prediction based on the available samples of simulated events may have underestimated it. We then decided to asses the systematic uncertainty associated with the secondary impact-parameter shape as the absolute variation in the fitted value of A_Γ when changing the secondary model from a sum of two Gaussian functions to the single Gaussian case. The systematic uncertainties on $A_\Gamma(\pi^+\pi^-)$ and $A_\Gamma(K^+K^-)$ are found to be 0.026% and 0.010%, respectively.

The A_Γ fit has been, anyhow, repeated for all the secondary models, and in all cases similar marginal variations of the final results are observed. This is expected as the secondary contamination is predicted (and measure by our fits) to be charge symmetric, thus cannot significantly bias the measured asymmetries.

6.6 Decay-time scale

The normalized decay time is calculated as $L_{xy}m_{D^0}/(p_T\tau)$, where the known D^0 mass and lifetime are used. The uncertainties on these values [8] do not affect significantly the determination of t/τ. A systematic uncertainty may instead arise from imperfect alignment of the silicon detector as this would translate in a wrong decay-length scale. Previous studies of the limited knowledge of the silicon detector alignment [11] estimated an uncertainty of $\pm 2\,\mu$m on L_{xy}, which translate in a 1.6% relative uncertainty on the estimated D^0 decay time.

This uncertainty is propagated to the A_Γ determination and results in a 0.001% (0.003%) systematic uncertainty on $A_\Gamma(\pi^+\pi^-)$ ($A_\Gamma(K^+K^-)$).

6.7 Total systematic uncertainty

Table 3 summarizes the most significant systematic uncertainties considered in the measurement. Assuming them independent and summing in quadrature, we obtain a total systematic uncertainty on $A_\Gamma(K^+K^-)$ and $A_\Gamma(\pi^+\pi^-)$ of 0.066% and 0.063%, respectively.

Source	$\Delta A_\Gamma(\pi^+\pi^-)$	$\Delta A_\Gamma(K^+K^-)$
Background subtraction	0.021%	0.038%
Impact parameter shapes	0.026%	0.010%
Decay-time scale	0.001%	0.003%
Total	0.033%	0.039%

Table 3: Summary of most significant systematic uncertainties. The total uncertainty is the sum in quadrature of all the contributions.

7 Final results

Using the full Run II data set, we measure the effective-lifetime asymmetry between D^0 and $\overline{D}^0$ decays to two-body CP-even final states to be

$$A_\Gamma(K^+K^-) = (-1.9 \pm 1.5 \pm 0.4) \times 10^{-3},$$
$$A_\Gamma(\pi^+\pi^-) = (-0.1 \pm 1.8 \pm 0.3) \times 10^{-3},$$

where the first uncertainty is statistical and the second systematic. Both results are compatible with CP conservation and with other experimental measurements [1]. As the systematic uncertainties are largely uncorrelated, the two results can be averaged to obtain a more precise determination of the effective-lifetime asymmetry: $A_\Gamma = (-1.2 \pm 1.2) \times 10^{-3}$.

References

[1] D. Asner *et al.*, arXiv:1010.1589 and online updates at `http://www.slac.stanford.edu/xorg/hfag`.

[2] S. Bianco, F. L. Fabbri, D. Benson, and I. I. Bigi, Riv. Nuovo Cim. **26N7**, 1 (2003) [arXiv:hep-ex/0309021]; Y. Grossman, A. L. Kagan and Y. Nir, *Phys. Rev.* **D 75** (2007) 036008, I. I. Bigi, A. Paul, and S. Recksiegel, *J. High Energy Phys.* **06** (2011) 089; I. I. Bigi and A. Paul, [arXiv:1110.2862]; H. -Y. Cheng and C.-W. Chiang, arXiv:1201.0785.

[3] M. Gersabeck *et al.* arXiv:1111.6515v2.

[4] Marko Staric *et al.* [Belle Collaboration], arXiv:1212.3478.

[5] J. P. Lees *et al.* [BaBar Collaboration], arXiv:1209.3896.

[6] R. Aaij *et al.* [LHCb Collaboration], arXiv:1310.7201.

[7] T. Aaltonen *et al.* [CDF Collaboration], arXiv:1207.2158; A. Di Canto *et al.*, CDF Note 10746.

[8] J. Beringer *et al.* [Particle Data Group], Phys. Rev. D 86, 010001 (2012).

[9] N. L. Johnson, Biometrika 36, 149 (1949).

[10] T. Aaltonen *et al.* [CDF Collaboration], arXiv:1309.4078; S. Behari *et al.*, CDF Note 10914.

[11] S. Menzemer, Ph.D. Thesis, Karlsruhe University, FERMILAB-THESIS-2003-52(2003)

A Detailed mass fit projections

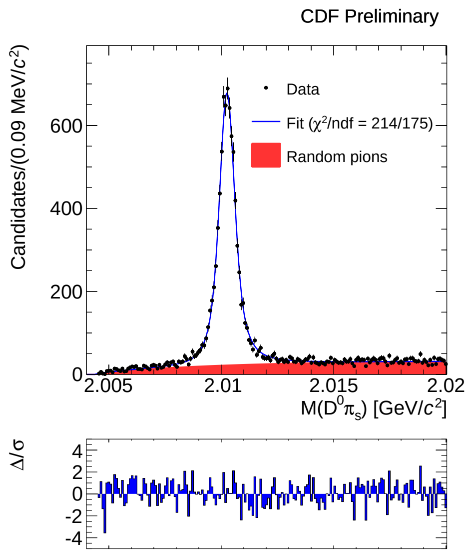

(a)

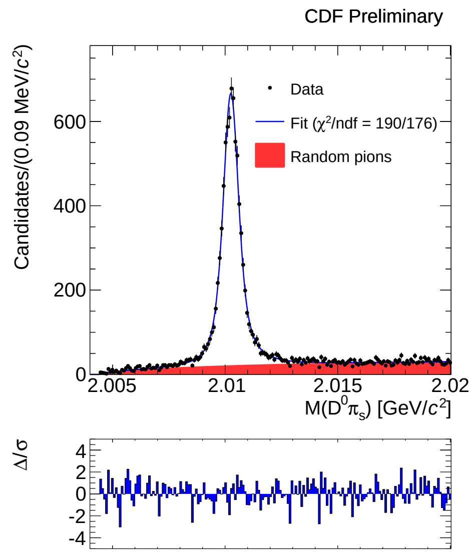

(b)

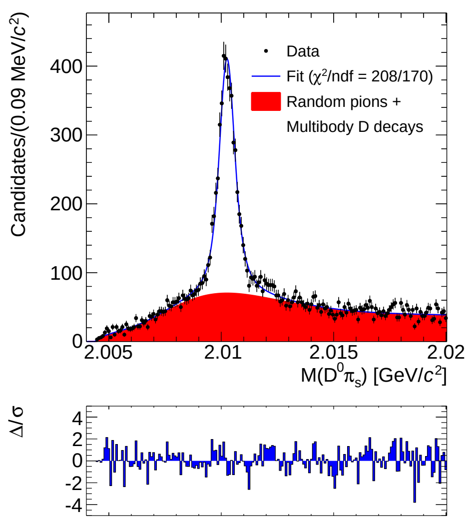

(c)

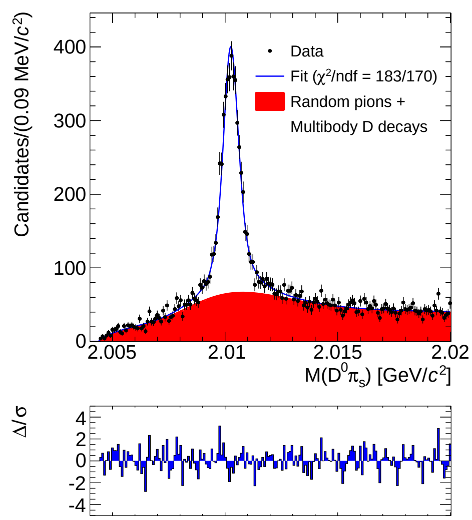

(d)

Figure 16: $D^0\pi_s$–mass distributions of (a) $D^{*-} \to \overline{D}^0(\to \pi^+\pi^-)\pi_s^-$, (b) $D^{*+} \to D^0(\to \pi^+\pi^-)\pi_s^+$, (c) $D^{*-} \to \overline{D}^0(\to K^+K^-)\pi_s^-$ and (d) $D^{*+} \to D^0(\to K^+K^-)\pi_s^+$ candidates restricted in the decay-time bin 0 ($t < 1.18\tau$), with fit projections overlaid.

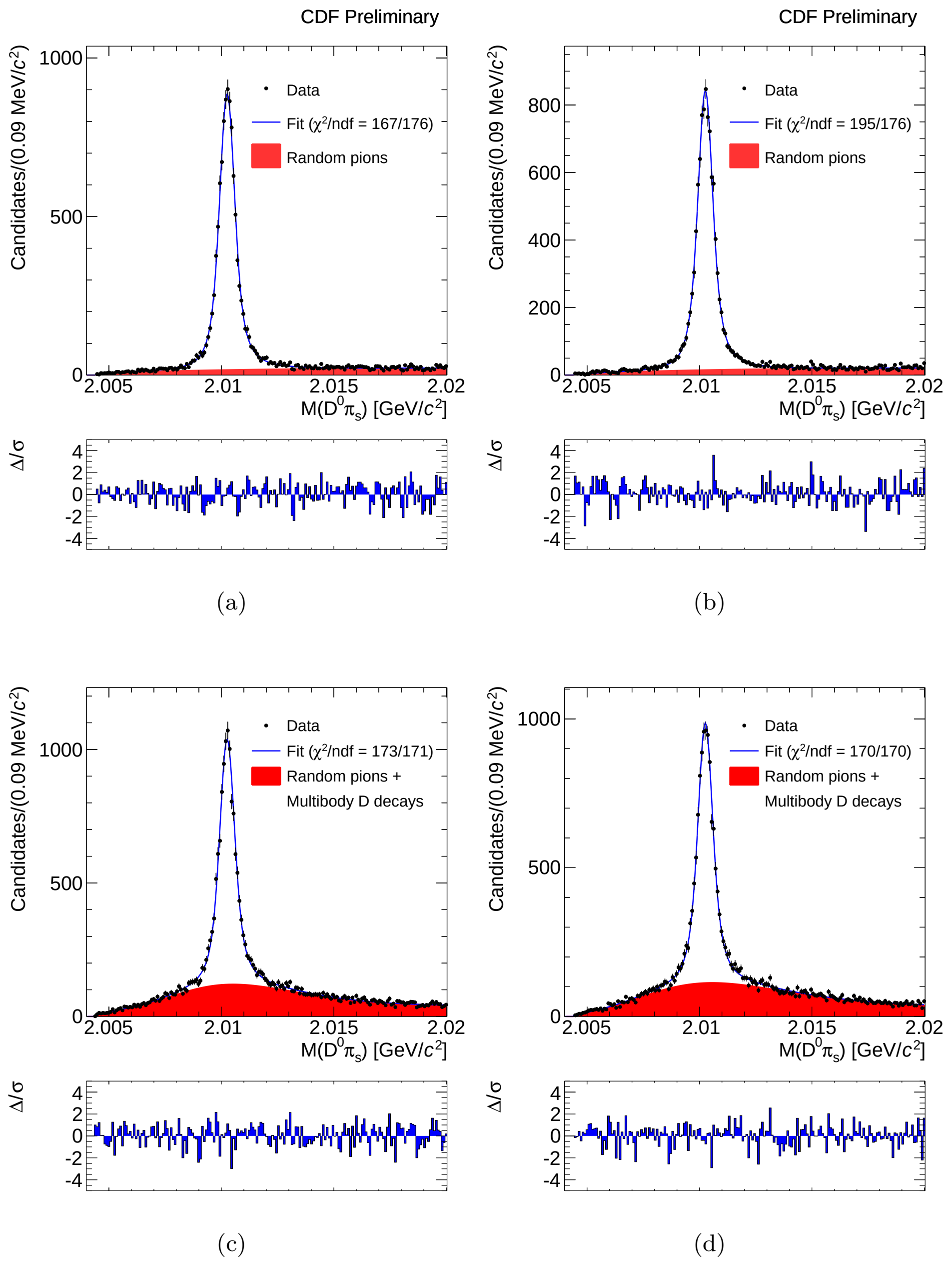

Figure 17: $D^0\pi_s$–mass distributions of (a) $D^{*-} \to \overline{D}^0(\to \pi^+\pi^-)\pi_s^-$, (b) $D^{*+} \to D^0(\to \pi^+\pi^-)\pi_s^+$, (c) $D^{*-} \to \overline{D}^0(\to K^+K^-)\pi_s^-$ and (d) $D^{*+} \to D^0(\to K^+K^-)\pi_s^+$ candidates restricted in the decay-time bin 1 ($1.18\tau < t < 1.32\tau$), with fit projections overlaid.

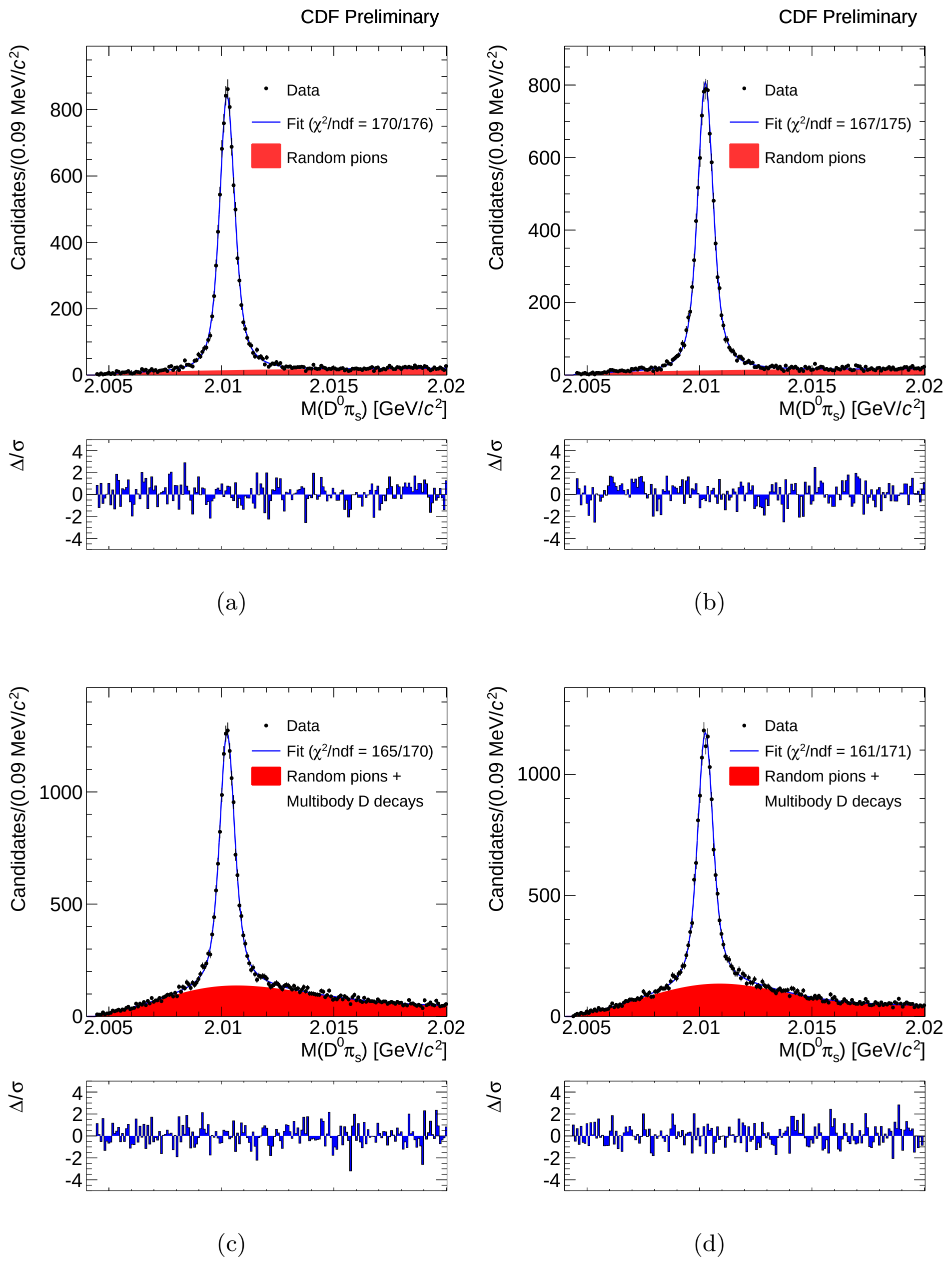

Figure 18: $D^0\pi_s$–mass distributions of (a) $D^{*-} \to \overline{D}^0(\to \pi^+\pi^-)\pi_s^-$, (b) $D^{*+} \to D^0(\to \pi^+\pi^-)\pi_s^+$, (c) $D^{*-} \to \overline{D}^0(\to K^+K^-)\pi_s^-$ and (d) $D^{*+} \to D^0(\to K^+K^-)\pi_s^+$ candidates restricted in the decay-time bin 2 ($1.32\tau < t < 1.42\tau$), with fit projections overlaid.

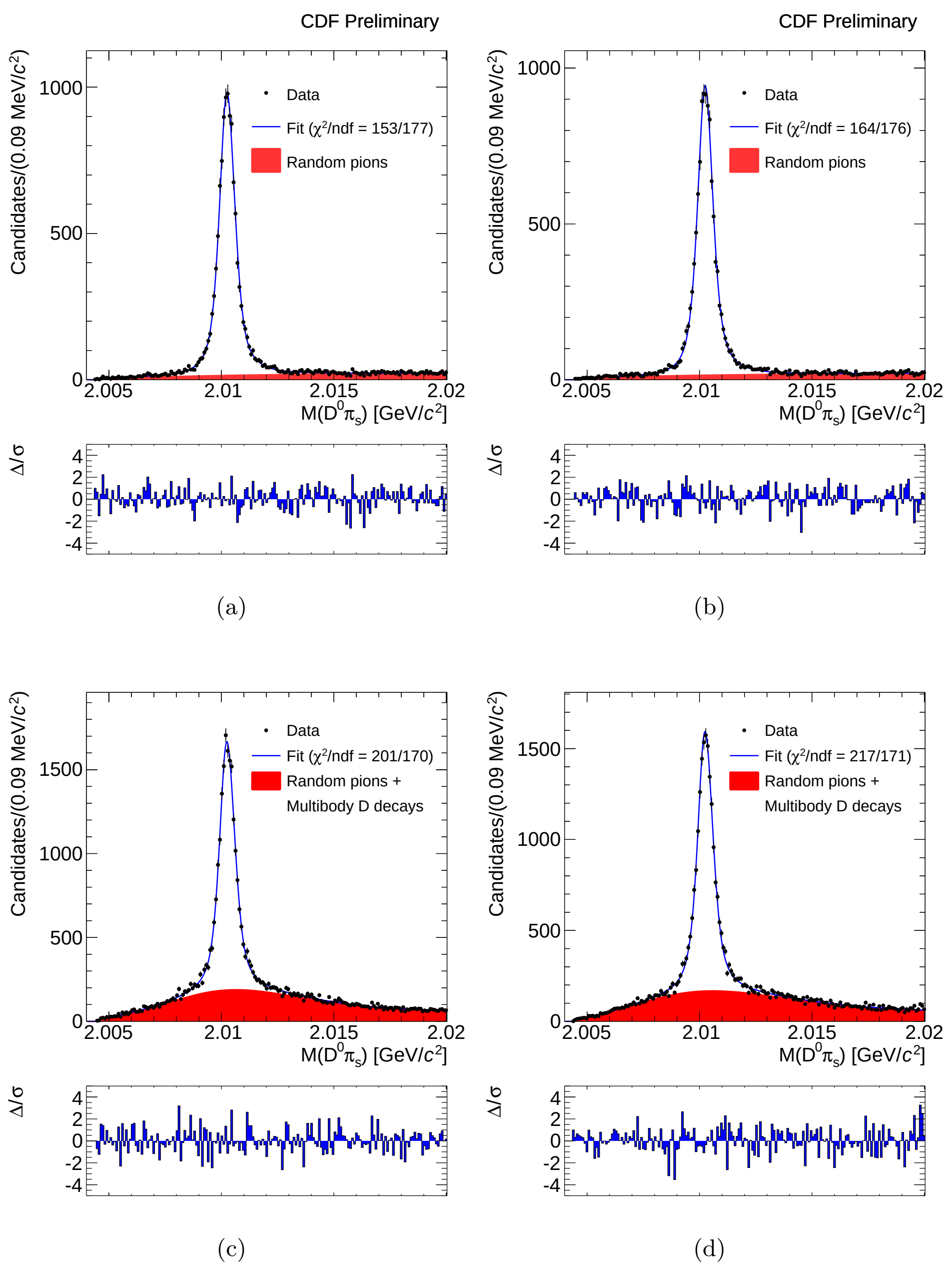

Figure 19: $D^0\pi_s$–mass distributions of (a) $D^{*-} \to \overline{D}^0(\to \pi^+\pi^-)\pi_s^-$, (b) $D^{*+} \to D^0(\to \pi^+\pi^-)\pi_s^+$, (c) $D^{*-} \to \overline{D}^0(\to K^+K^-)\pi_s^-$ and (d) $D^{*+} \to D^0(\to K^+K^-)\pi_s^+$ candidates restricted in the decay-time bin 3 ($1.42\tau < t < 1.52\tau$), with fit projections overlaid.

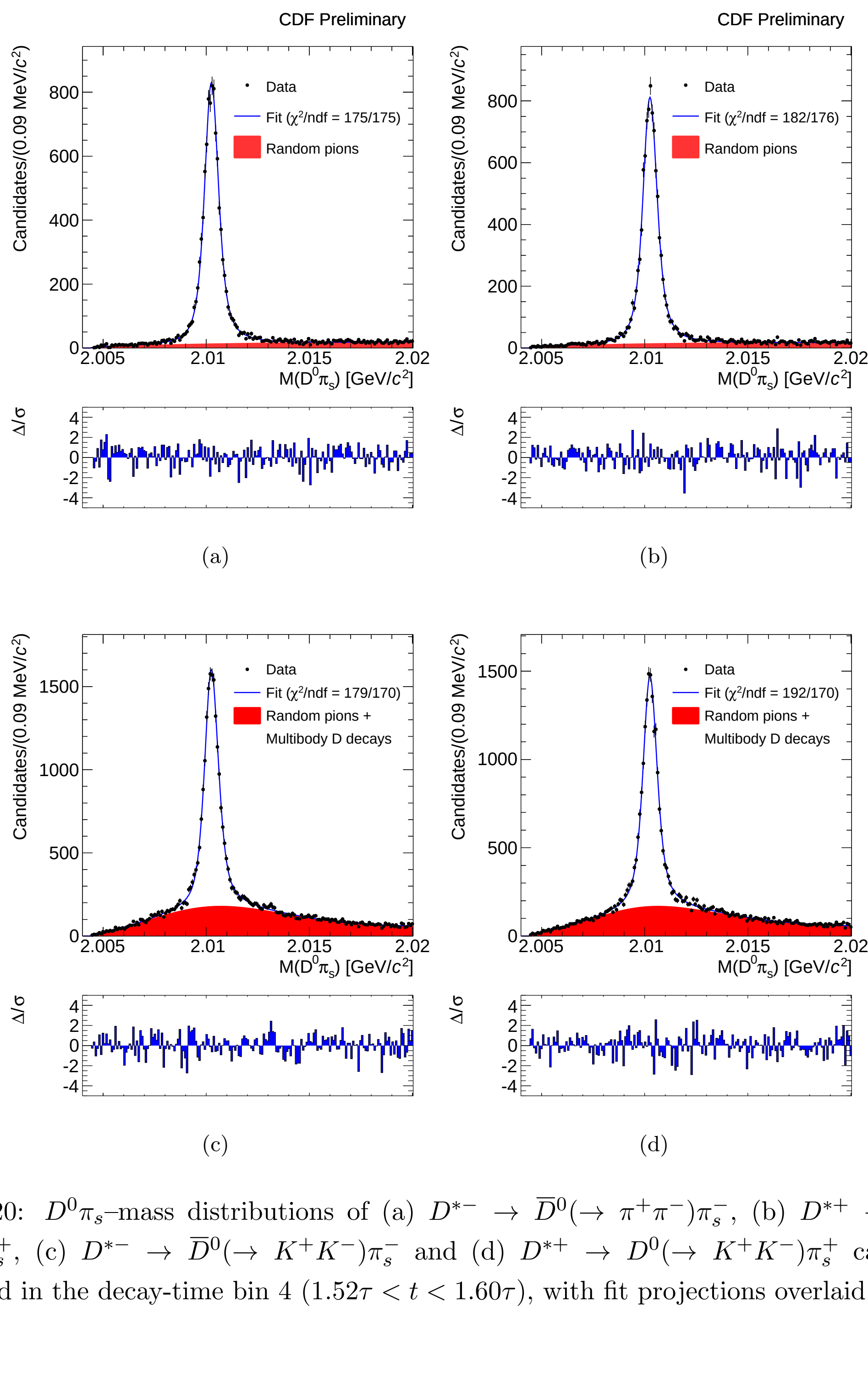

(a) (b)

(c) (d)

Figure 20: $D^0\pi_s$–mass distributions of (a) $D^{*-} \to \overline{D}^0(\to \pi^+\pi^-)\pi_s^-$, (b) $D^{*+} \to D^0(\to \pi^+\pi^-)\pi_s^+$, (c) $D^{*-} \to \overline{D}^0(\to K^+K^-)\pi_s^-$ and (d) $D^{*+} \to D^0(\to K^+K^-)\pi_s^+$ candidates restricted in the decay-time bin 4 ($1.52\tau < t < 1.60\tau$), with fit projections overlaid.

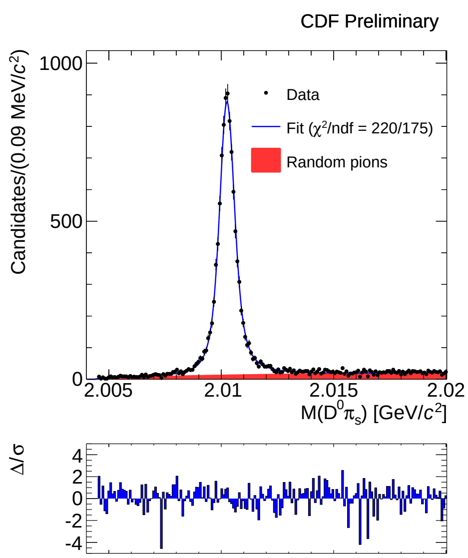

(a)

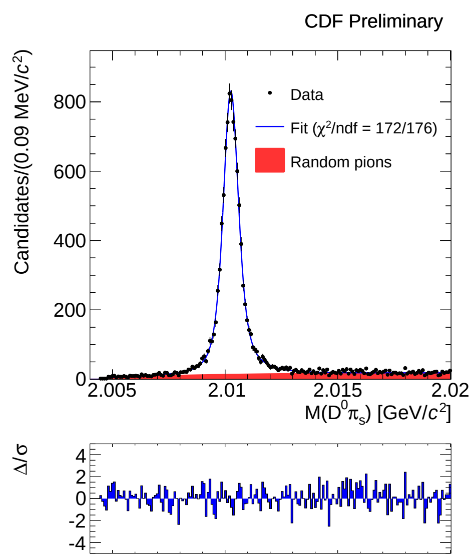

(b)

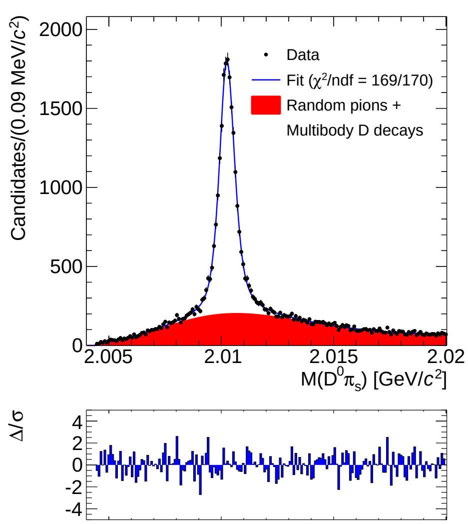

(c)

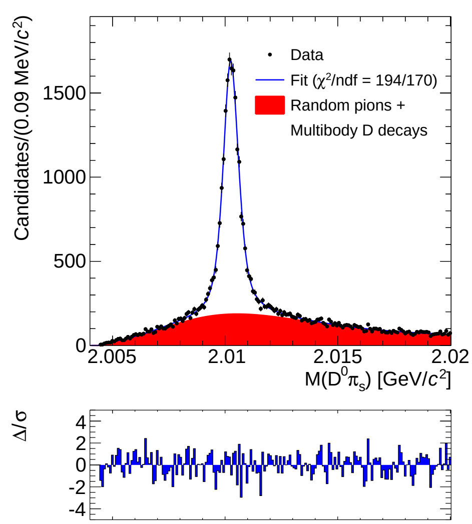

(d)

Figure 21: $D^0\pi_s$–mass distributions of (a) $D^{*-} \to \overline{D}^0(\to \pi^+\pi^-)\pi_s^-$, (b) $D^{*+} \to D^0(\to \pi^+\pi^-)\pi_s^+$, (c) $D^{*-} \to \overline{D}^0(\to K^+K^-)\pi_s^-$ and (d) $D^{*+} \to D^0(\to K^+K^-)\pi_s^+$ candidates restricted in the decay-time bin 5 ($1.60\tau < t < 1.68\tau$), with fit projections overlaid.

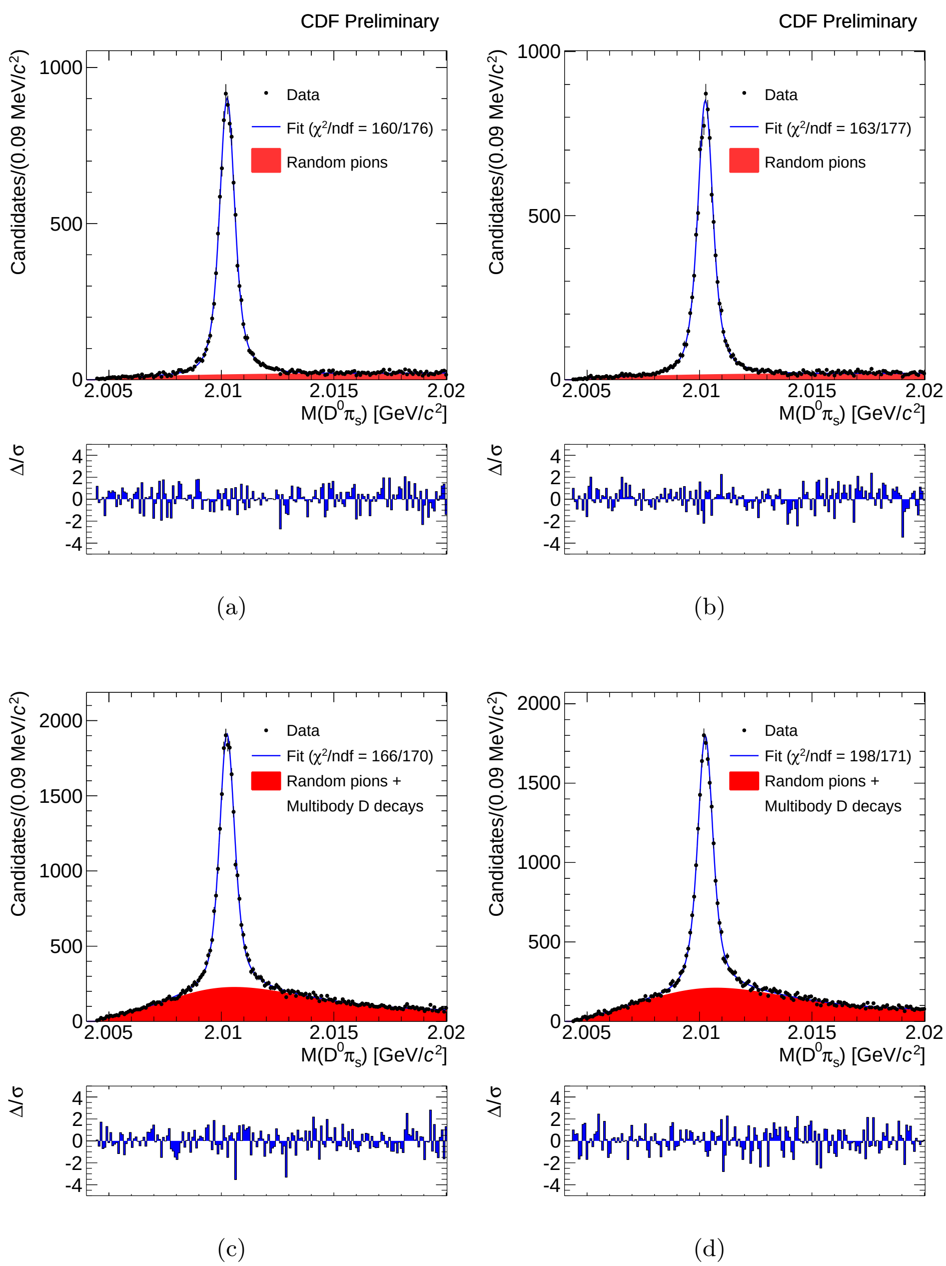

Figure 22: $D^0\pi_s$–mass distributions of (a) $D^{*-} \to \overline{D}^0(\to \pi^+\pi^-)\pi_s^-$, (b) $D^{*+} \to D^0(\to \pi^+\pi^-)\pi_s^+$, (c) $D^{*-} \to \overline{D}^0(\to K^+K^-)\pi_s^-$ and (d) $D^{*+} \to D^0(\to K^+K^-)\pi_s^+$ candidates restricted in the decay-time bin 6 ($1.68\tau < t < 1.76\tau$), with fit projections overlaid.

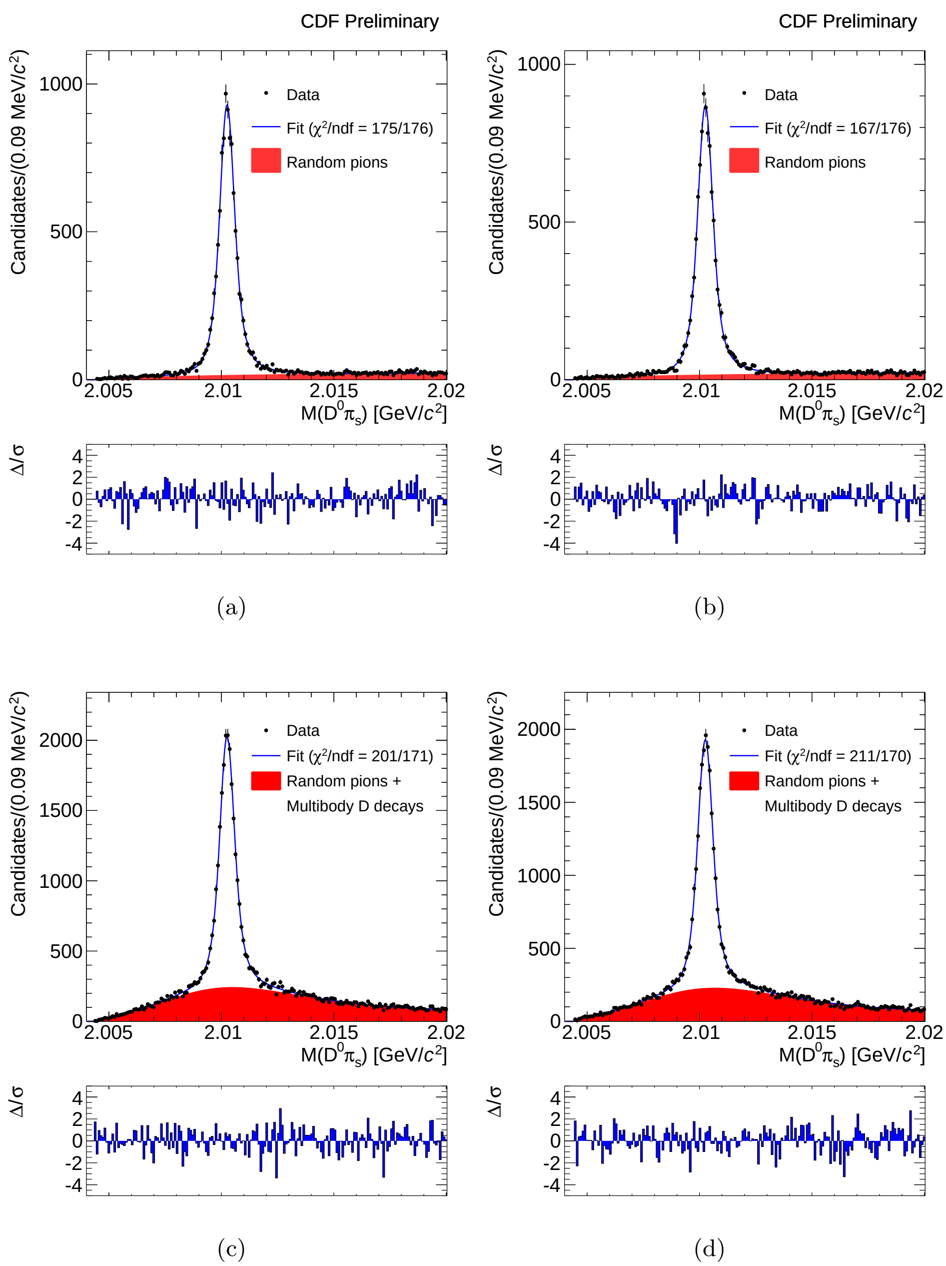

Figure 23: $D^0\pi_s$–mass distributions of (a) $D^{*-} \to \overline{D}^0(\to \pi^+\pi^-)\pi_s^-$, (b) $D^{*+} \to D^0(\to \pi^+\pi^-)\pi_s^+$, (c) $D^{*-} \to \overline{D}^0(\to K^+K^-)\pi_s^-$ and (d) $D^{*+} \to D^0(\to K^+K^-)\pi_s^+$ candidates restricted in the decay-time bin 7 ($1.76\tau < t < 1.84\tau$), with fit projections overlaid.

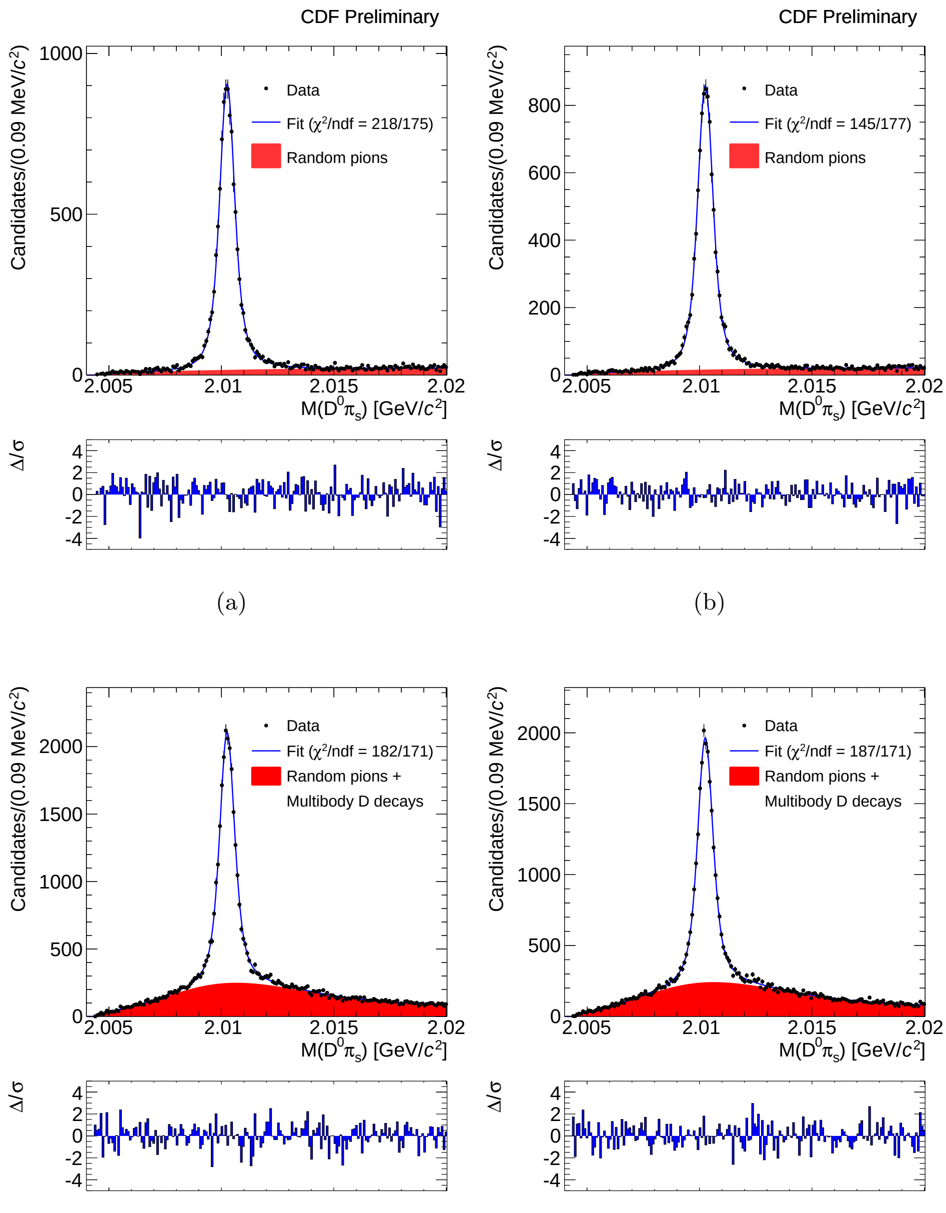

(a) (b)

(c) (d)

Figure 24: $D^0\pi_s$–mass distributions of (a) $D^{*-} \to \overline{D}^0(\to \pi^+\pi^-)\pi_s^-$, (b) $D^{*+} \to D^0(\to \pi^+\pi^-)\pi_s^+$, (c) $D^{*-} \to \overline{D}^0(\to K^+K^-)\pi_s^-$ and (d) $D^{*+} \to D^0(\to K^+K^-)\pi_s^+$ candidates restricted in the decay-time bin 8 ($1.84\tau < t < 1.92\tau$), with fit projections overlaid.

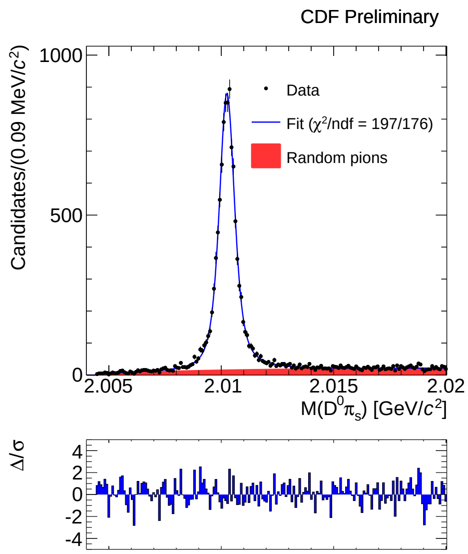

(a)

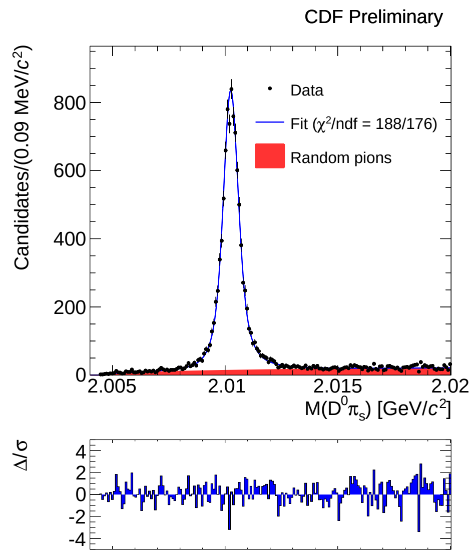

(b)

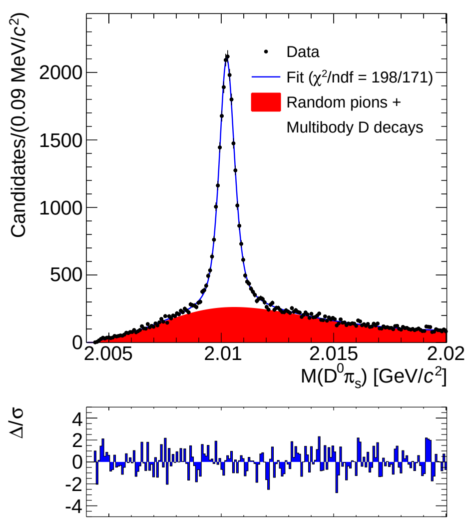

(c)

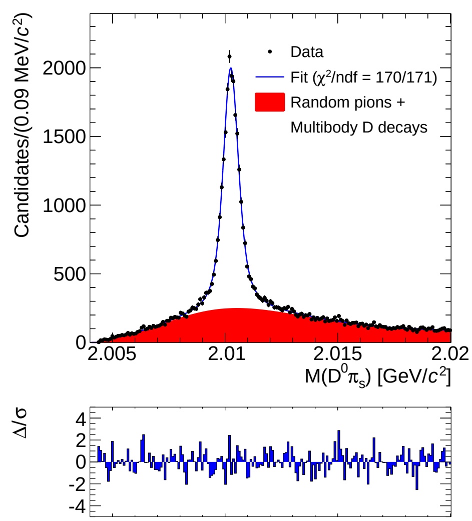

(d)

Figure 25: $D^0\pi_s$–mass distributions of (a) $D^{*-} \to \overline{D}^0(\to \pi^+\pi^-)\pi_s^-$, (b) $D^{*+} \to D^0(\to \pi^+\pi^-)\pi_s^+$, (c) $D^{*-} \to \overline{D}^0(\to K^+K^-)\pi_s^-$ and (d) $D^{*+} \to D^0(\to K^+K^-)\pi_s^+$ candidates restricted in the decay-time bin 9 ($1.92\tau < t < 2.00\tau$), with fit projections overlaid.

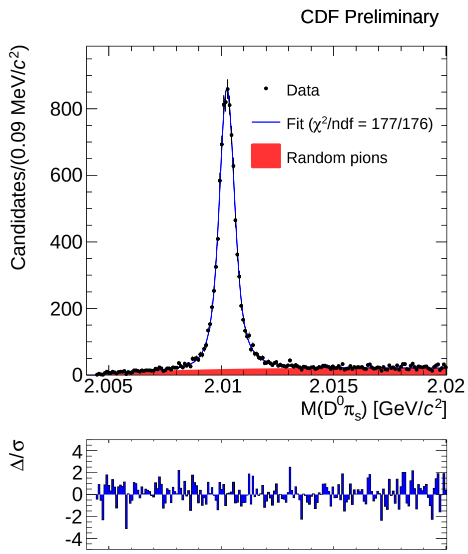

(a)

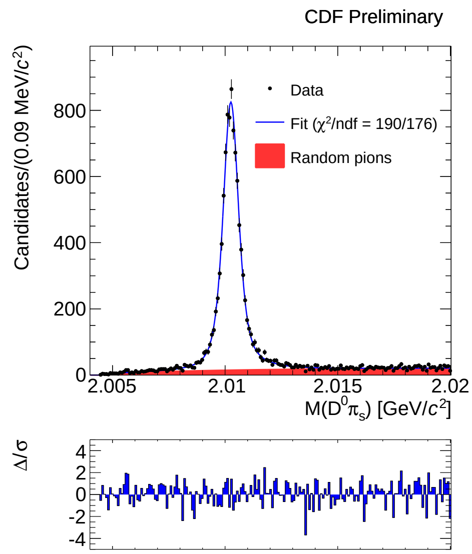

(b)

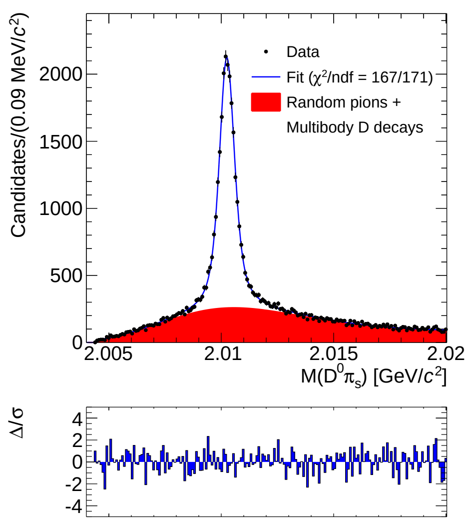

(c)

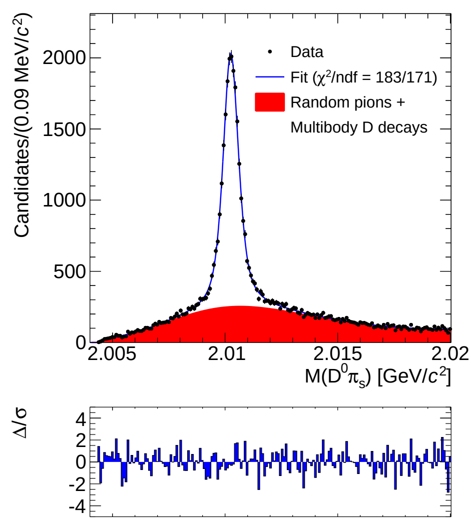

(d)

Figure 26: $D^0\pi_s$–mass distributions of (a) $D^{*-} \to \overline{D}^0(\to \pi^+\pi^-)\pi_s^-$, (b) $D^{*+} \to D^0(\to \pi^+\pi^-)\pi_s^+$, (c) $D^{*-} \to \overline{D}^0(\to K^+K^-)\pi_s^-$ and (d) $D^{*+} \to D^0(\to K^+K^-)\pi_s^+$ candidates restricted in the decay-time bin 10 ($2.00\tau < t < 2.08\tau$), with fit projections overlaid.

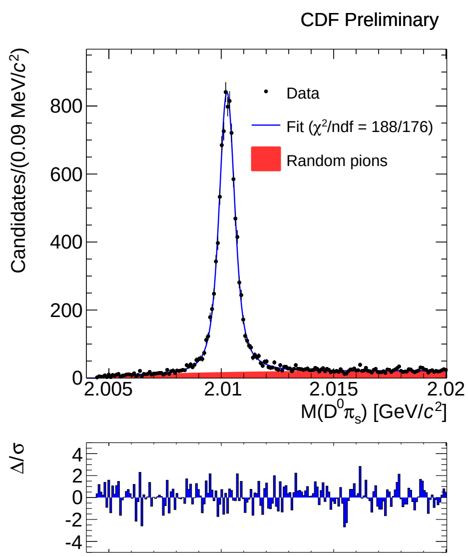

(a)

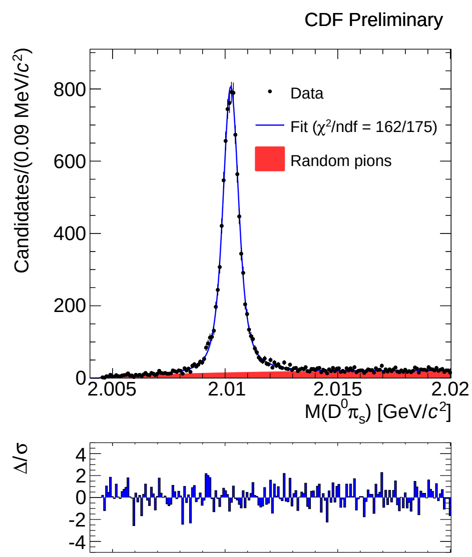

(b)

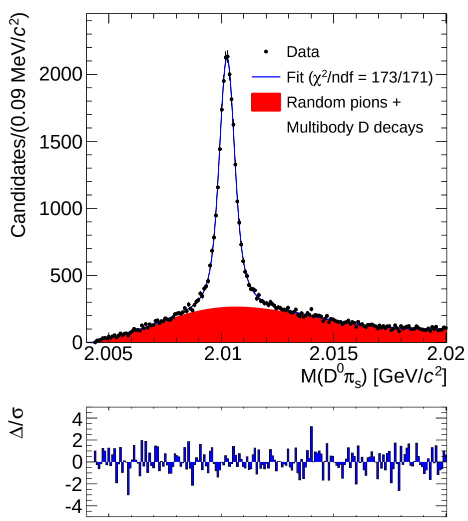

(c)

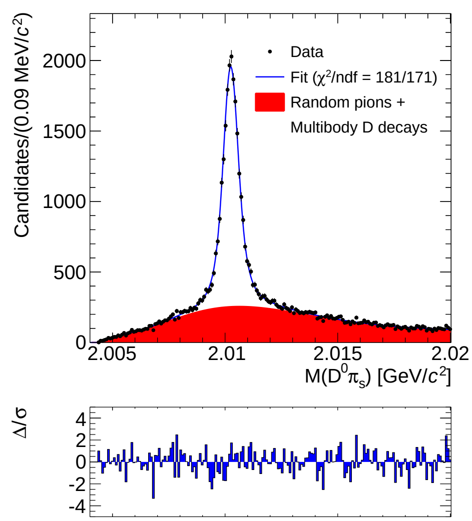

(d)

Figure 27: $D^0\pi_s$–mass distributions of (a) $D^{*-} \to \overline{D}^0(\to \pi^+\pi^-)\pi_s^-$, (b) $D^{*+} \to D^0(\to \pi^+\pi^-)\pi_s^+$, (c) $D^{*-} \to \overline{D}^0(\to K^+K^-)\pi_s^-$ and (d) $D^{*+} \to D^0(\to K^+K^-)\pi_s^+$ candidates restricted in the decay-time bin 11 ($2.08\tau < t < 2.16\tau$), with fit projections overlaid.

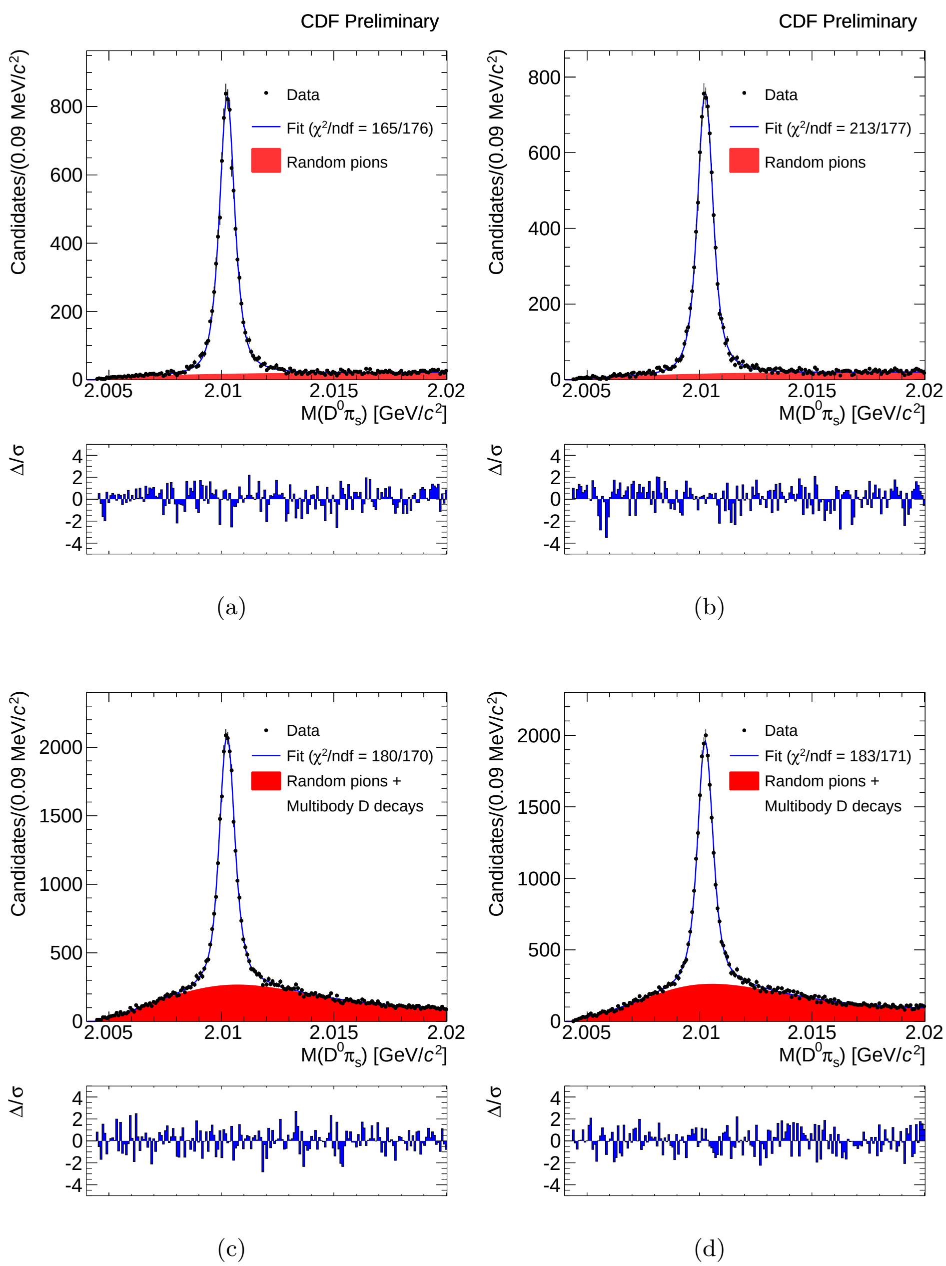

Figure 28: $D^0\pi_s$–mass distributions of (a) $D^{*-} \to \overline{D}^0(\to \pi^+\pi^-)\pi_s^-$, (b) $D^{*+} \to D^0(\to \pi^+\pi^-)\pi_s^+$, (c) $D^{*-} \to \overline{D}^0(\to K^+K^-)\pi_s^-$ and (d) $D^{*+} \to D^0(\to K^+K^-)\pi_s^+$ candidates restricted in the decay-time bin 12 ($2.16\tau < t < 2.24\tau$), with fit projections overlaid.

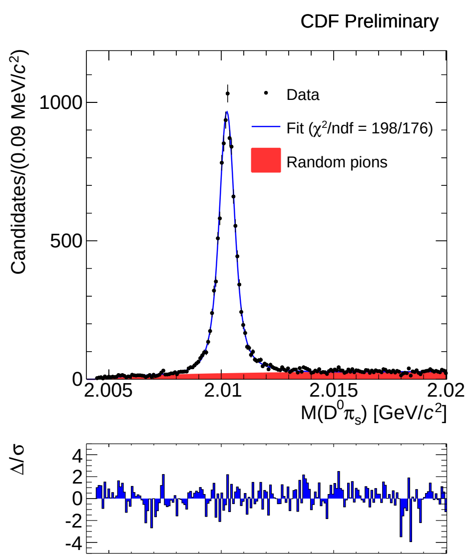

(a)

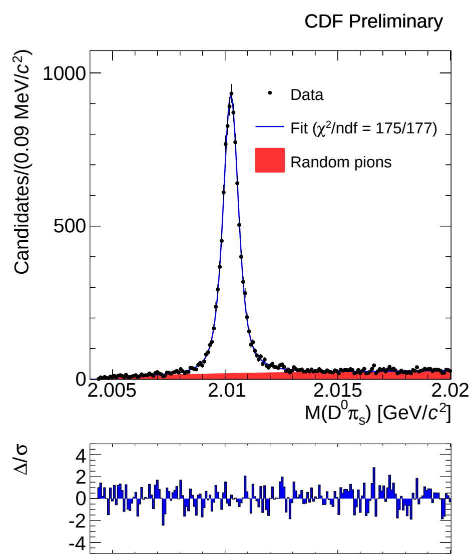

(b)

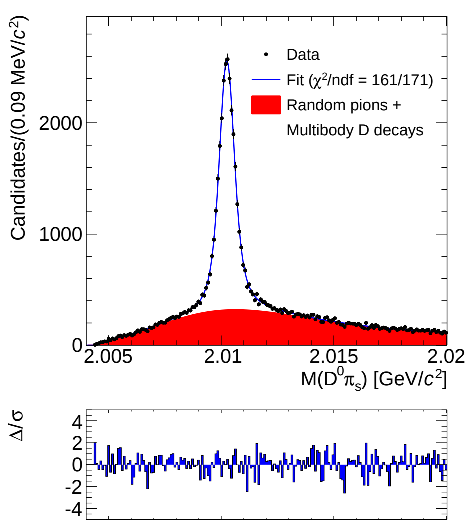

(c)

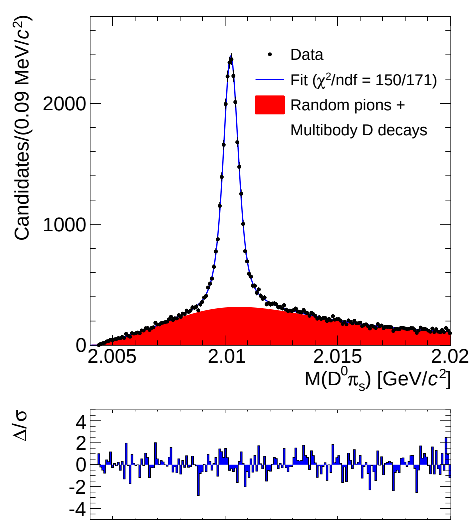

(d)

Figure 29: $D^0\pi_s$–mass distributions of (a) $D^{*-} \to \overline{D}^0(\to \pi^+\pi^-)\pi_s^-$, (b) $D^{*+} \to D^0(\to \pi^+\pi^-)\pi_s^+$, (c) $D^{*-} \to \overline{D}^0(\to K^+K^-)\pi_s^-$ and (d) $D^{*+} \to D^0(\to K^+K^-)\pi_s^+$ candidates restricted in the decay-time bin 13 ($2.24\tau < t < 2.34\tau$), with fit projections overlaid.

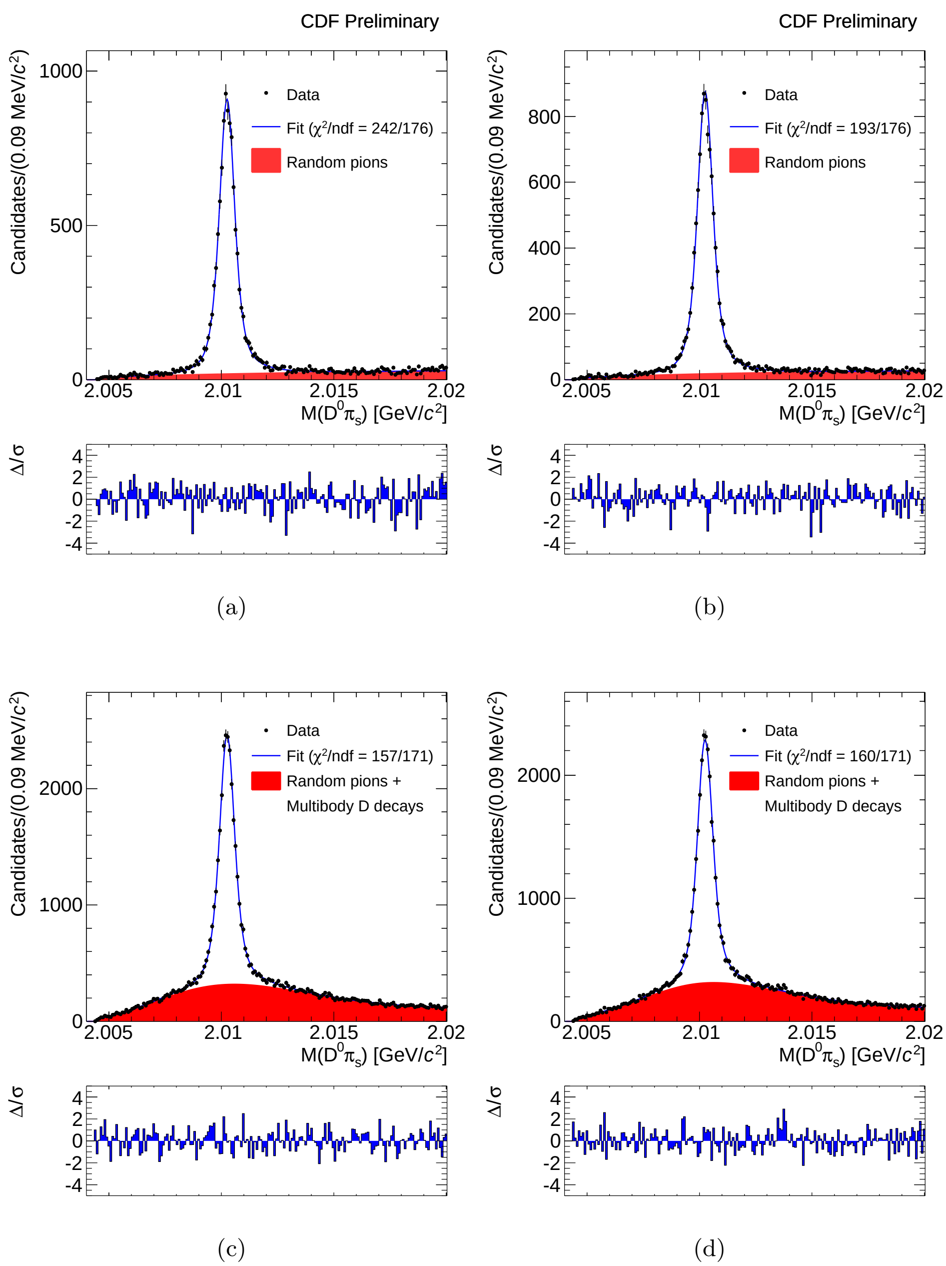

Figure 30: $D^0\pi_s$–mass distributions of (a) $D^{*-} \to \overline{D}^0(\to \pi^+\pi^-)\pi_s^-$, (b) $D^{*+} \to D^0(\to \pi^+\pi^-)\pi_s^+$, (c) $D^{*-} \to \overline{D}^0(\to K^+K^-)\pi_s^-$ and (d) $D^{*+} \to D^0(\to K^+K^-)\pi_s^+$ candidates restricted in the decay-time bin 14 ($2.34\tau < t < 2.44\tau$), with fit projections overlaid.

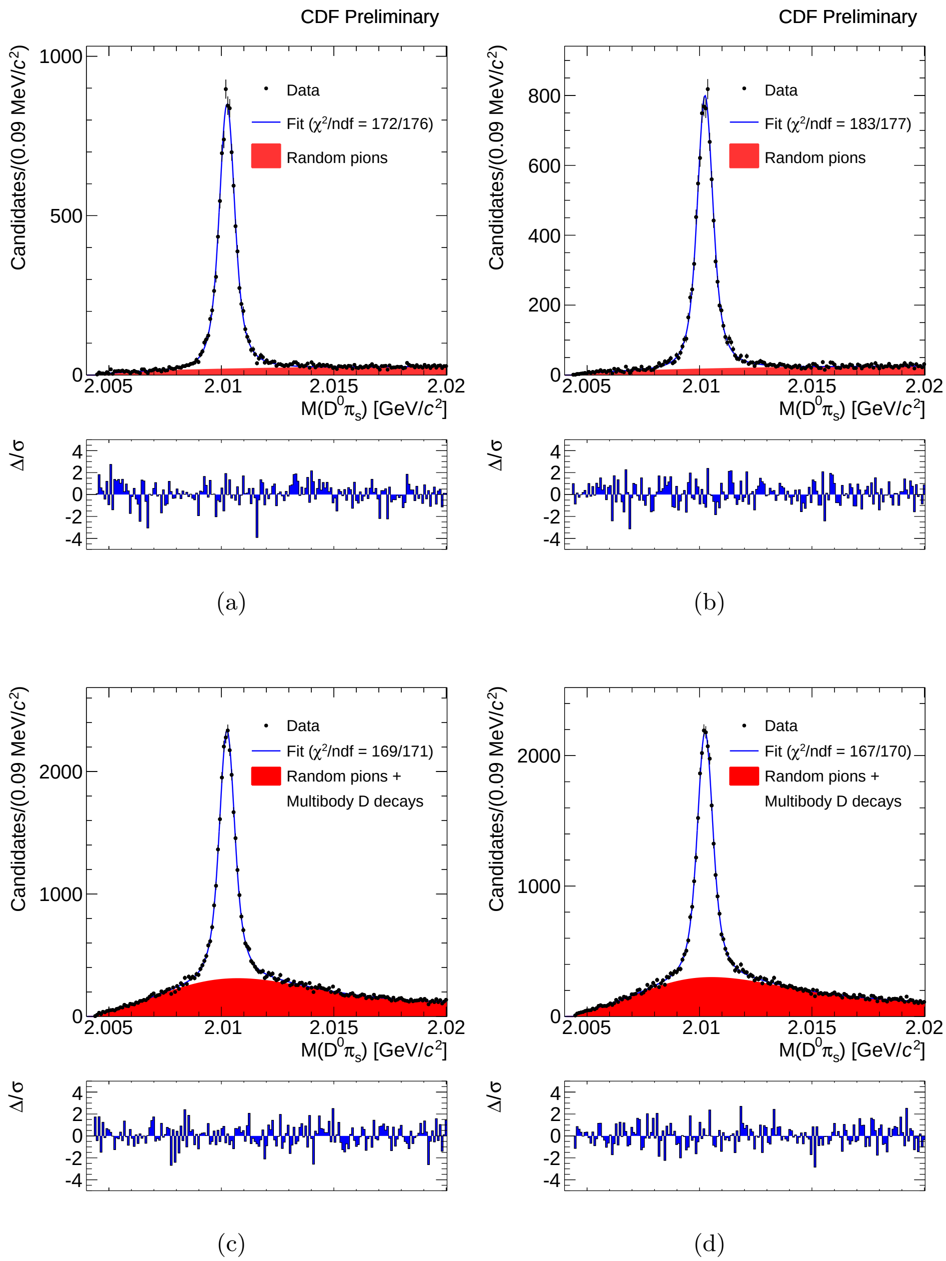

Figure 31: $D^0\pi_s$–mass distributions of (a) $D^{*-} \to \overline{D}^0(\to \pi^+\pi^-)\pi_s^-$, (b) $D^{*+} \to D^0(\to \pi^+\pi^-)\pi_s^+$, (c) $D^{*-} \to \overline{D}^0(\to K^+K^-)\pi_s^-$ and (d) $D^{*+} \to D^0(\to K^+K^-)\pi_s^+$ candidates restricted in the decay-time bin 15 ($2.44\tau < t < 2.54\tau$), with fit projections overlaid.

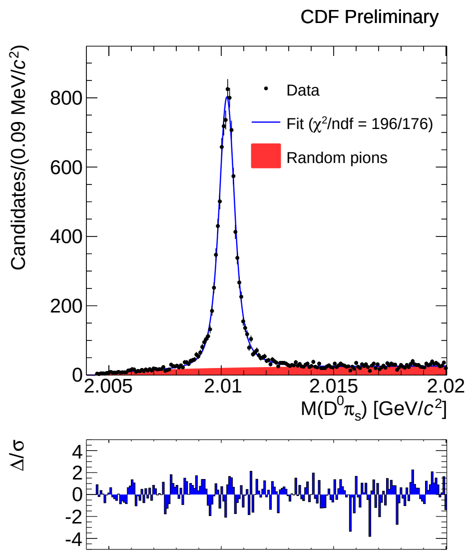

(a)

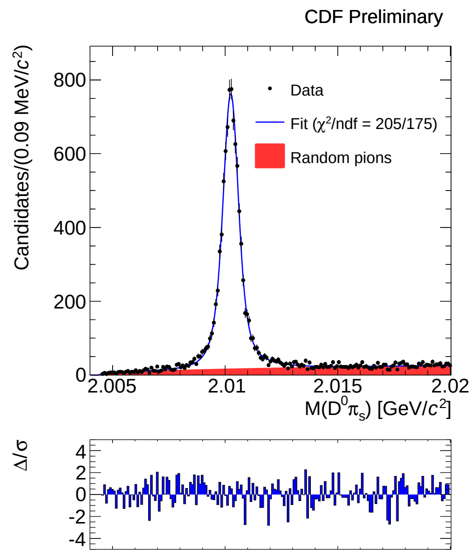

(b)

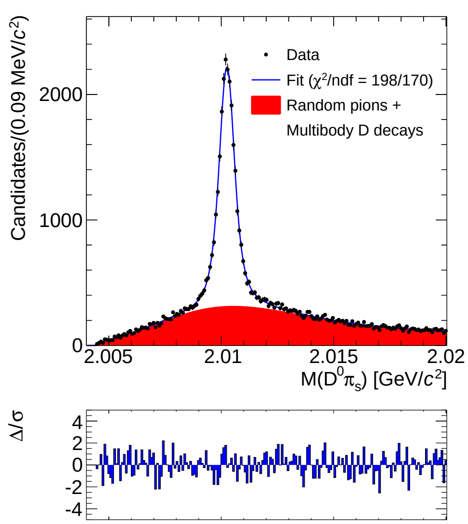

(c)

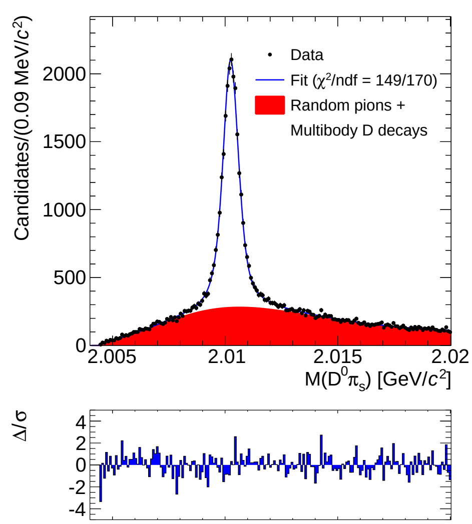

(d)

Figure 32: $D^0\pi_s$–mass distributions of (a) $D^{*-} \to \overline{D}^0(\to \pi^+\pi^-)\pi_s^-$, (b) $D^{*+} \to D^0(\to \pi^+\pi^-)\pi_s^+$, (c) $D^{*-} \to \overline{D}^0(\to K^+K^-)\pi_s^-$ and (d) $D^{*+} \to D^0(\to K^+K^-)\pi_s^+$ candidates restricted in the decay-time bin 16 ($2.54\tau < t < 2.64\tau$), with fit projections overlaid.

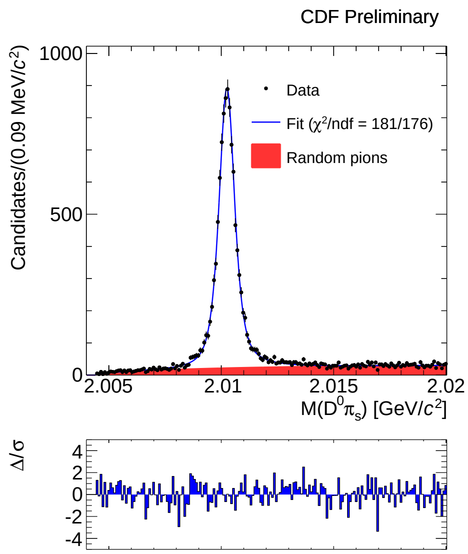

(a)

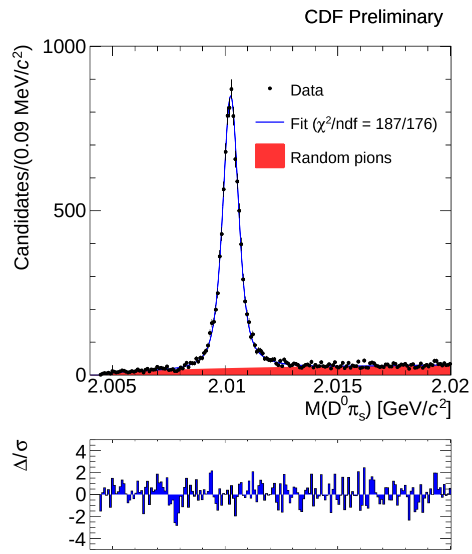

(b)

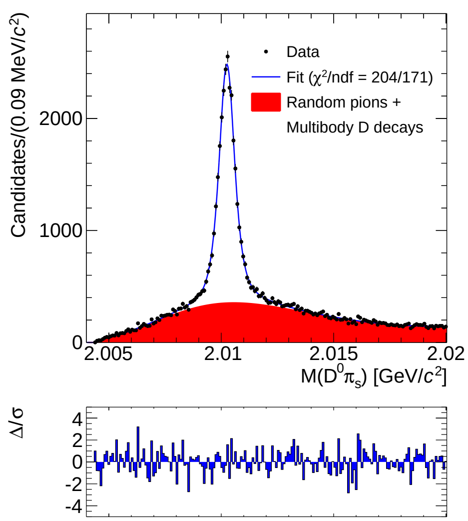

(c)

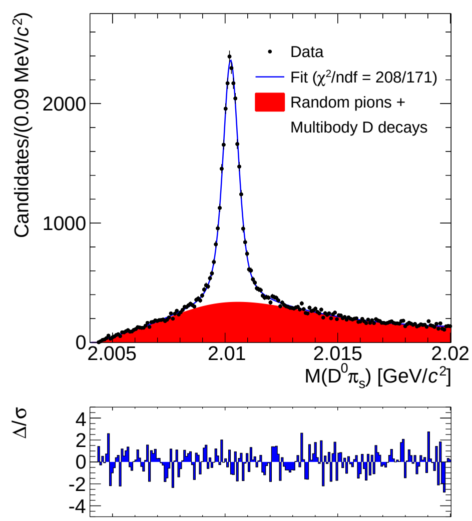

(d)

Figure 33: $D^0\pi_s$–mass distributions of (a) $D^{*-} \to \overline{D}^0(\to \pi^+\pi^-)\pi_s^-$, (b) $D^{*+} \to D^0(\to \pi^+\pi^-)\pi_s^+$, (c) $D^{*-} \to \overline{D}^0(\to K^+K^-)\pi_s^-$ and (d) $D^{*+} \to D^0(\to K^+K^-)\pi_s^+$ candidates restricted in the decay-time bin 17 ($2.64\tau < t < 2.76\tau$), with fit projections overlaid.

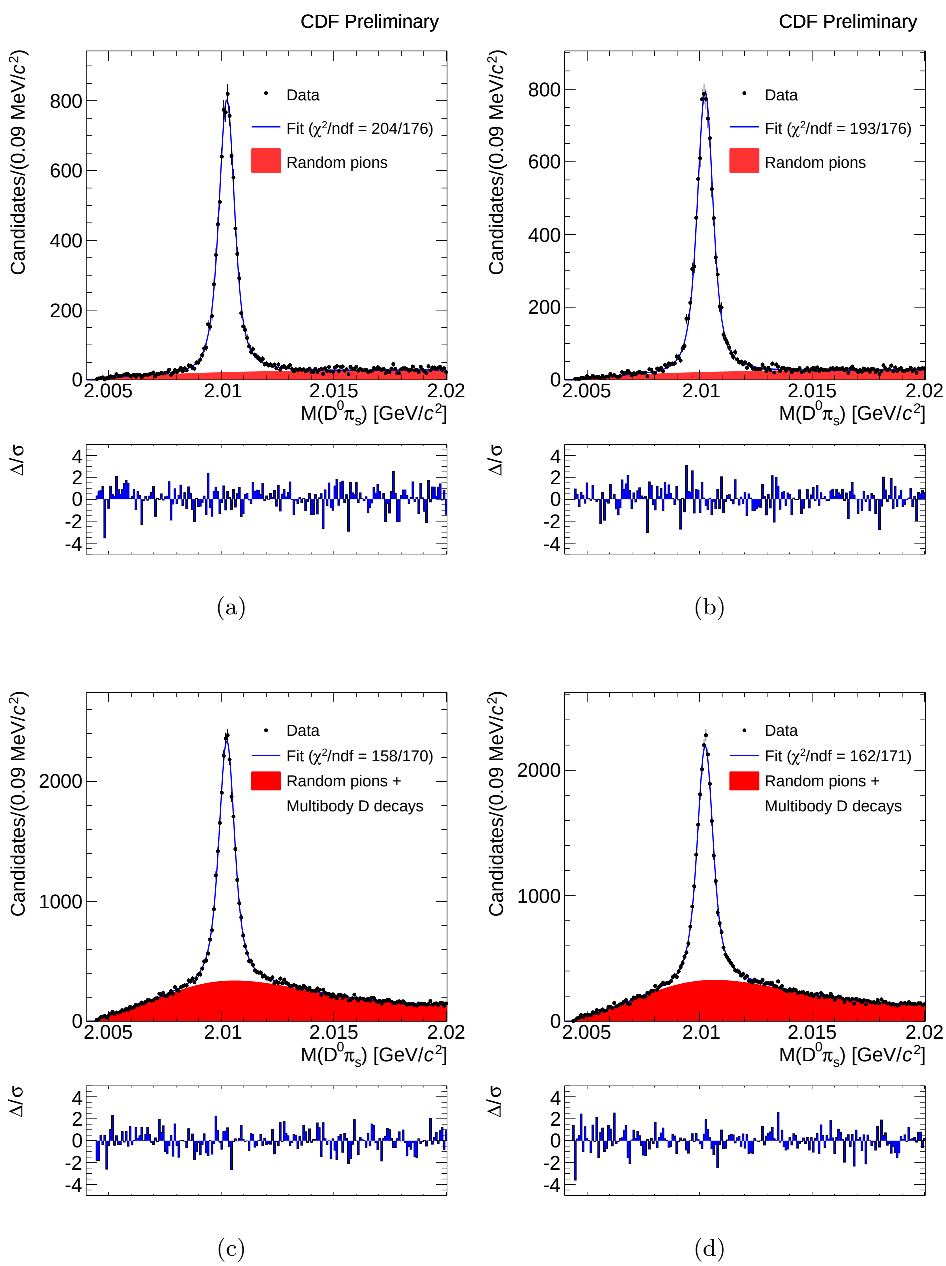

Figure 34: $D^0\pi_s$–mass distributions of (a) $D^{*-} \to \overline{D}^0(\to \pi^+\pi^-)\pi_s^-$, (b) $D^{*+} \to D^0(\to \pi^+\pi^-)\pi_s^+$, (c) $D^{*-} \to \overline{D}^0(\to K^+K^-)\pi_s^-$ and (d) $D^{*+} \to D^0(\to K^+K^-)\pi_s^+$ candidates restricted in the decay-time bin 18 ($2.76\tau < t < 2.88\tau$), with fit projections overlaid.

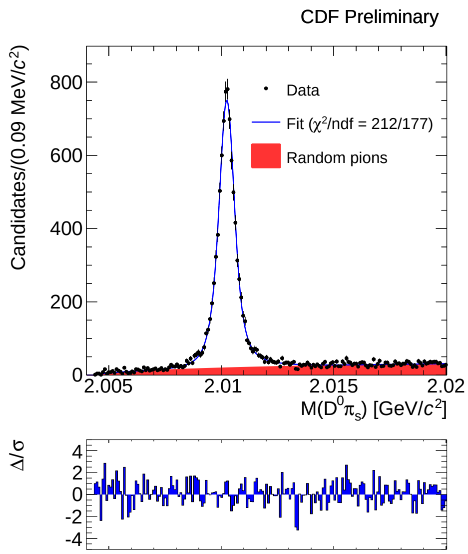

(a)

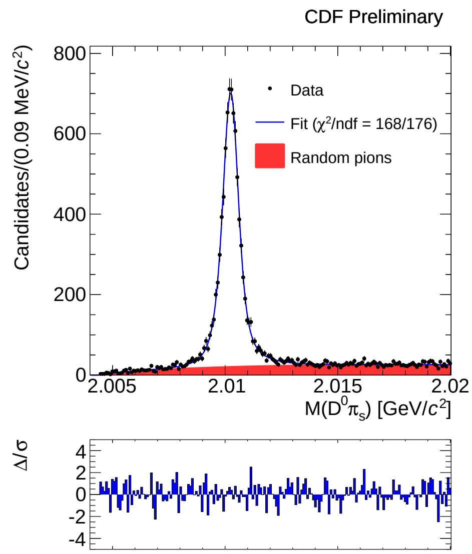

(b)

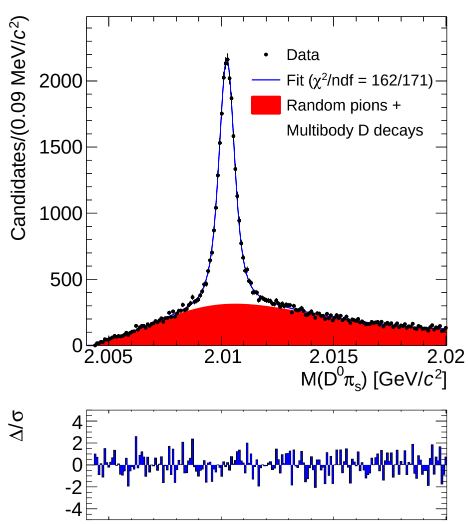

(c)

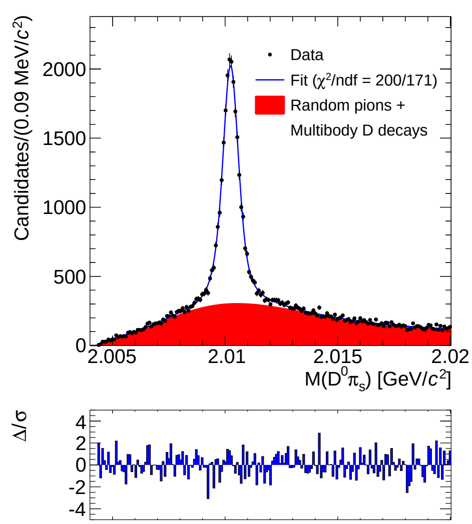

(d)

Figure 35: $D^0\pi_s$–mass distributions of (a) $D^{*-} \to \overline{D}^0(\to \pi^+\pi^-)\pi_s^-$, (b) $D^{*+} \to D^0(\to \pi^+\pi^-)\pi_s^+$, (c) $D^{*-} \to \overline{D}^0(\to K^+K^-)\pi_s^-$ and (d) $D^{*+} \to D^0(\to K^+K^-)\pi_s^+$ candidates restricted in the decay-time bin 19 ($2.88\tau < t < 3.00\tau$), with fit projections overlaid.

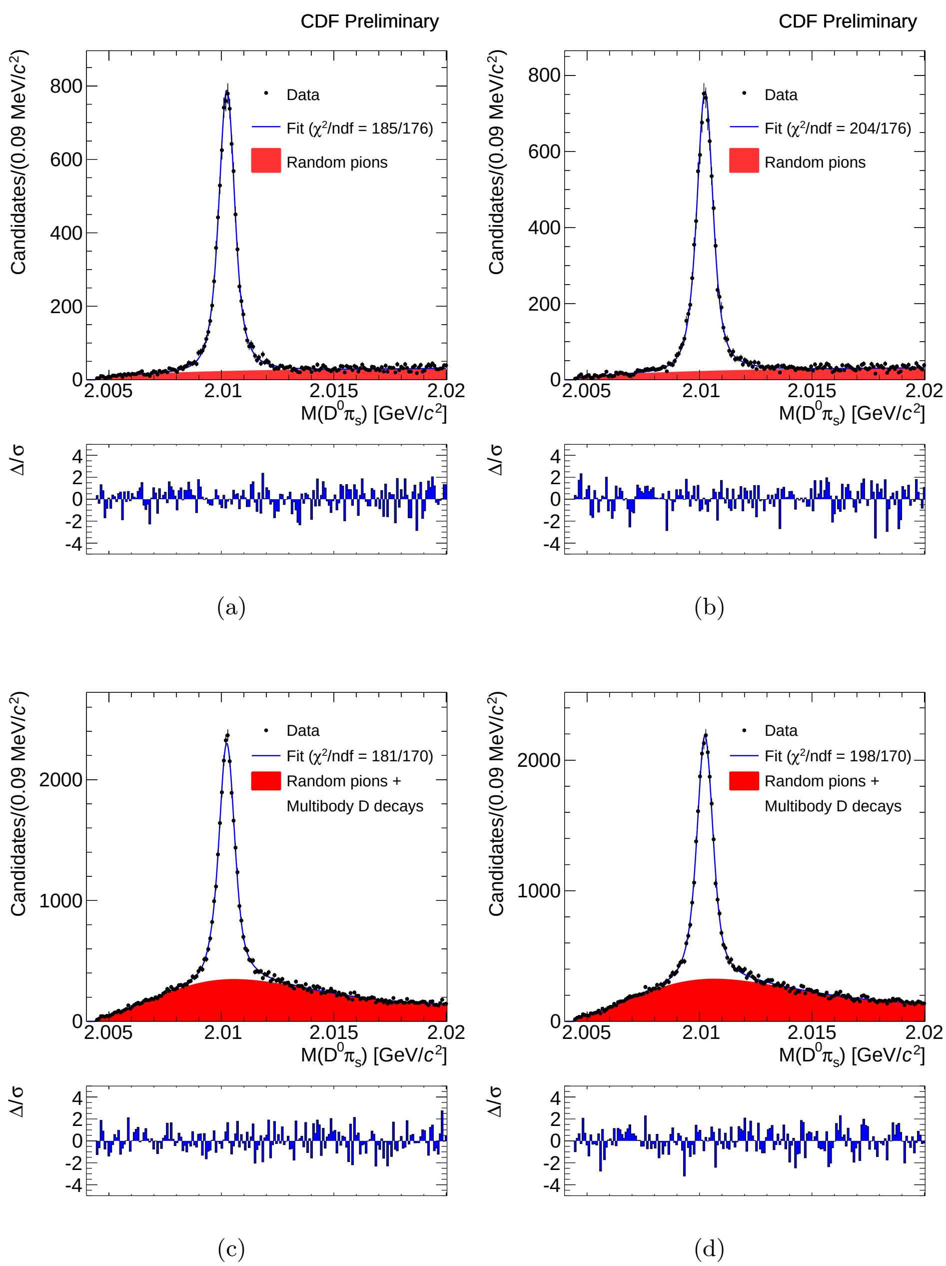

Figure 36: $D^0\pi_s$–mass distributions of (a) $D^{*-} \to \overline{D}^0(\to \pi^+\pi^-)\pi_s^-$, (b) $D^{*+} \to D^0(\to \pi^+\pi^-)\pi_s^+$, (c) $D^{*-} \to \overline{D}^0(\to K^+K^-)\pi_s^-$ and (d) $D^{*+} \to D^0(\to K^+K^-)\pi_s^+$ candidates restricted in the decay-time bin 20 ($3.00\tau < t < 3.14\tau$), with fit projections overlaid.

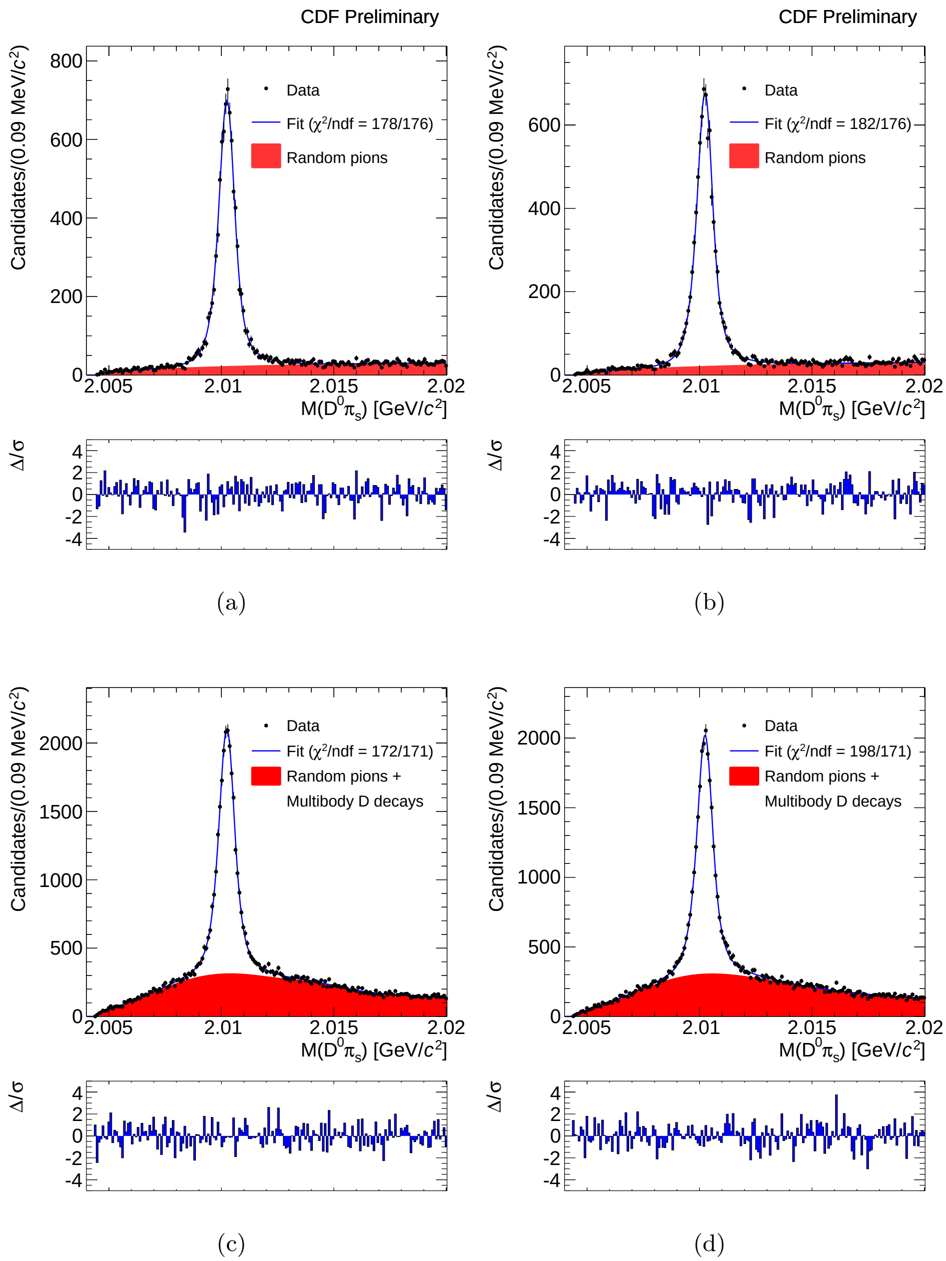

Figure 37: $D^0\pi_s$–mass distributions of (a) $D^{*-} \to \overline{D}^0(\to \pi^+\pi^-)\pi_s^-$, (b) $D^{*+} \to D^0(\to \pi^+\pi^-)\pi_s^+$, (c) $D^{*-} \to \overline{D}^0(\to K^+K^-)\pi_s^-$ and (d) $D^{*+} \to D^0(\to K^+K^-)\pi_s^+$ candidates restricted in the decay-time bin 21 ($3.14\tau < t < 3.28\tau$), with fit projections overlaid.

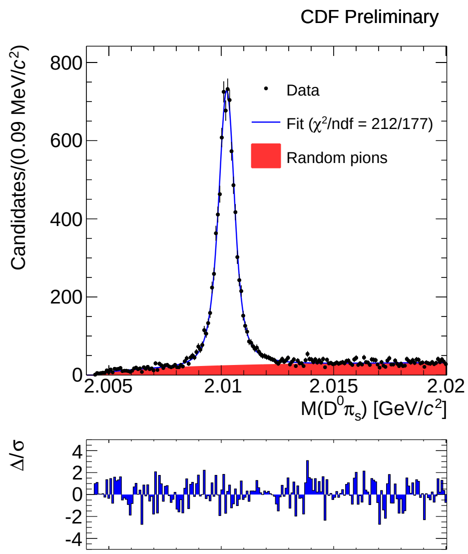

(a)

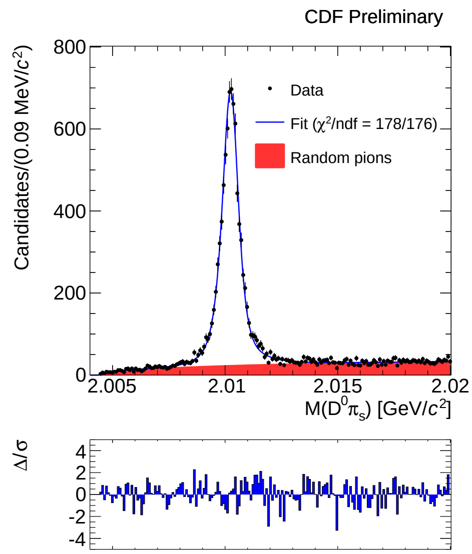

(b)

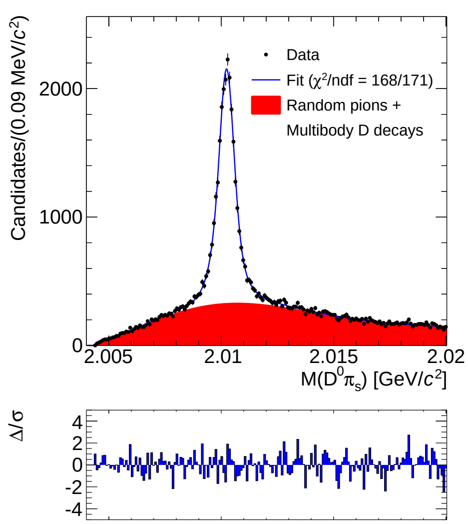

(c)

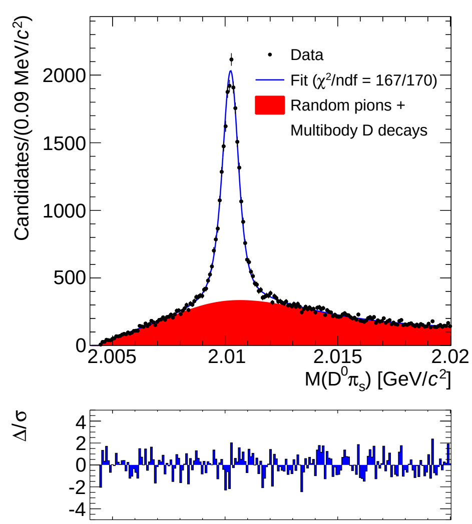

(d)

Figure 38: $D^0\pi_s$–mass distributions of (a) $D^{*-} \to \overline{D}^0(\to \pi^+\pi^-)\pi_s^-$, (b) $D^{*+} \to D^0(\to \pi^+\pi^-)\pi_s^+$, (c) $D^{*-} \to \overline{D}^0(\to K^+K^-)\pi_s^-$ and (d) $D^{*+} \to D^0(\to K^+K^-)\pi_s^+$ candidates restricted in the decay-time bin 22 ($3.28\tau < t < 3.44\tau$), with fit projections overlaid.

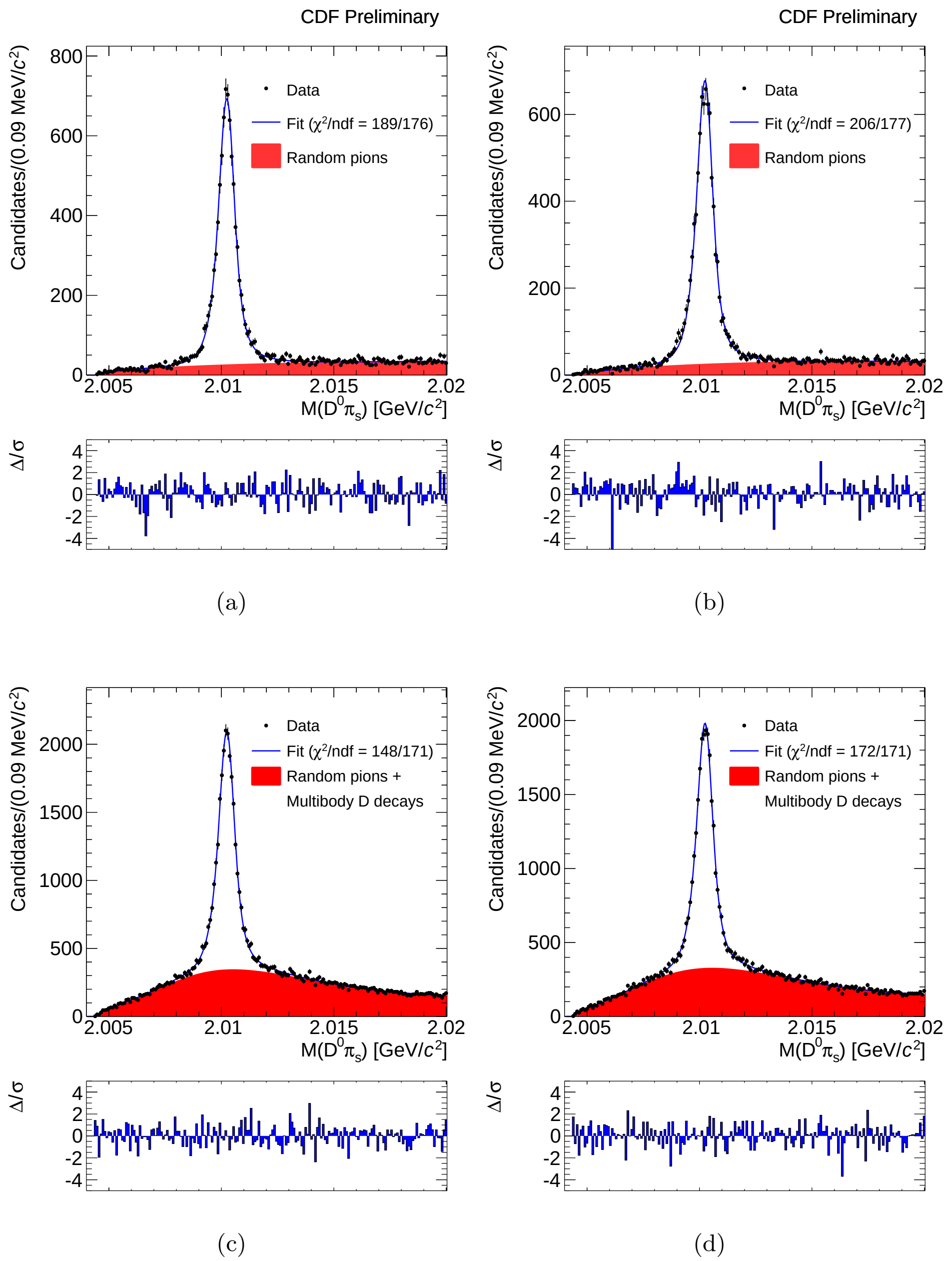

Figure 39: $D^0\pi_s$–mass distributions of (a) $D^{*-} \to \overline{D}^0(\to \pi^+\pi^-)\pi_s^-$, (b) $D^{*+} \to D^0(\to \pi^+\pi^-)\pi_s^+$, (c) $D^{*-} \to \overline{D}^0(\to K^+K^-)\pi_s^-$ and (d) $D^{*+} \to D^0(\to K^+K^-)\pi_s^+$ candidates restricted in the decay-time bin 23 ($3.44\tau < t < 3.62\tau$), with fit projections overlaid.

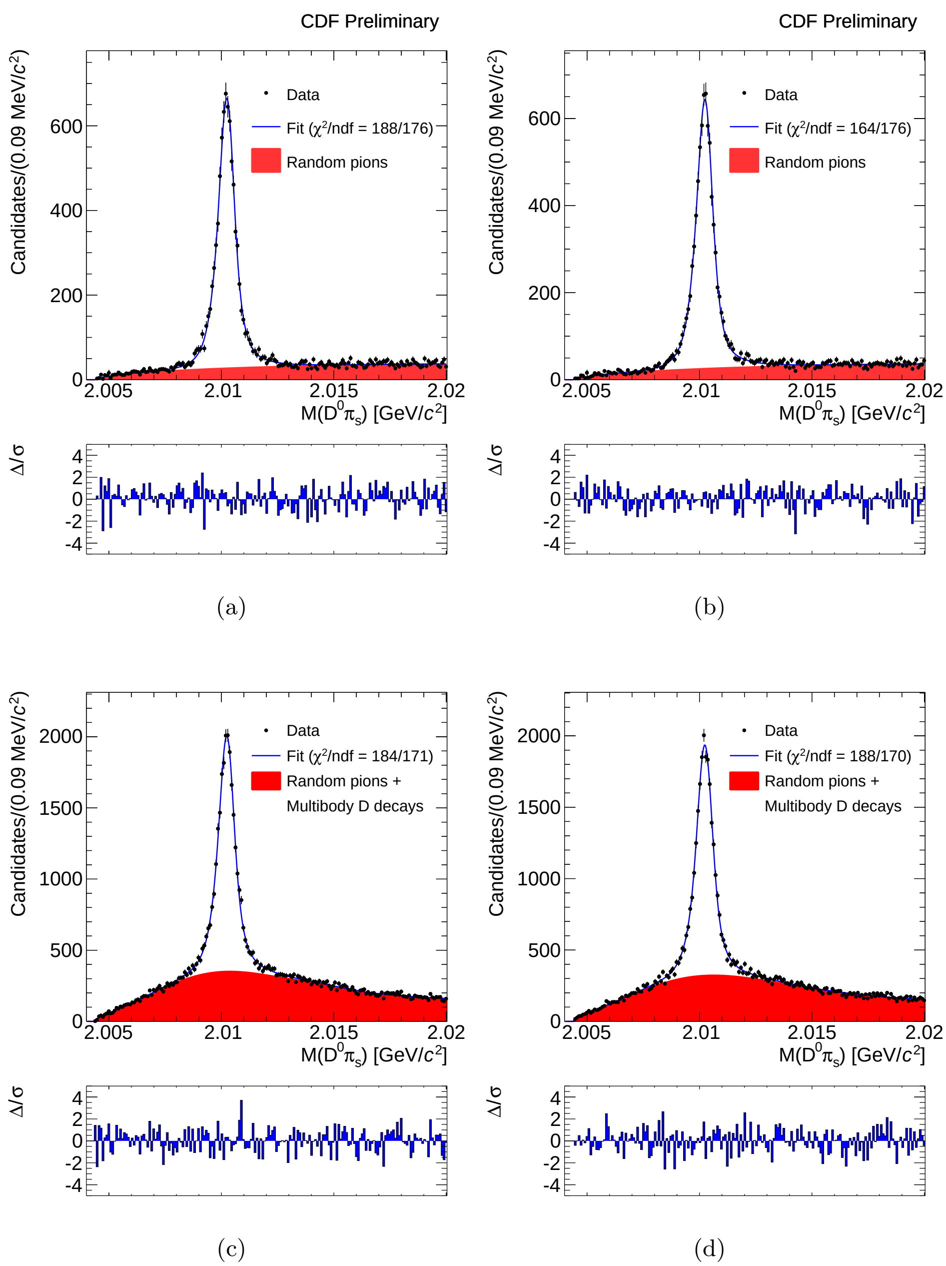

Figure 40: $D^0\pi_s$–mass distributions of (a) $D^{*-} \to \overline{D}^0(\to \pi^+\pi^-)\pi_s^-$, (b) $D^{*+} \to D^0(\to \pi^+\pi^-)\pi_s^+$, (c) $D^{*-} \to \overline{D}^0(\to K^+K^-)\pi_s^-$ and (d) $D^{*+} \to D^0(\to K^+K^-)\pi_s^+$ candidates restricted in the decay-time bin 24 ($3.62\tau < t < 3.82\tau$), with fit projections overlaid.

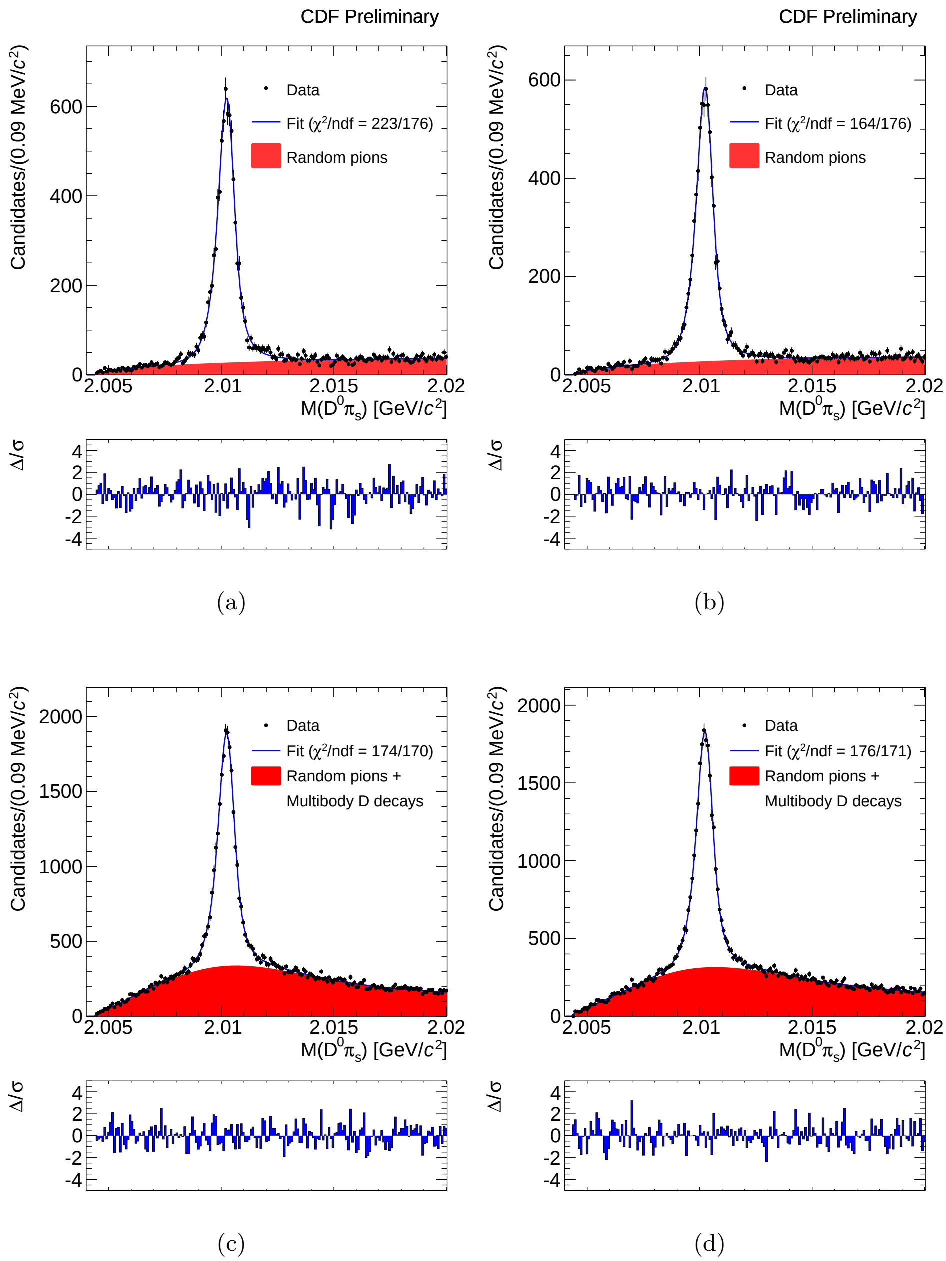

Figure 41: $D^0\pi_s$–mass distributions of (a) $D^{*-} \to \overline{D}^0(\to \pi^+\pi^-)\pi_s^-$, (b) $D^{*+} \to D^0(\to \pi^+\pi^-)\pi_s^+$, (c) $D^{*-} \to \overline{D}^0(\to K^+K^-)\pi_s^-$ and (d) $D^{*+} \to D^0(\to K^+K^-)\pi_s^+$ candidates restricted in the decay-time bin 25 ($3.82\tau < t < 4.04\tau$), with fit projections overlaid.

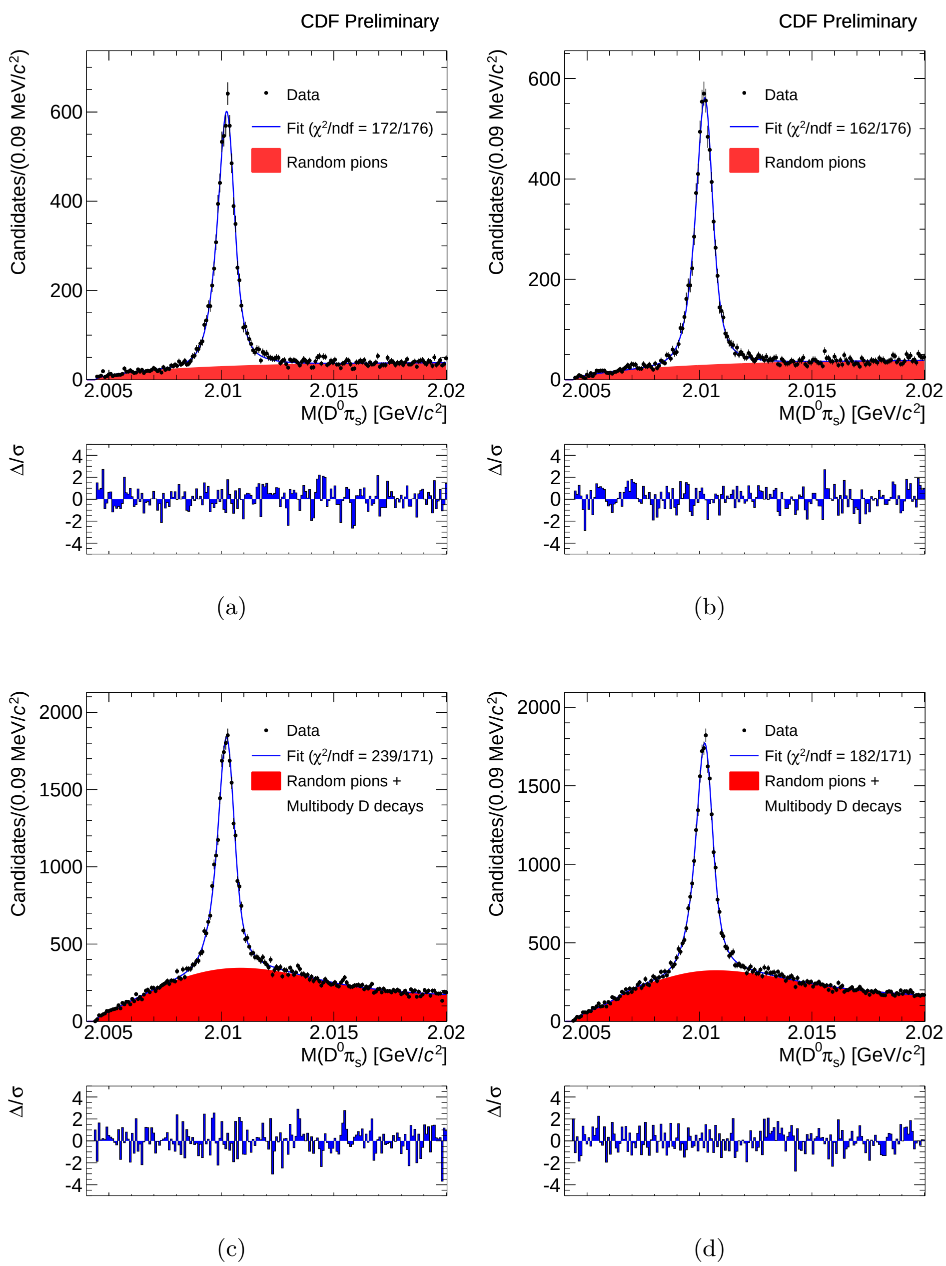

Figure 42: $D^0\pi_s$–mass distributions of (a) $D^{*-} \to \overline{D}^0(\to \pi^+\pi^-)\pi_s^-$, (b) $D^{*+} \to D^0(\to \pi^+\pi^-)\pi_s^+$, (c) $D^{*-} \to \overline{D}^0(\to K^+K^-)\pi_s^-$ and (d) $D^{*+} \to D^0(\to K^+K^-)\pi_s^+$ candidates restricted in the decay-time bin 26 ($4.04\tau < t < 4.30\tau$), with fit projections overlaid.

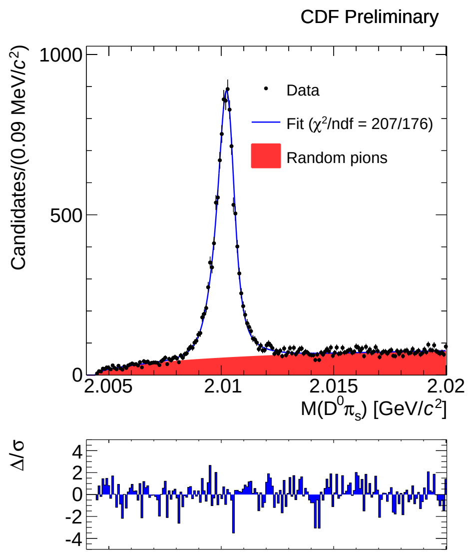

(a)

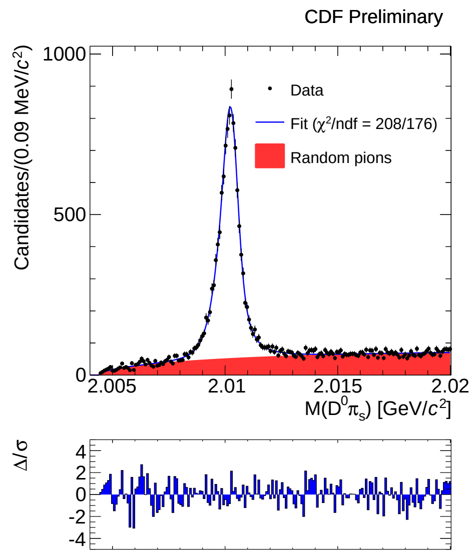

(b)

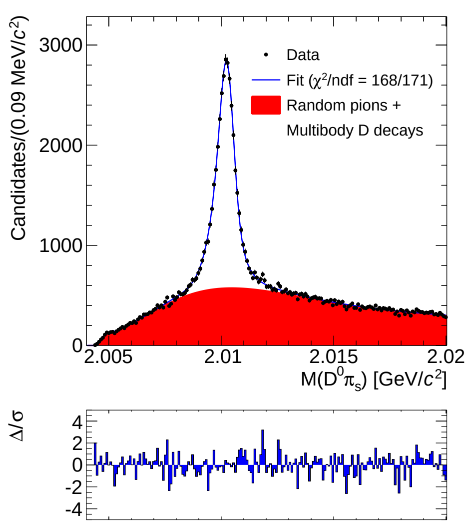

(c)

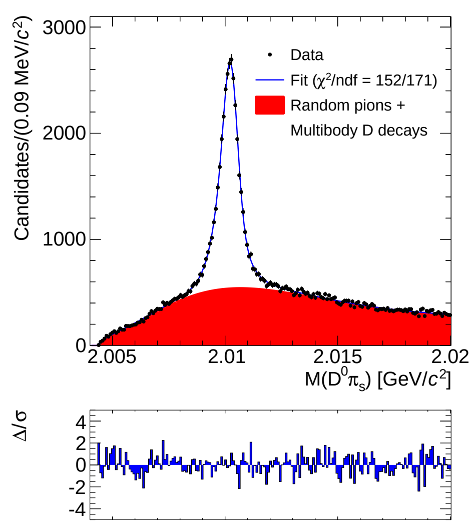

(d)

Figure 43: $D^0\pi_s$–mass distributions of (a) $D^{*-} \rightarrow \overline{D}^0(\rightarrow \pi^+\pi^-)\pi_s^-$, (b) $D^{*+} \rightarrow D^0(\rightarrow \pi^+\pi^-)\pi_s^+$, (c) $D^{*-} \rightarrow \overline{D}^0(\rightarrow K^+K^-)\pi_s^-$ and (d) $D^{*+} \rightarrow D^0(\rightarrow K^+K^-)\pi_s^+$ candidates restricted in the decay-time bin 27 ($4.30\tau < t < 4.98\tau$), with fit projections overlaid.

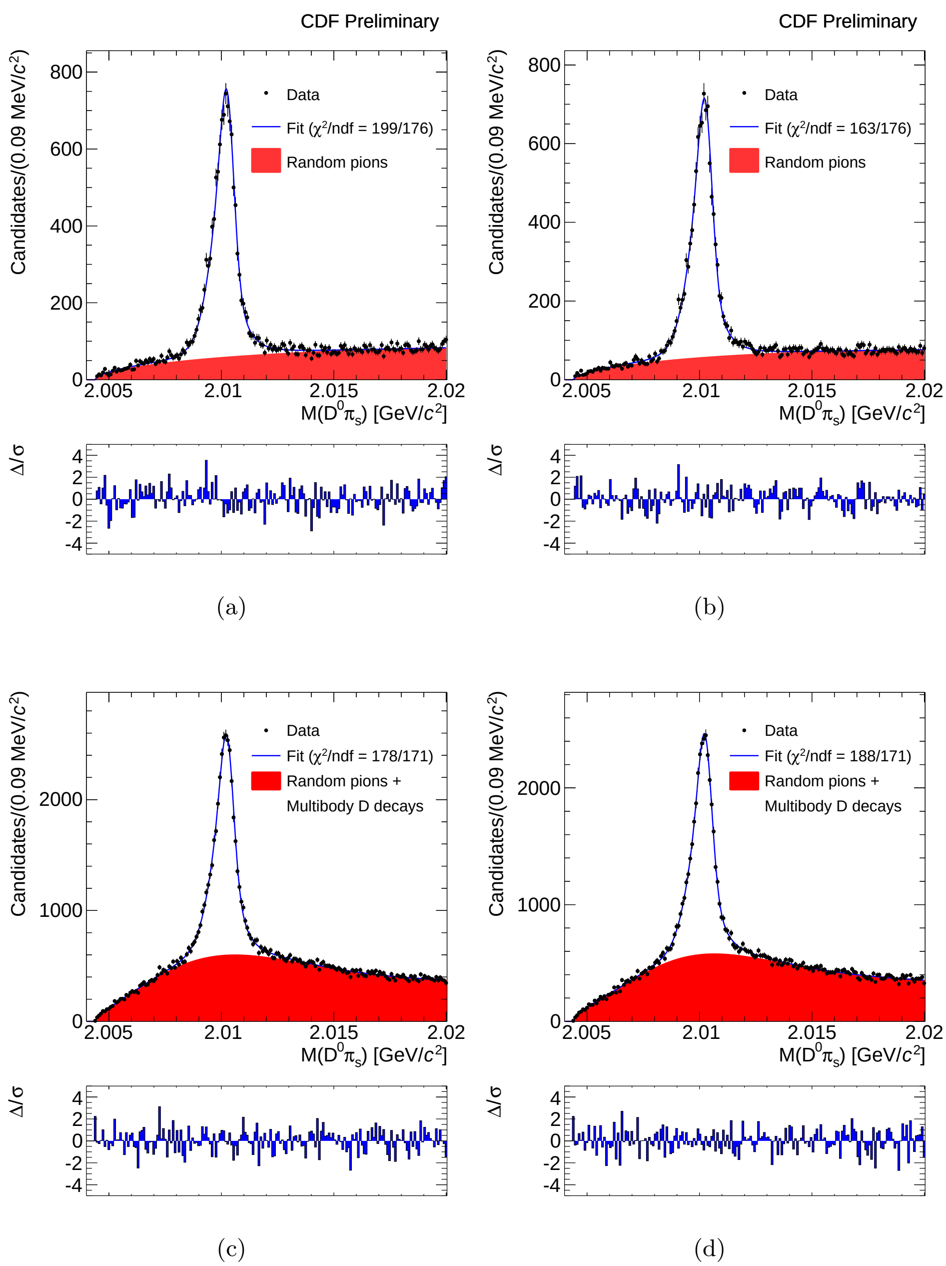

Figure 44: $D^0\pi_s$–mass distributions of (a) $D^{*-} \rightarrow \overline{D}^0(\rightarrow \pi^+\pi^-)\pi_s^-$, (b) $D^{*+} \rightarrow D^0(\rightarrow \pi^+\pi^-)\pi_s^+$, (c) $D^{*-} \rightarrow \overline{D}^0(\rightarrow K^+K^-)\pi_s^-$ and (d) $D^{*+} \rightarrow D^0(\rightarrow K^+K^-)\pi_s^+$ candidates restricted in the decay-time bin 28 ($4.98\tau < t < 6.16\tau$), with fit projections overlaid.

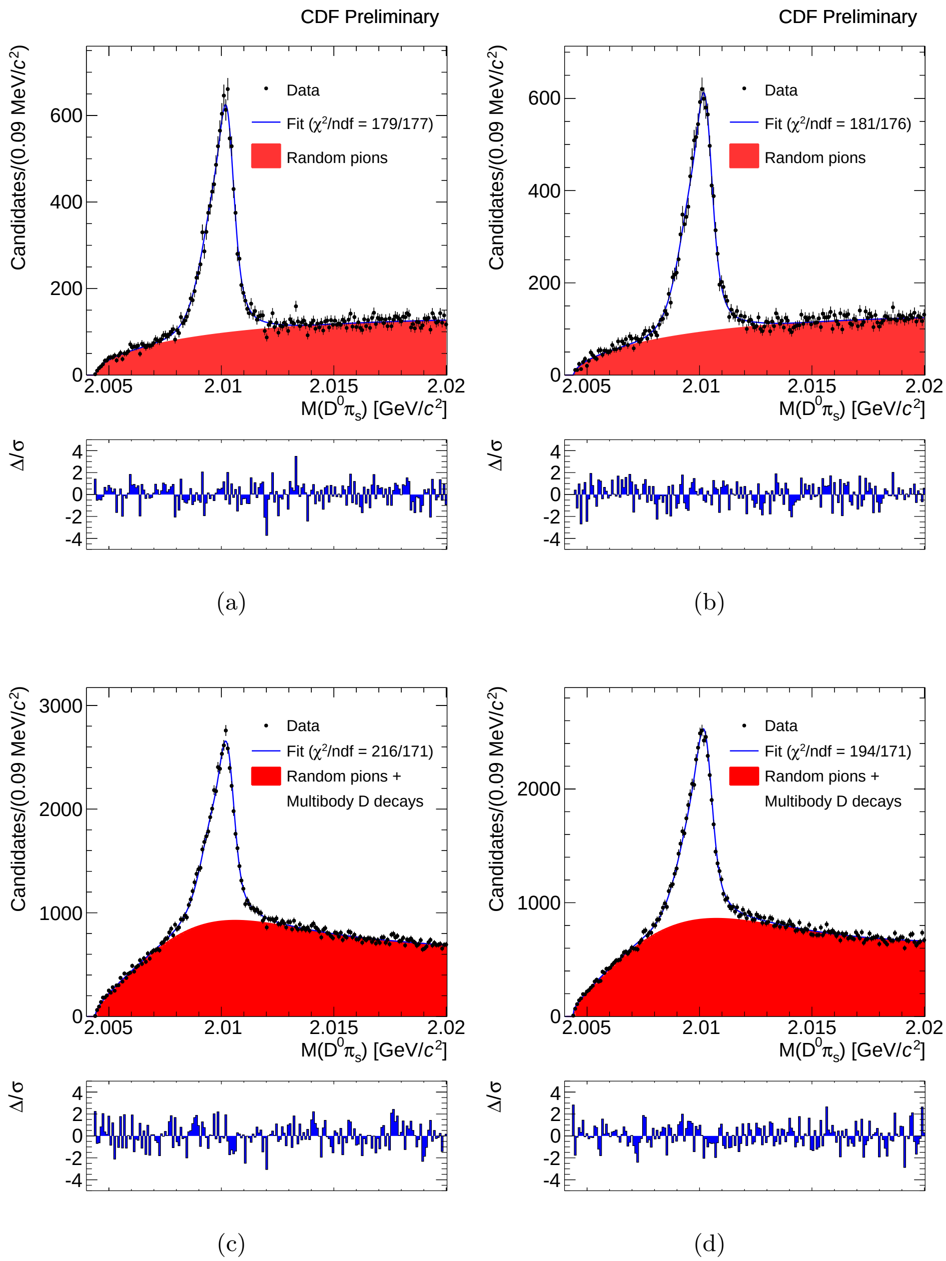

Figure 45: $D^0\pi_s$–mass distributions of (a) $D^{*-} \to \overline{D}^0(\to \pi^+\pi^-)\pi_s^-$, (b) $D^{*+} \to D^0(\to \pi^+\pi^-)\pi_s^+$, (c) $D^{*-} \to \overline{D}^0(\to K^+K^-)\pi_s^-$ and (d) $D^{*+} \to D^0(\to K^+K^-)\pi_s^+$ candidates restricted in the decay-time bin 29 ($6.16\tau < t < 20\tau$), with fit projections overlaid.

B Detailed impact parameter fit projections

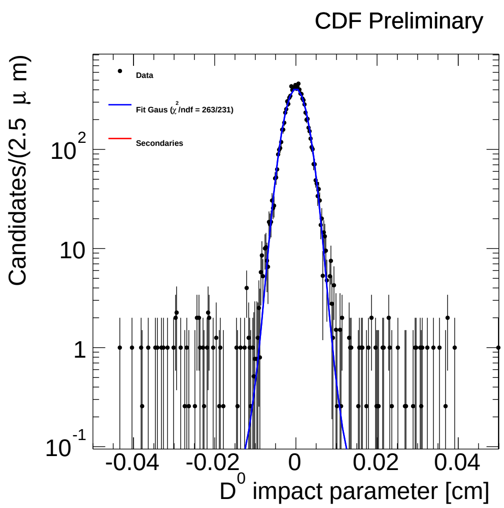

(a)

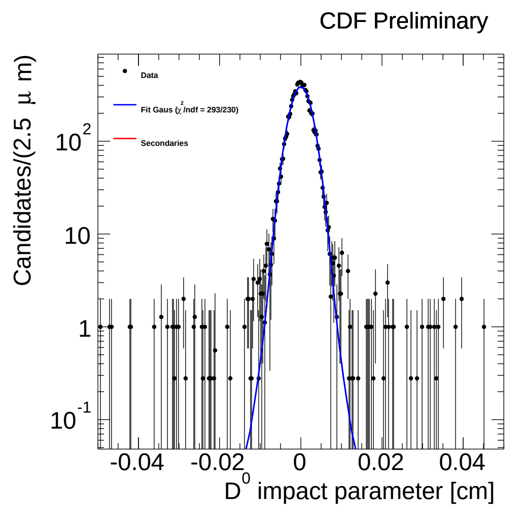

(b)

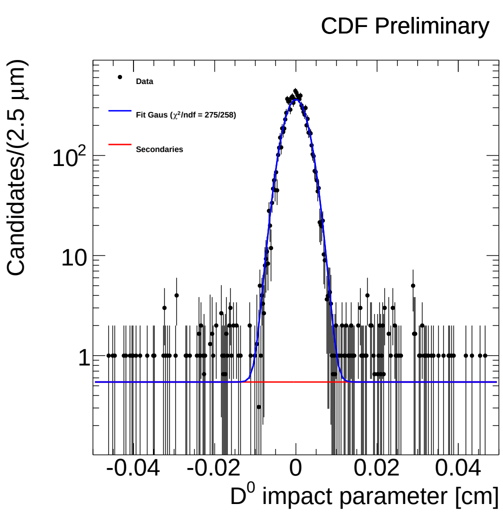

(c)

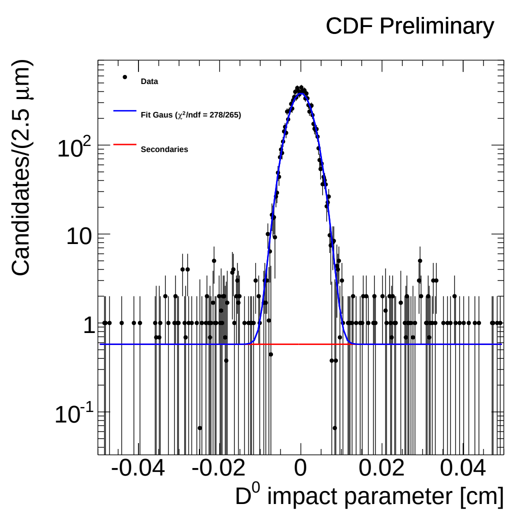

(d)

Figure 46: Impact parameter distributions of (a) $D^{*-} \rightarrow \overline{D}^0(\rightarrow \pi^+\pi^-)\pi_s^-$, (b) $D^{*+} \rightarrow D^0(\rightarrow \pi^+\pi^-)\pi_s^+$, (c) $D^{*-} \rightarrow \overline{D}^0(\rightarrow K^+K^-)\pi_s^-$ and (d) $D^{*+} \rightarrow D^0(\rightarrow K^+K^-)\pi_s^+$ candidates restricted in the decay-time bin 1, with fit projections overlaid.

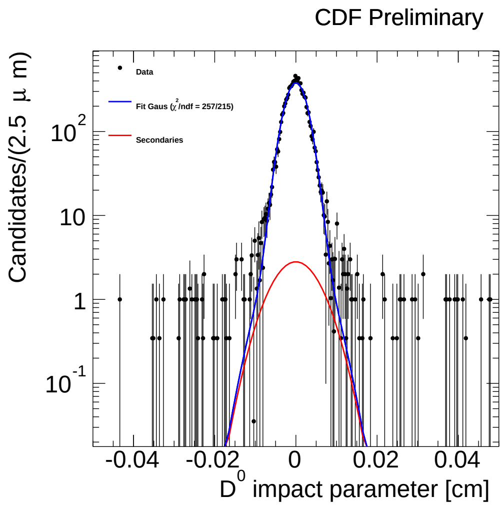

(a)

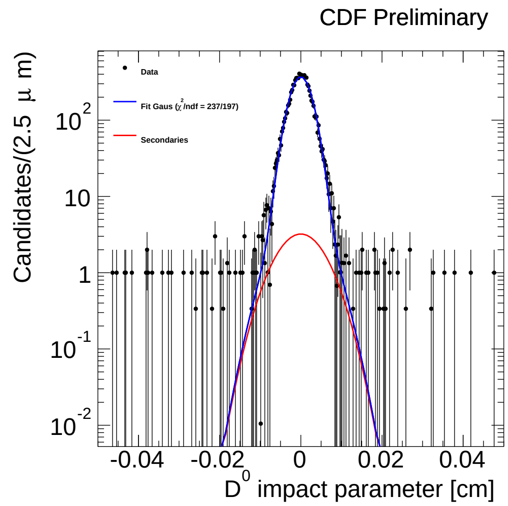

(b)

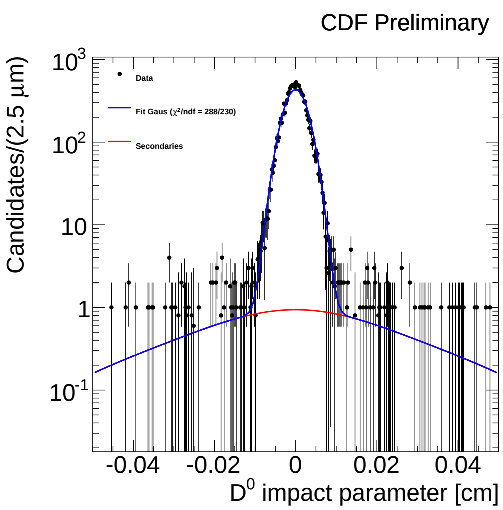

(c)

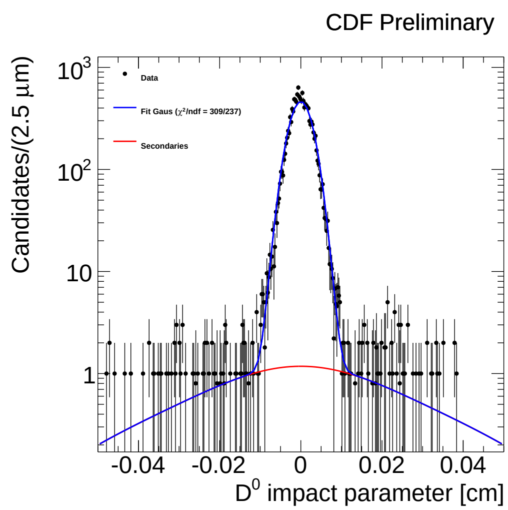

(d)

Figure 47: Impact parameter distributions of (a) $D^{*-} \to \overline{D}^0(\to \pi^+\pi^-)\pi_s^-$, (b) $D^{*+} \to D^0(\to \pi^+\pi^-)\pi_s^+$, (c) $D^{*-} \to \overline{D}^0(\to K^+K^-)\pi_s^-$ and (d) $D^{*+} \to D^0(\to K^+K^-)\pi_s^+$ candidates restricted in the decay-time bin 2, with fit projections overlaid.

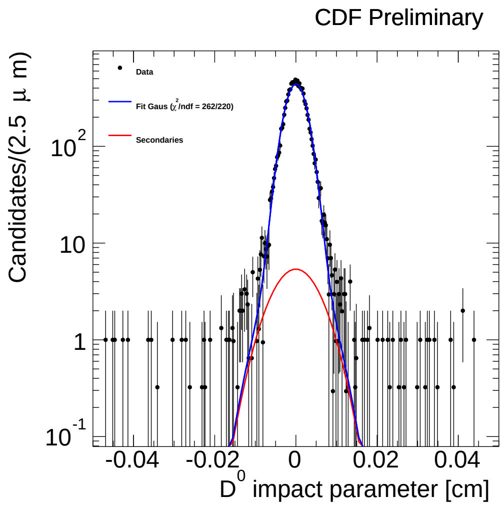

(a)

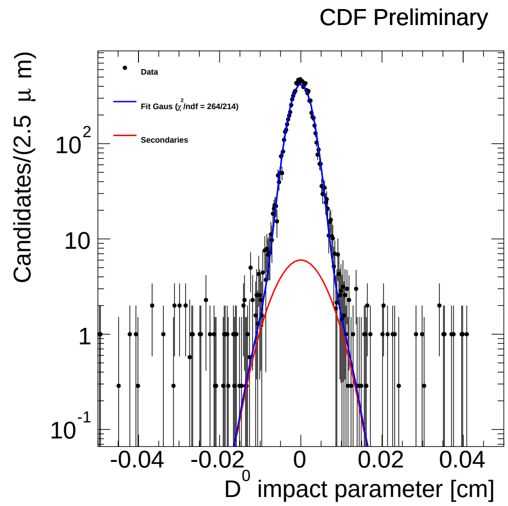

(b)

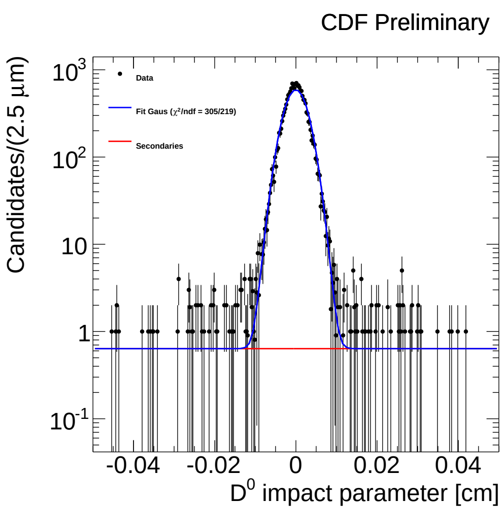

(c)

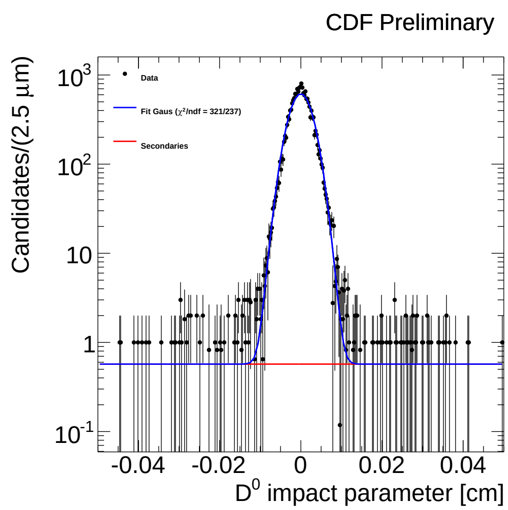

(d)

Figure 48: Impact parameter distributions of (a) $D^{*-} \to \overline{D}^0(\to \pi^+\pi^-)\pi_s^-$, (b) $D^{*+} \to D^0(\to \pi^+\pi^-)\pi_s^+$, (c) $D^{*-} \to \overline{D}^0(\to K^+K^-)\pi_s^-$ and (d) $D^{*+} \to D^0(\to K^+K^-)\pi_s^+$ candidates restricted in the decay-time bin 3, with fit projections overlaid.

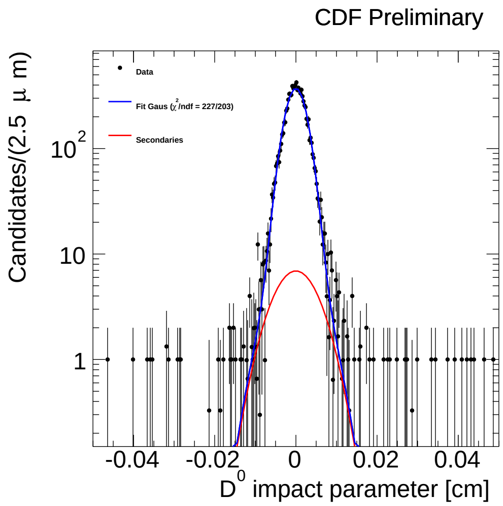

(a)

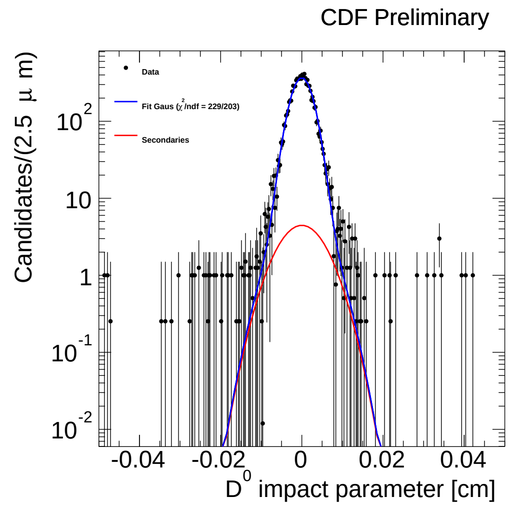

(b)

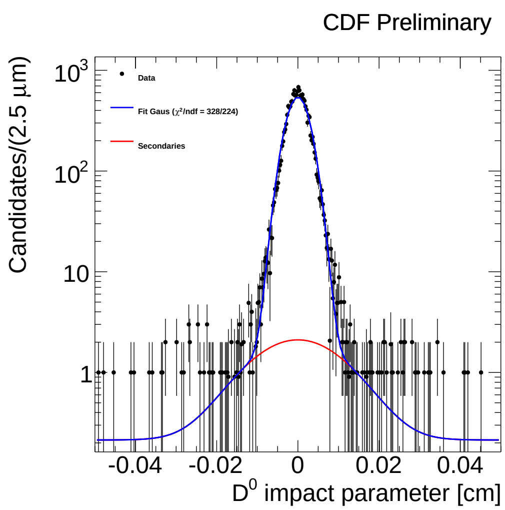

(c)

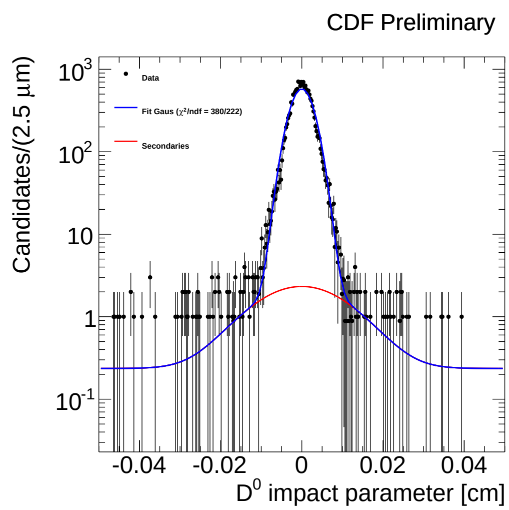

(d)

Figure 49: Impact parameter distributions of (a) $D^{*-} \to \overline{D}^0(\to \pi^+\pi^-)\pi_s^-$, (b) $D^{*+} \to D^0(\to \pi^+\pi^-)\pi_s^+$, (c) $D^{*-} \to \overline{D}^0(\to K^+K^-)\pi_s^-$ and (d) $D^{*+} \to D^0(\to K^+K^-)\pi_s^+$ candidates restricted in the decay-time bin 4, with fit projections overlaid.

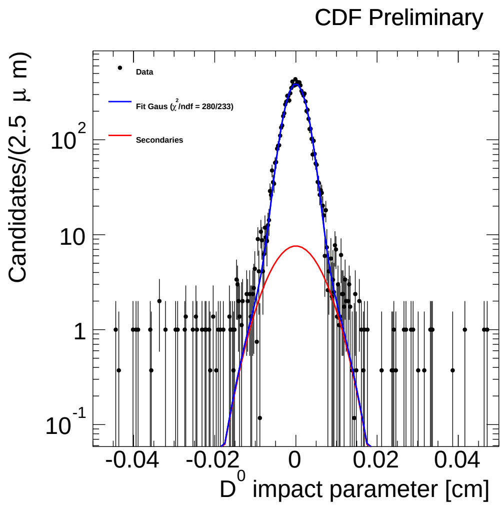

(a)

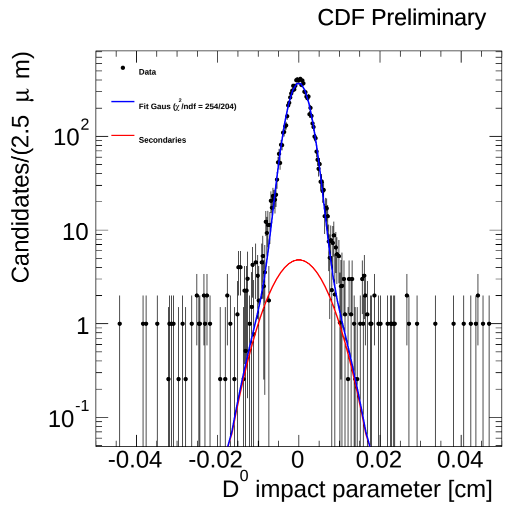

(b)

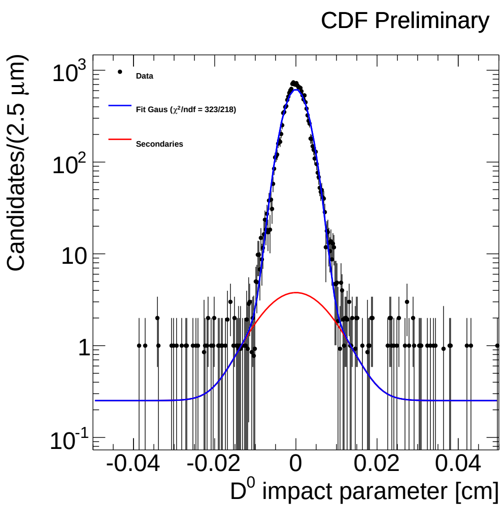

(c)

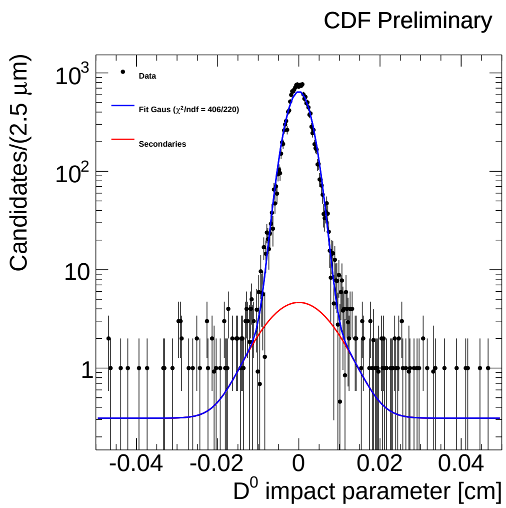

(d)

Figure 50: Impact parameter distributions of (a) $D^{*-} \to \overline{D}^0(\to \pi^+\pi^-)\pi_s^-$, (b) $D^{*+} \to D^0(\to \pi^+\pi^-)\pi_s^+$, (c) $D^{*-} \to \overline{D}^0(\to K^+K^-)\pi_s^-$ and (d) $D^{*+} \to D^0(\to K^+K^-)\pi_s^+$ candidates restricted in the decay-time bin 5, with fit projections overlaid.

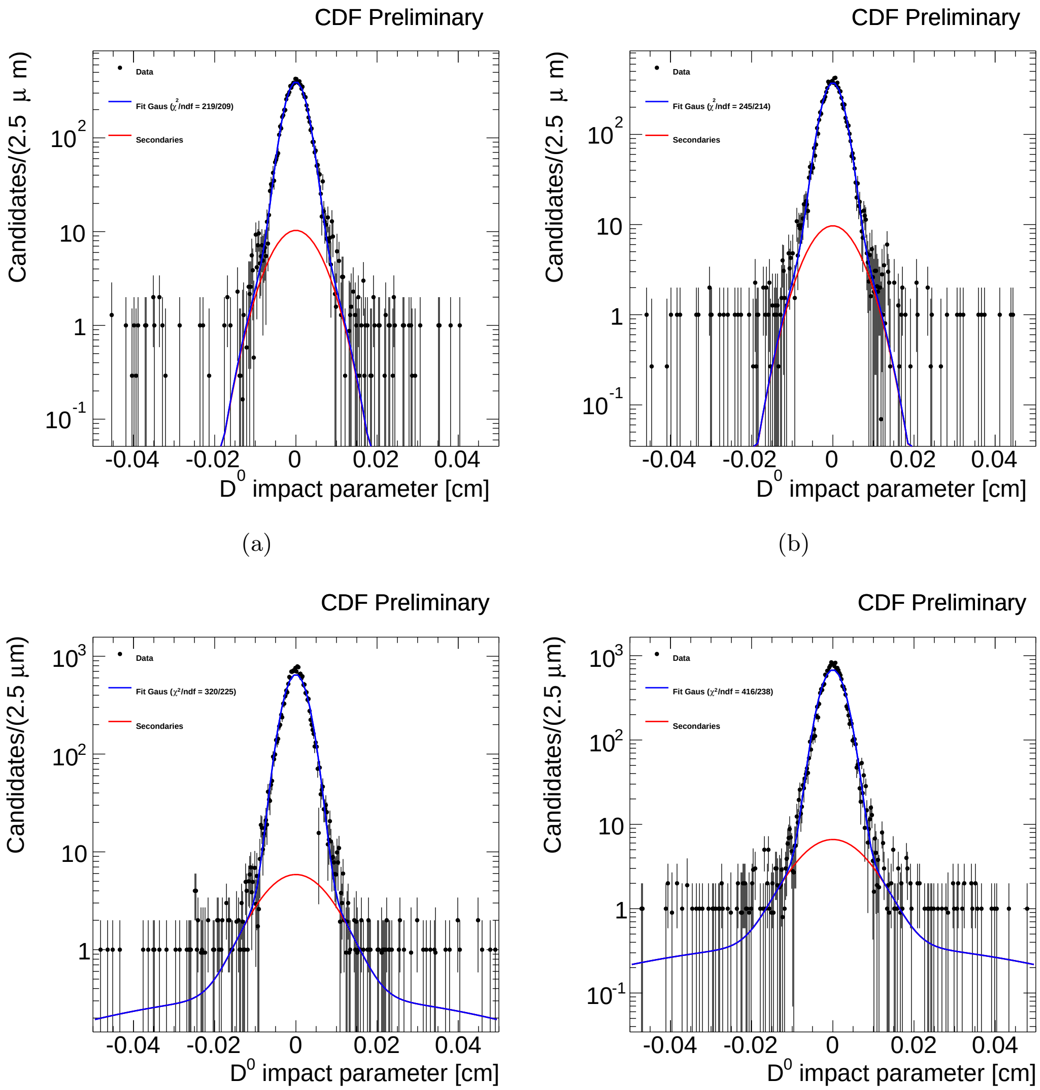

(a) (b) (c) (d)

Figure 51: Impact parameter distributions of (a) $D^{*-} \to \overline{D}^0(\to \pi^+\pi^-)\pi_s^-$, (b) $D^{*+} \to D^0(\to \pi^+\pi^-)\pi_s^+$, (c) $D^{*-} \to \overline{D}^0(\to K^+K^-)\pi_s^-$ and (d) $D^{*+} \to D^0(\to K^+K^-)\pi_s^+$ candidates restricted in the decay-time bin 6, with fit projections overlaid.

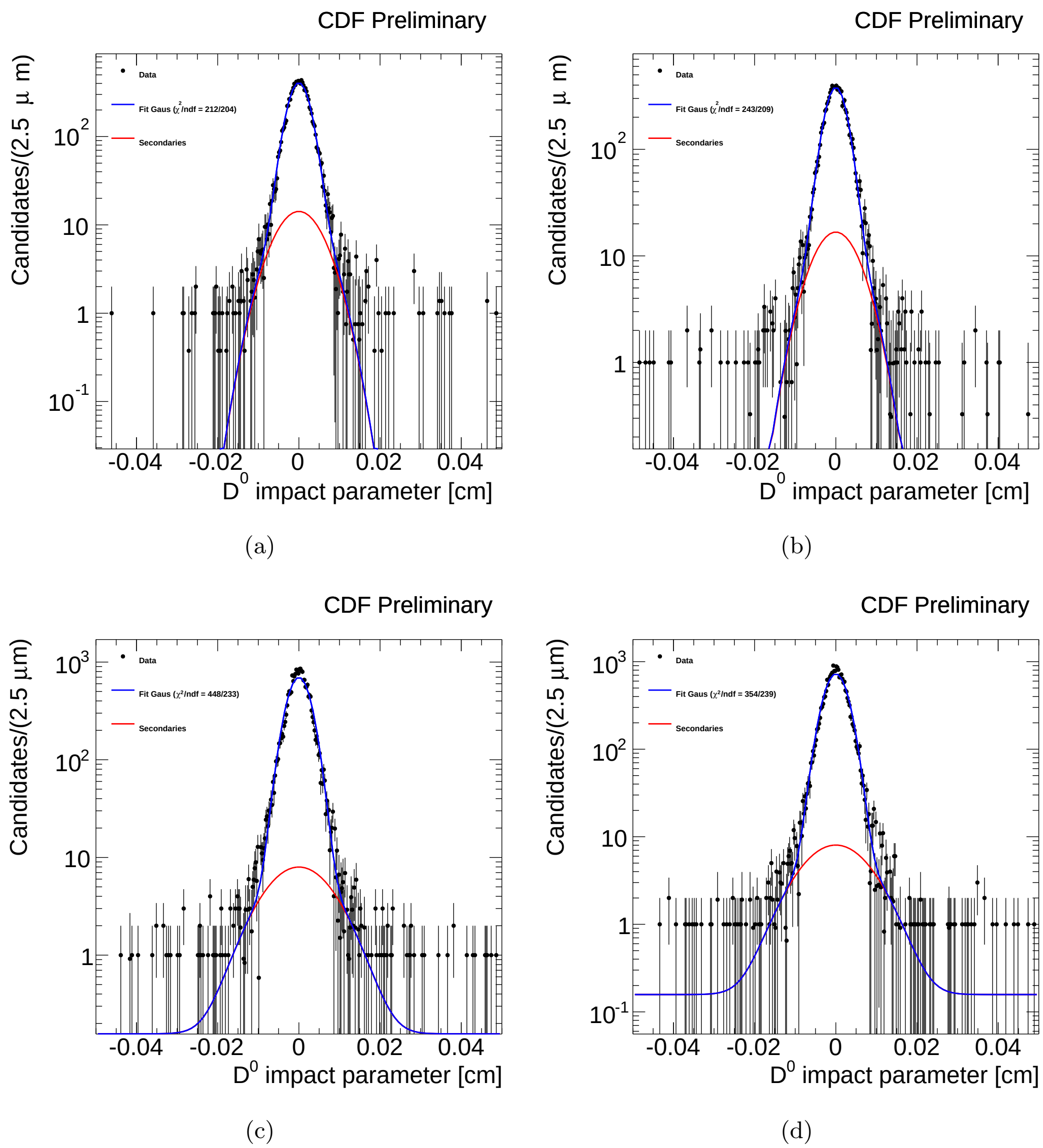

Figure 52: Impact parameter distributions of (a) $D^{*-} \to \overline{D}^0(\to \pi^+\pi^-)\pi_s^-$, (b) $D^{*+} \to D^0(\to \pi^+\pi^-)\pi_s^+$, (c) $D^{*-} \to \overline{D}^0(\to K^+K^-)\pi_s^-$ and (d) $D^{*+} \to D^0(\to K^+K^-)\pi_s^+$ candidates restricted in the decay-time bin 7, with fit projections overlaid.

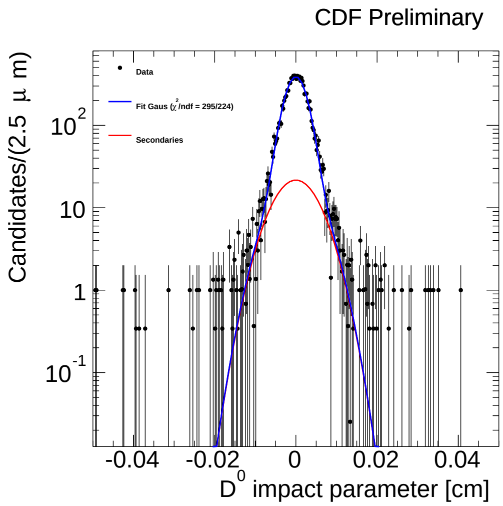

(a)

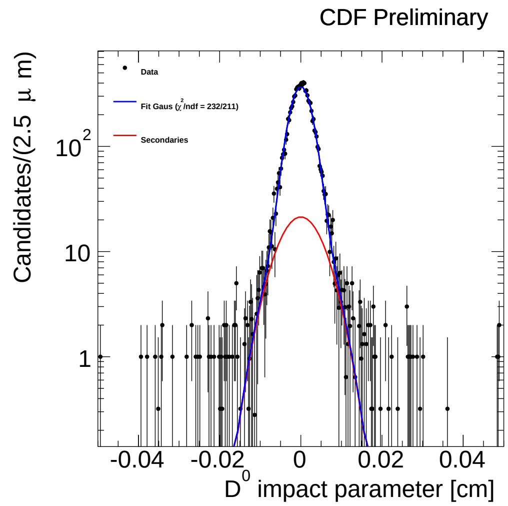

(b)

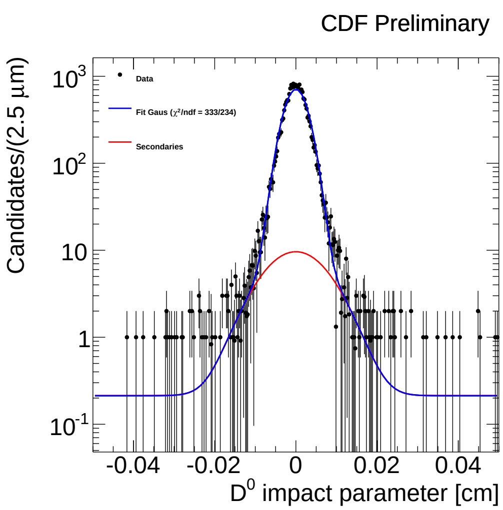

(c)

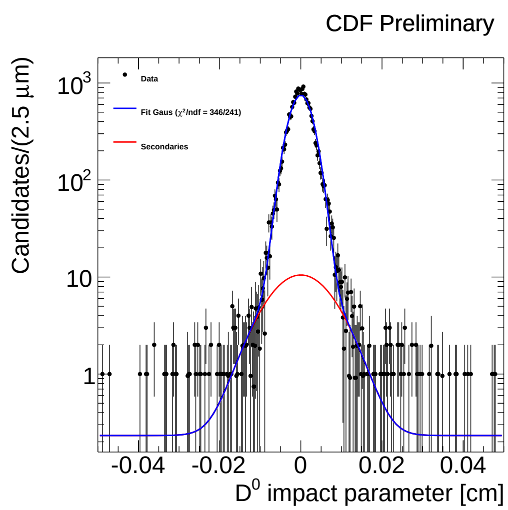

(d)

Figure 53: Impact parameter distributions of (a) $D^{*-} \to \overline{D}^0(\to \pi^+\pi^-)\pi_s^-$, (b) $D^{*+} \to D^0(\to \pi^+\pi^-)\pi_s^+$, (c) $D^{*-} \to \overline{D}^0(\to K^+K^-)\pi_s^-$ and (d) $D^{*+} \to D^0(\to K^+K^-)\pi_s^+$ candidates restricted in the decay-time bin 8, with fit projections overlaid.

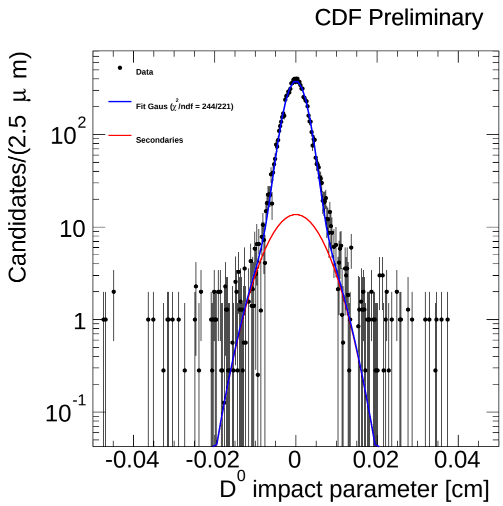

(a)

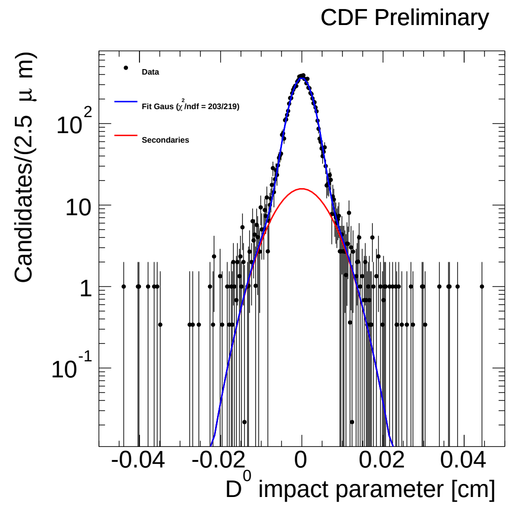

(b)

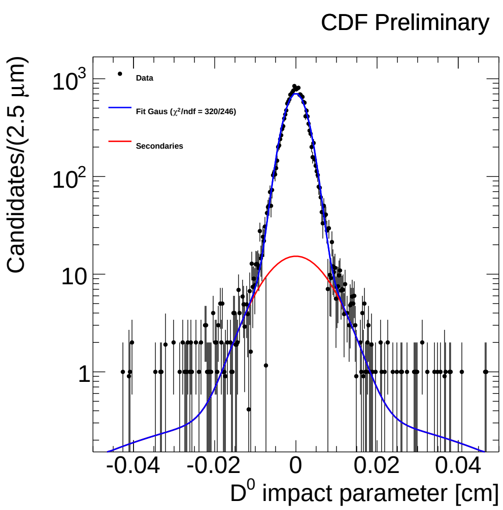

(c)

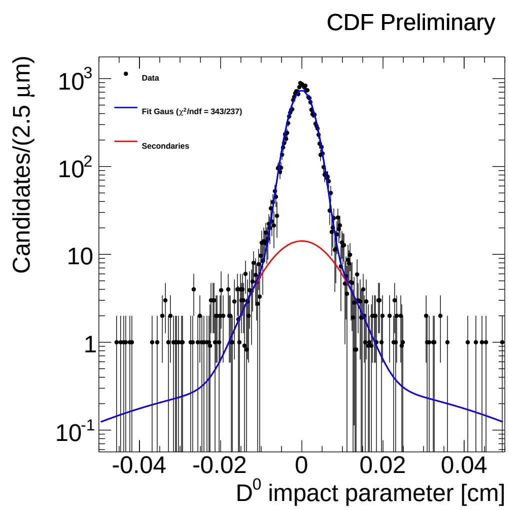

(d)

Figure 54: Impact parameter distributions of (a) $D^{*-} \to \overline{D}^0(\to \pi^+\pi^-)\pi_s^-$, (b) $D^{*+} \to D^0(\to \pi^+\pi^-)\pi_s^+$, (c) $D^{*-} \to \overline{D}^0(\to K^+K^-)\pi_s^-$ and (d) $D^{*+} \to D^0(\to K^+K^-)\pi_s^+$ candidates restricted in the decay-time bin 9, with fit projections overlaid.

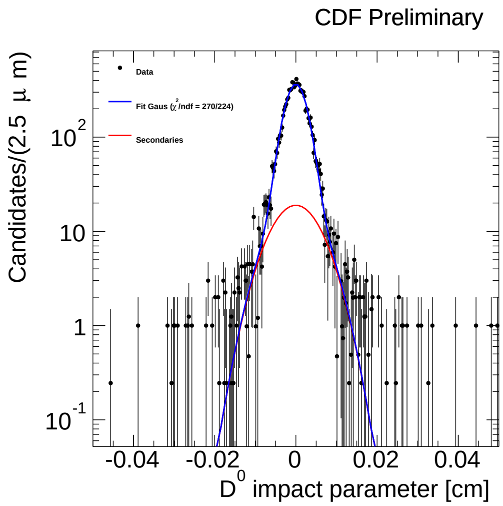

(a)

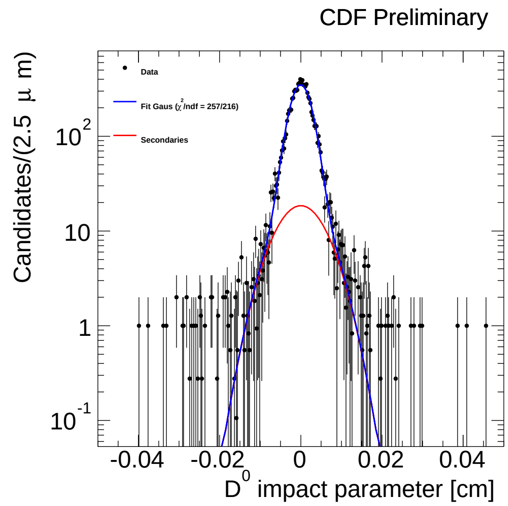

(b)

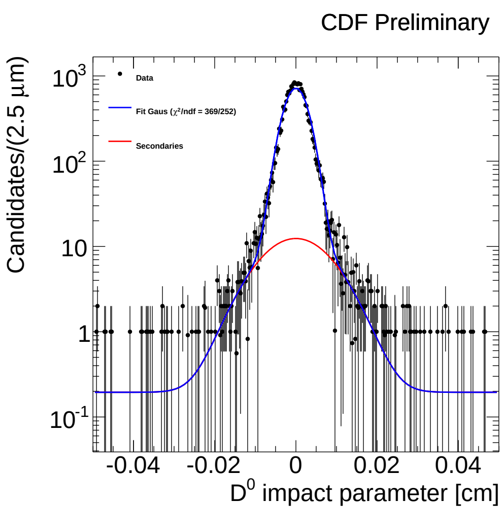

(c)

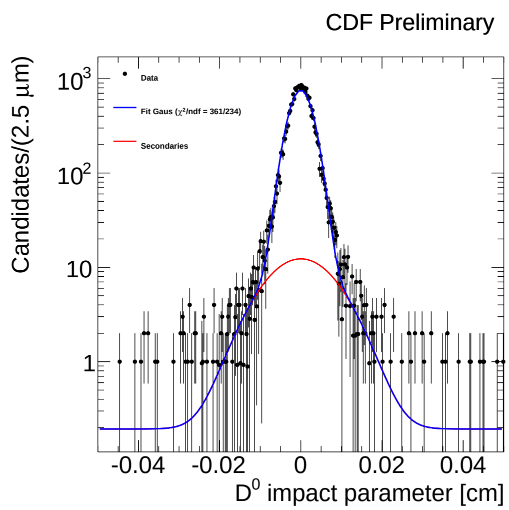

(d)

Figure 55: Impact parameter distributions of (a) $D^{*-} \rightarrow \overline{D}^0(\rightarrow \pi^+\pi^-)\pi_s^-$, (b) $D^{*+} \rightarrow D^0(\rightarrow \pi^+\pi^-)\pi_s^+$, (c) $D^{*-} \rightarrow \overline{D}^0(\rightarrow K^+K^-)\pi_s^-$ and (d) $D^{*+} \rightarrow D^0(\rightarrow K^+K^-)\pi_s^+$ candidates restricted in the decay-time bin 10, with fit projections overlaid.

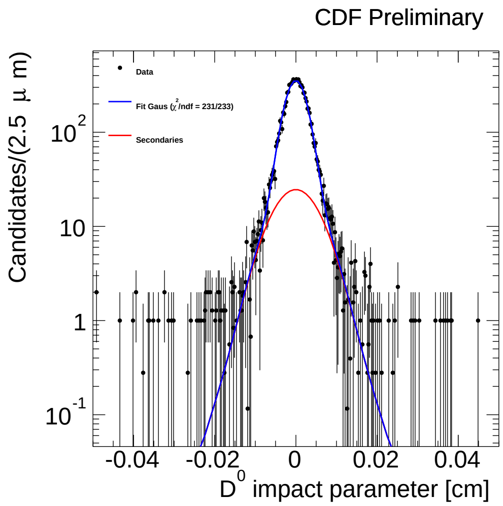

(a)

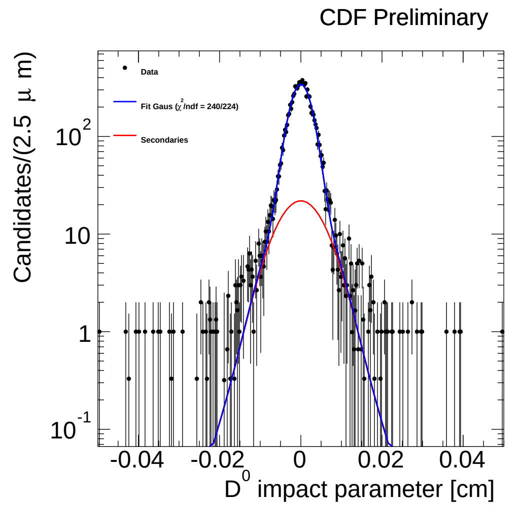

(b)

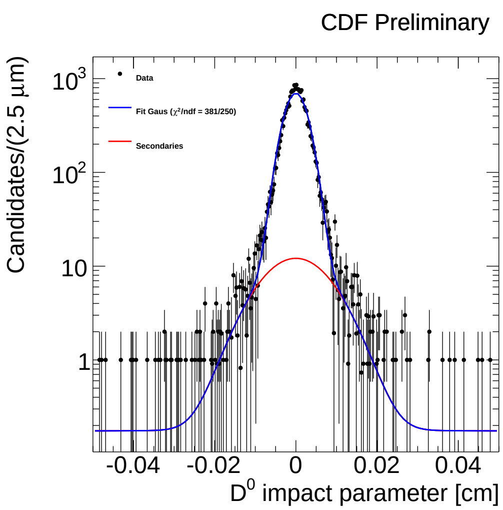

(c)

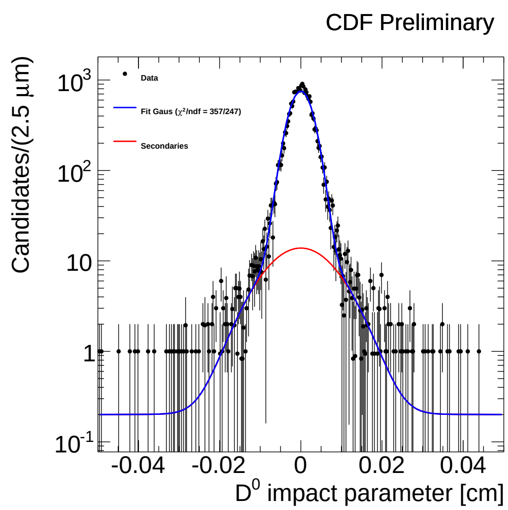

(d)

Figure 56: Impact parameter distributions of (a) $D^{*-} \to \overline{D}^0(\to \pi^+\pi^-)\pi_s^-$, (b) $D^{*+} \to D^0(\to \pi^+\pi^-)\pi_s^+$, (c) $D^{*-} \to \overline{D}^0(\to K^+K^-)\pi_s^-$ and (d) $D^{*+} \to D^0(\to K^+K^-)\pi_s^+$ candidates restricted in the decay-time bin 11, with fit projections overlaid.

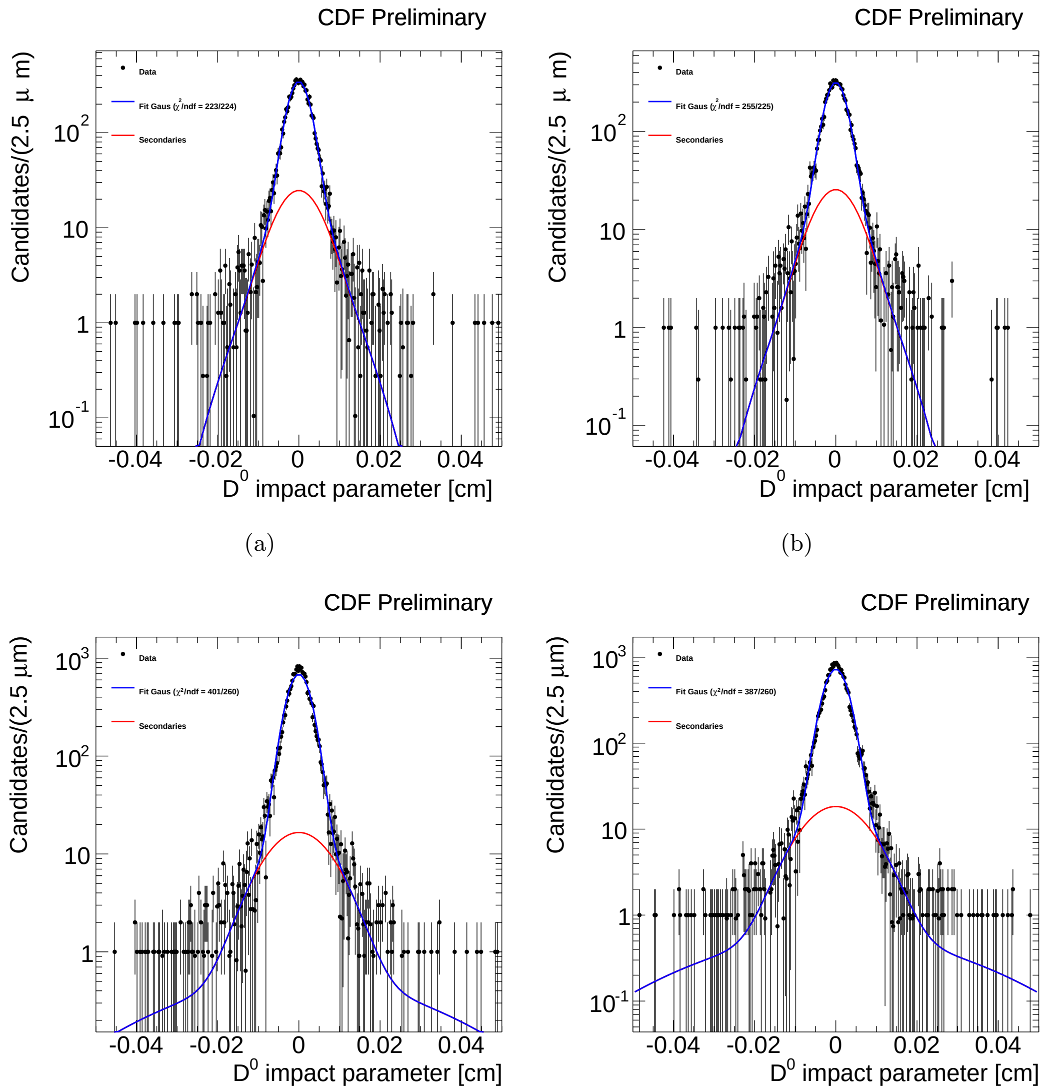

(a) (b) (c) (d)

Figure 57: Impact parameter distributions of (a) $D^{*-} \to \overline{D}^0(\to \pi^+\pi^-)\pi_s^-$, (b) $D^{*+} \to D^0(\to \pi^+\pi^-)\pi_s^+$, (c) $D^{*-} \to \overline{D}^0(\to K^+K^-)\pi_s^-$ and (d) $D^{*+} \to D^0(\to K^+K^-)\pi_s^+$ candidates restricted in the decay-time bin 12, with fit projections overlaid.

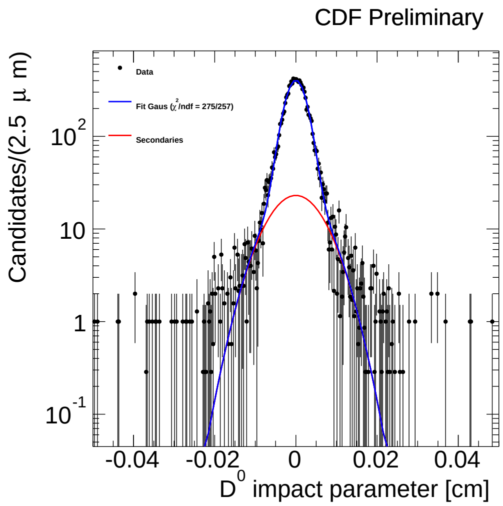

(a)

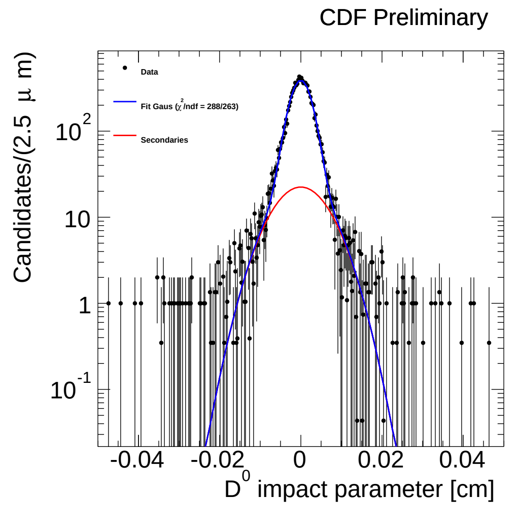

(b)

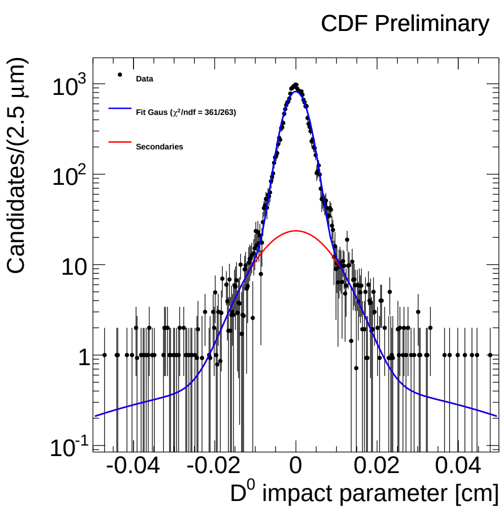

(c)

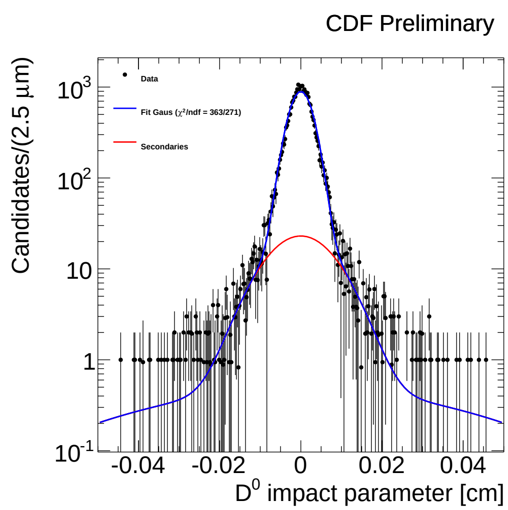

(d)

Figure 58: Impact parameter distributions of (a) $D^{*-} \rightarrow \overline{D}^0(\rightarrow \pi^+\pi^-)\pi_s^-$, (b) $D^{*+} \rightarrow D^0(\rightarrow \pi^+\pi^-)\pi_s^+$, (c) $D^{*-} \rightarrow \overline{D}^0(\rightarrow K^+K^-)\pi_s^-$ and (d) $D^{*+} \rightarrow D^0(\rightarrow K^+K^-)\pi_s^+$ candidates restricted in the decay-time bin 13, with fit projections overlaid.

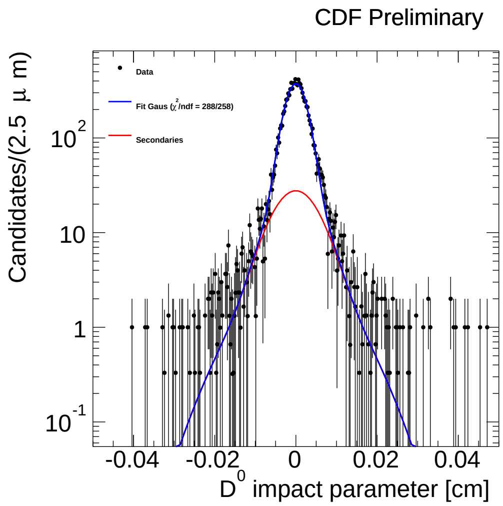

(a)

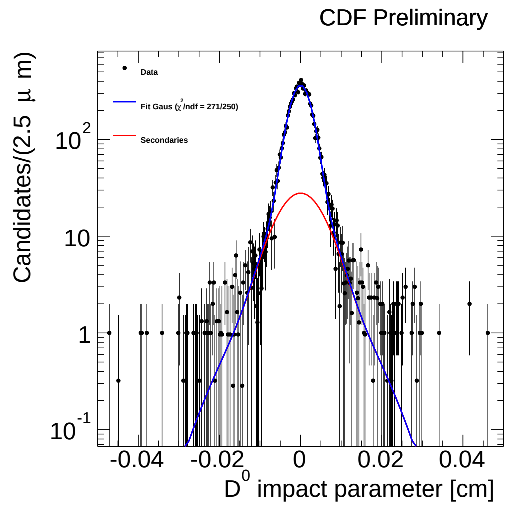

(b)

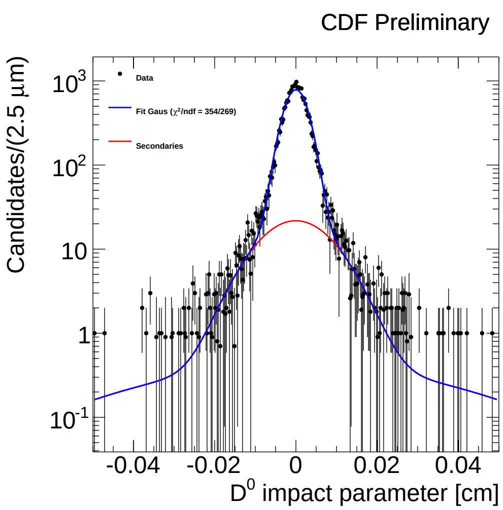

(c)

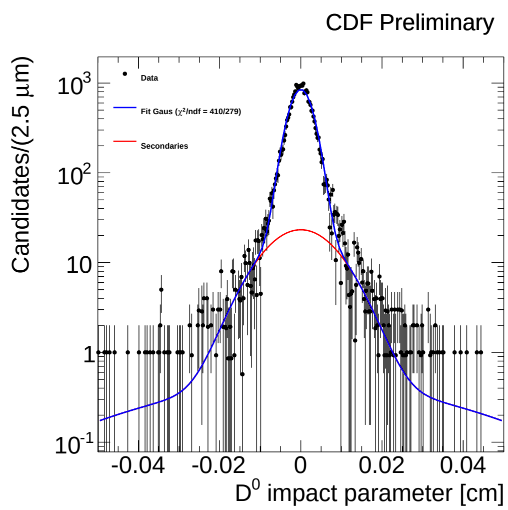

(d)

Figure 59: Impact parameter distributions of (a) $D^{*-} \to \overline{D}^0(\to \pi^+\pi^-)\pi_s^-$, (b) $D^{*+} \to D^0(\to \pi^+\pi^-)\pi_s^+$, (c) $D^{*-} \to \overline{D}^0(\to K^+K^-)\pi_s^-$ and (d) $D^{*+} \to D^0(\to K^+K^-)\pi_s^+$ candidates restricted in the decay-time bin 14, with fit projections overlaid.

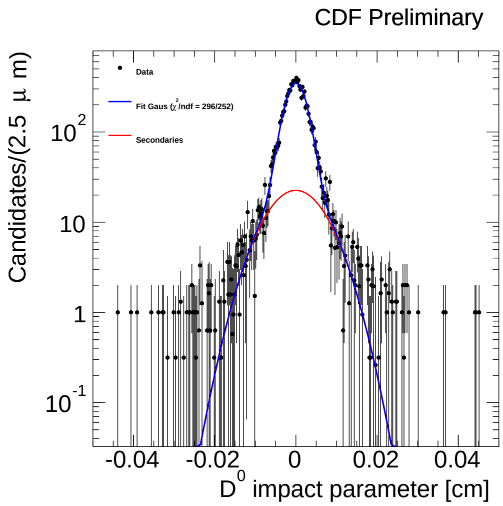

(a)

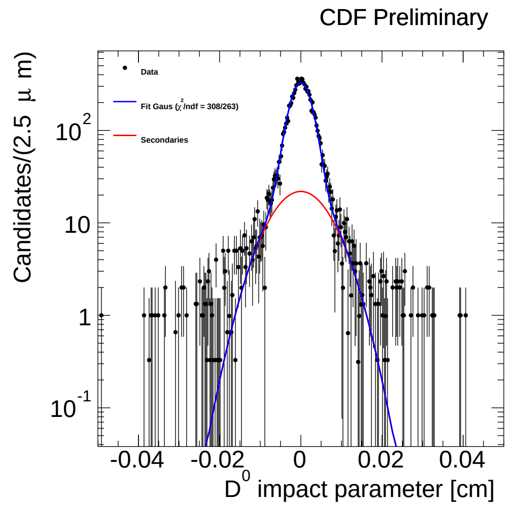

(b)

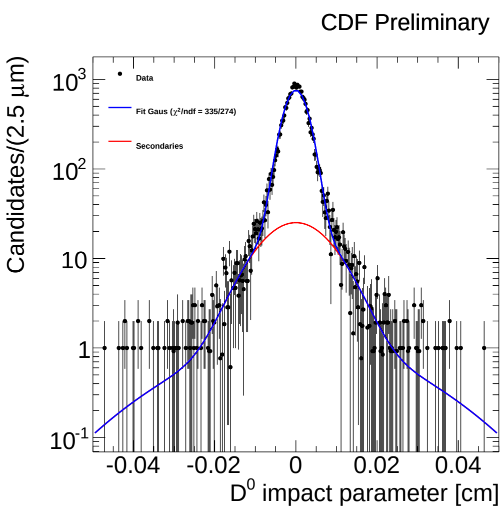

(c)

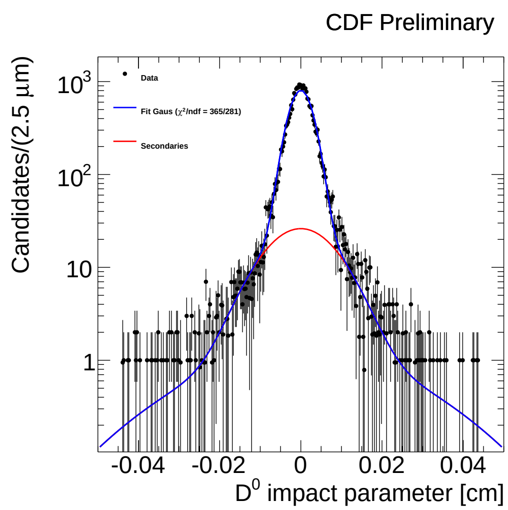

(d)

Figure 60: Impact parameter distributions of (a) $D^{*-} \to \overline{D}^0(\to \pi^+\pi^-)\pi_s^-$, (b) $D^{*+} \to D^0(\to \pi^+\pi^-)\pi_s^+$, (c) $D^{*-} \to \overline{D}^0(\to K^+K^-)\pi_s^-$ and (d) $D^{*+} \to D^0(\to K^+K^-)\pi_s^+$ candidates restricted in the decay-time bin 15, with fit projections overlaid.

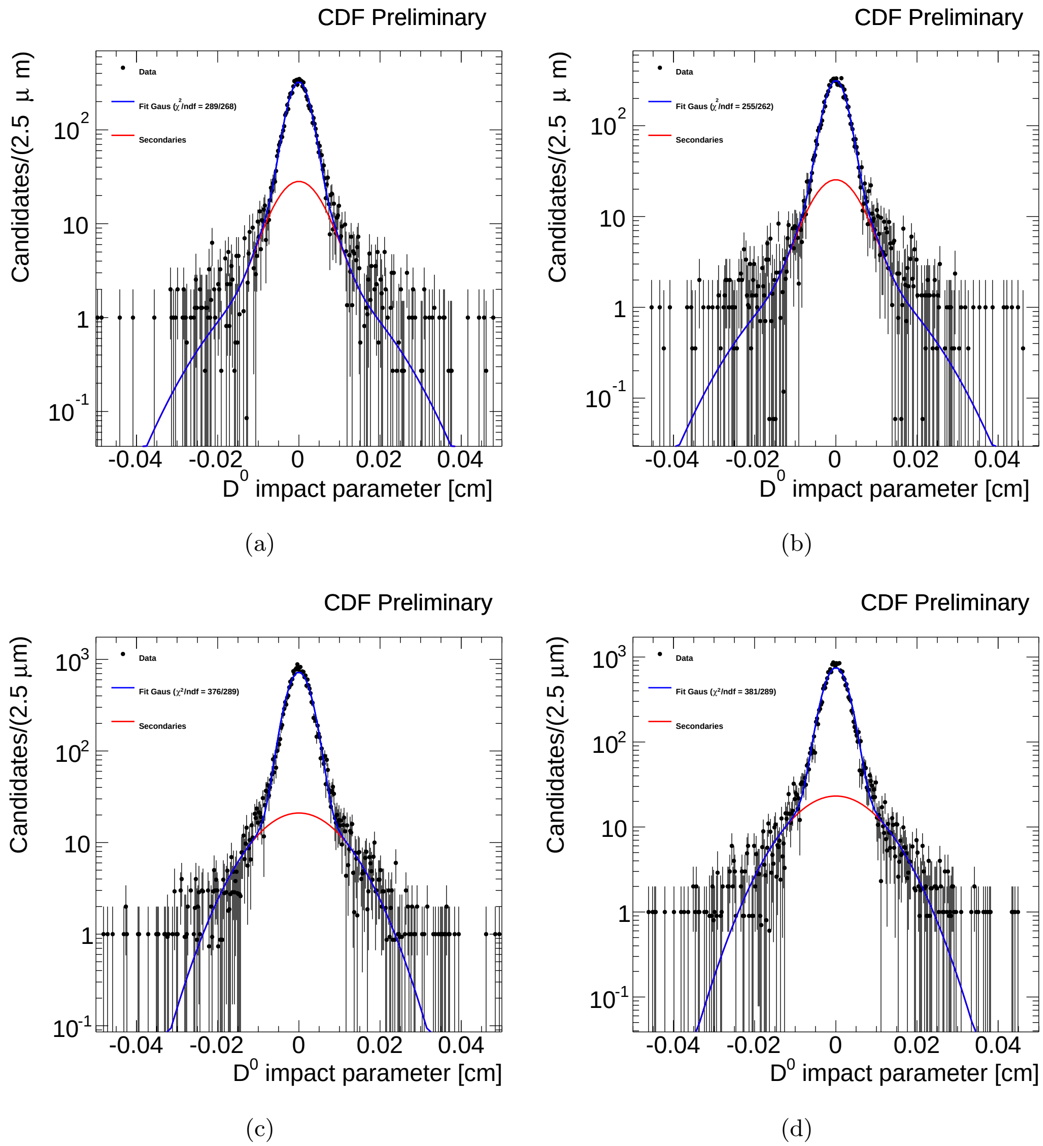

Figure 61: Impact parameter distributions of (a) $D^{*-} \to \overline{D}^0(\to \pi^+\pi^-)\pi_s^-$, (b) $D^{*+} \to D^0(\to \pi^+\pi^-)\pi_s^+$, (c) $D^{*-} \to \overline{D}^0(\to K^+K^-)\pi_s^-$ and (d) $D^{*+} \to D^0(\to K^+K^-)\pi_s^+$ candidates restricted in the decay-time bin 16, with fit projections overlaid.

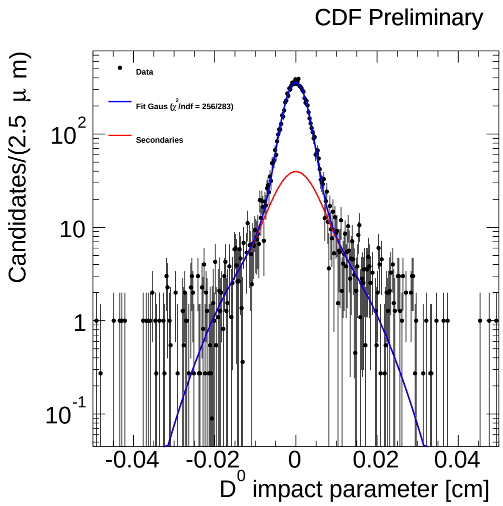

(a)

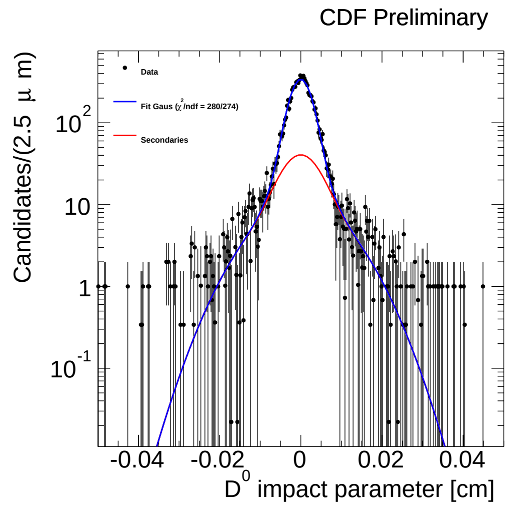

(b)

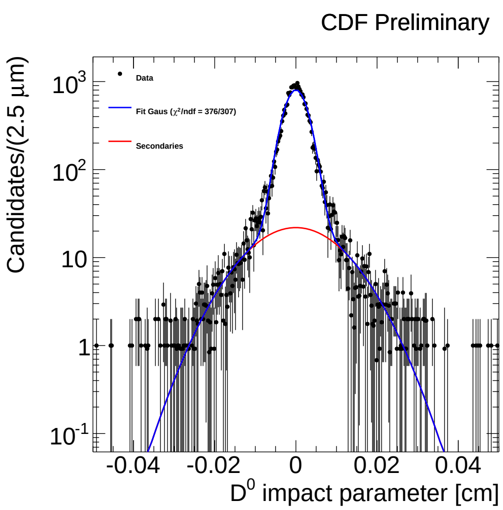

(c)

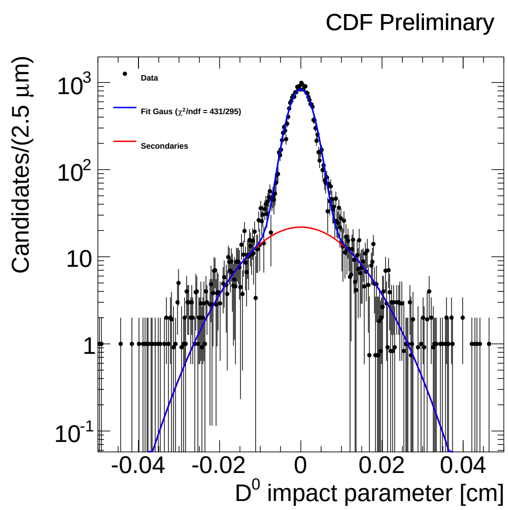

(d)

Figure 62: Impact parameter distributions of (a) $D^{*-} \to \overline{D}^0(\to \pi^+\pi^-)\pi_s^-$, (b) $D^{*+} \to D^0(\to \pi^+\pi^-)\pi_s^+$, (c) $D^{*-} \to \overline{D}^0(\to K^+K^-)\pi_s^-$ and (d) $D^{*+} \to D^0(\to K^+K^-)\pi_s^+$ candidates restricted in the decay-time bin 17, with fit projections overlaid.

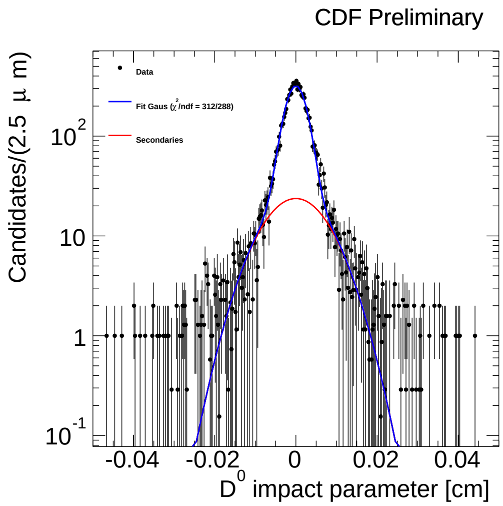

(a)

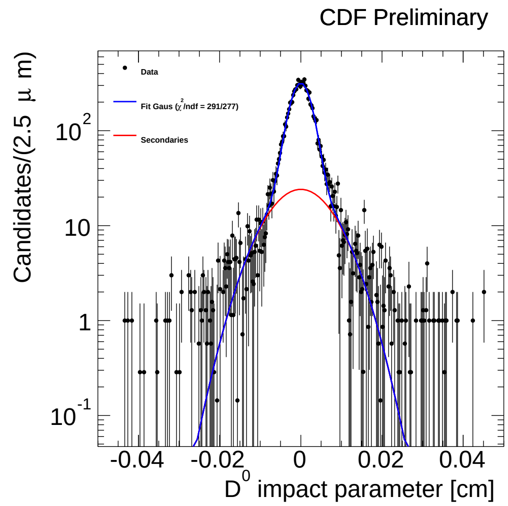

(b)

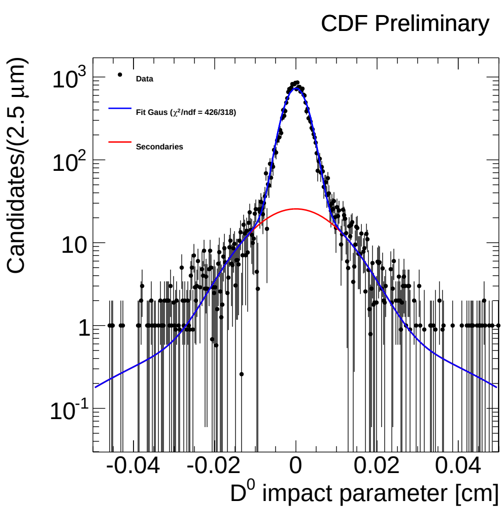

(c)

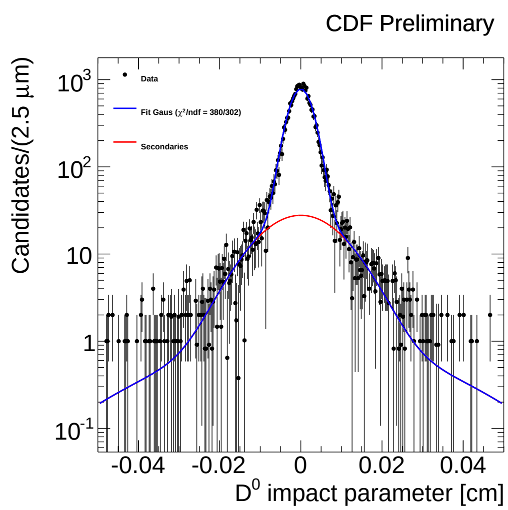

(d)

Figure 63: Impact parameter distributions of (a) $D^{*-} \rightarrow \overline{D}^0(\rightarrow \pi^+\pi^-)\pi_s^-$, (b) $D^{*+} \rightarrow D^0(\rightarrow \pi^+\pi^-)\pi_s^+$, (c) $D^{*-} \rightarrow \overline{D}^0(\rightarrow K^+K^-)\pi_s^-$ and (d) $D^{*+} \rightarrow D^0(\rightarrow K^+K^-)\pi_s^+$ candidates restricted in the decay-time bin 18, with fit projections overlaid.

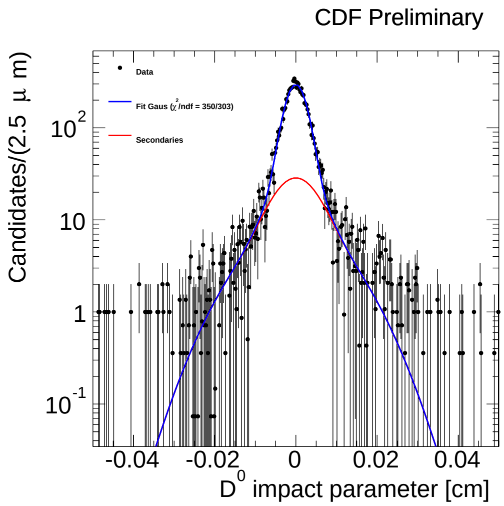

(a)

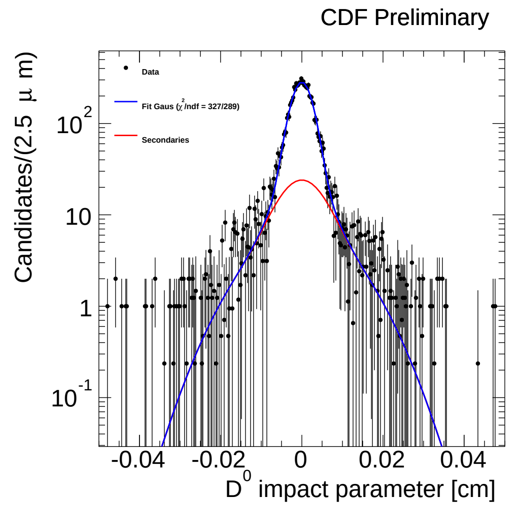

(b)

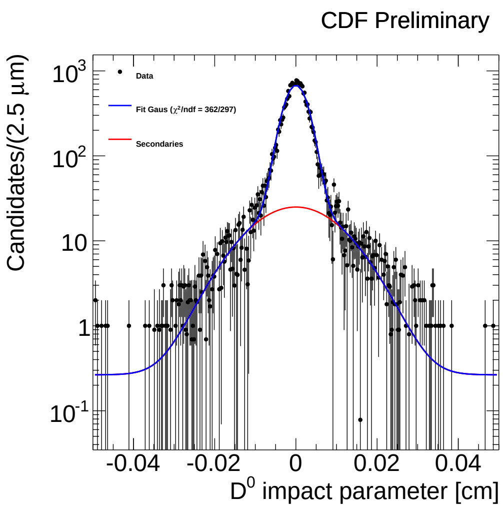

(c)

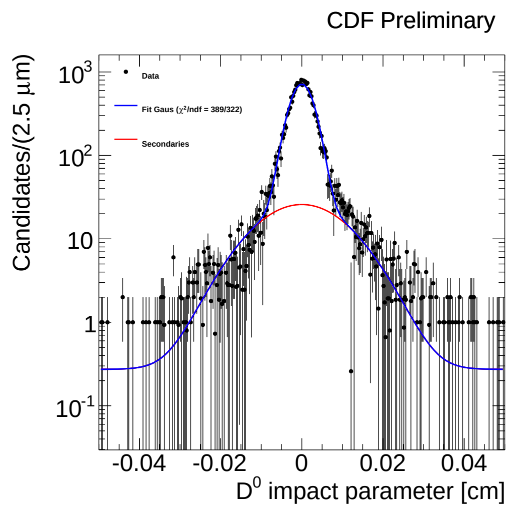

(d)

Figure 64: Impact parameter distributions of (a) $D^{*-} \to \overline{D}^0(\to \pi^+\pi^-)\pi_s^-$, (b) $D^{*+} \to D^0(\to \pi^+\pi^-)\pi_s^+$, (c) $D^{*-} \to \overline{D}^0(\to K^+K^-)\pi_s^-$ and (d) $D^{*+} \to D^0(\to K^+K^-)\pi_s^+$ candidates restricted in the decay-time bin 19, with fit projections overlaid.

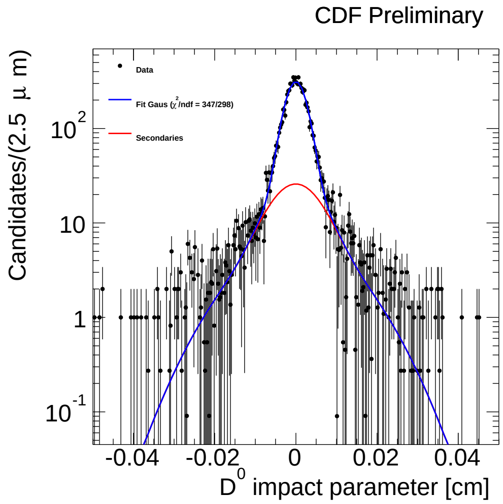

(a)

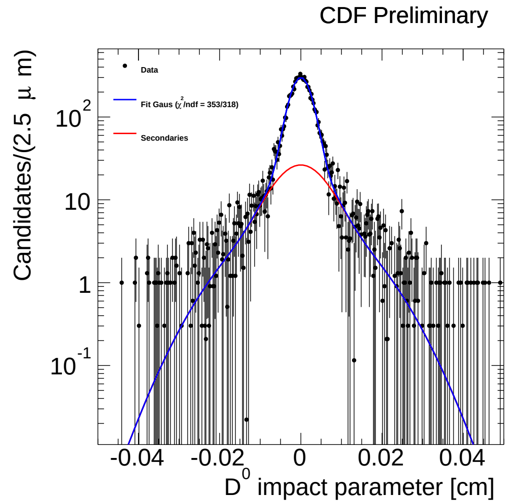

(b)

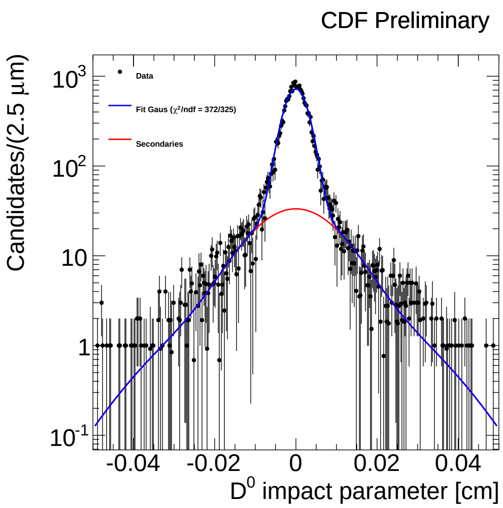

(c)

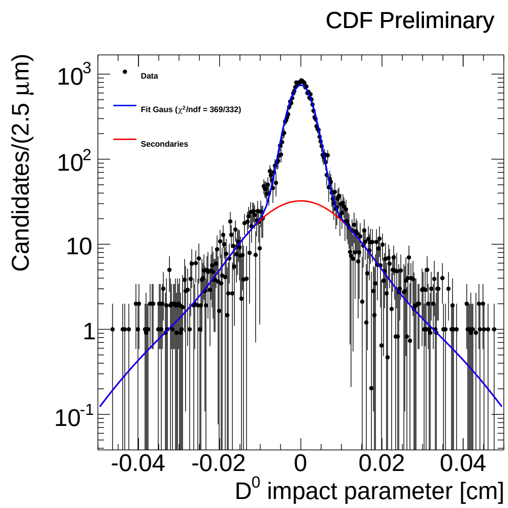

(d)

Figure 65: Impact parameter distributions of (a) $D^{*-} \to \overline{D}^0(\to \pi^+\pi^-)\pi_s^-$, (b) $D^{*+} \to D^0(\to \pi^+\pi^-)\pi_s^+$, (c) $D^{*-} \to \overline{D}^0(\to K^+K^-)\pi_s^-$ and (d) $D^{*+} \to D^0(\to K^+K^-)\pi_s^+$ candidates restricted in the decay-time bin 20, with fit projections overlaid.

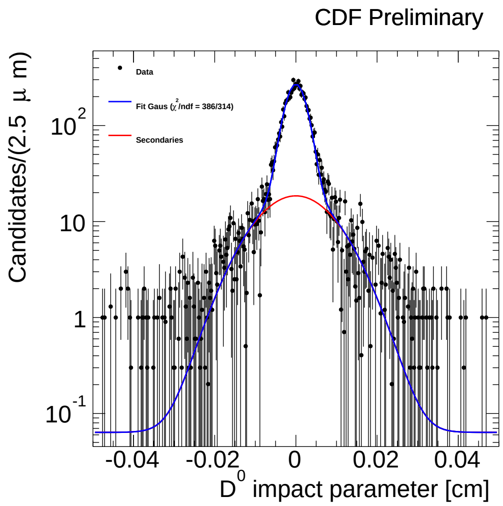

(a)

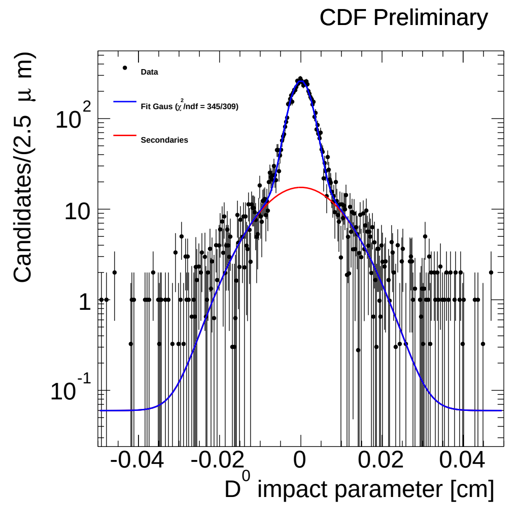

(b)

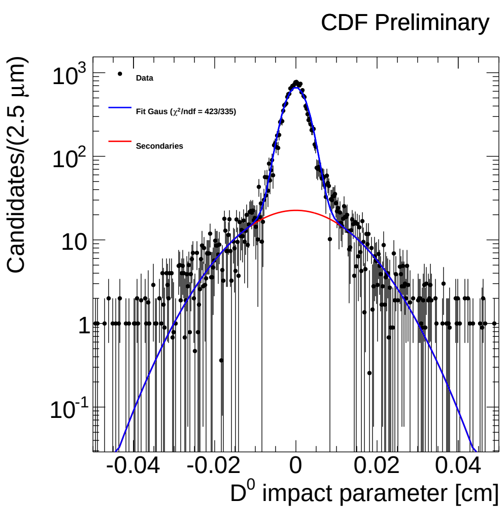

(c)

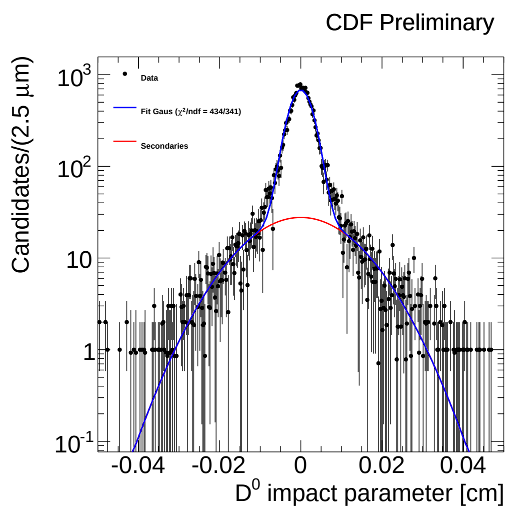

(d)

Figure 66: Impact parameter distributions of (a) $D^{*-} \rightarrow \overline{D}^0(\rightarrow \pi^+\pi^-)\pi_s^-$, (b) $D^{*+} \rightarrow D^0(\rightarrow \pi^+\pi^-)\pi_s^+$, (c) $D^{*-} \rightarrow \overline{D}^0(\rightarrow K^+K^-)\pi_s^-$ and (d) $D^{*+} \rightarrow D^0(\rightarrow K^+K^-)\pi_s^+$ candidates restricted in the decay-time bin 21, with fit projections overlaid.

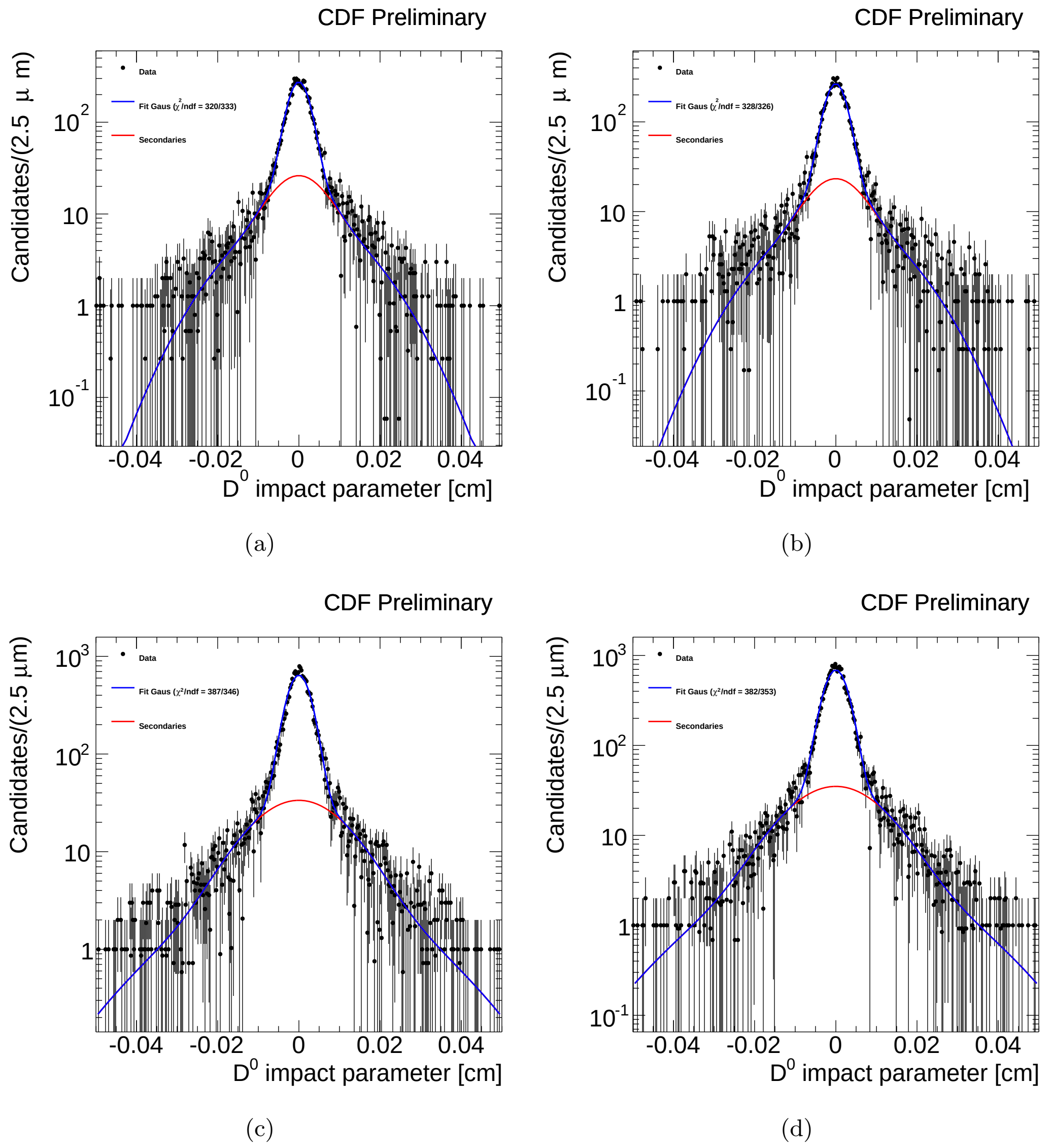

Figure 67: Impact parameter distributions of (a) $D^{*-} \to \overline{D}^0(\to \pi^+\pi^-)\pi_s^-$, (b) $D^{*+} \to D^0(\to \pi^+\pi^-)\pi_s^+$, (c) $D^{*-} \to \overline{D}^0(\to K^+K^-)\pi_s^-$ and (d) $D^{*+} \to D^0(\to K^+K^-)\pi_s^+$ candidates restricted in the decay-time bin 22, with fit projections overlaid.

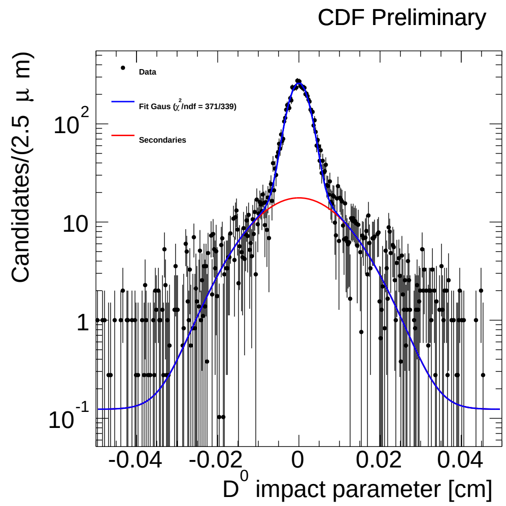

(a)

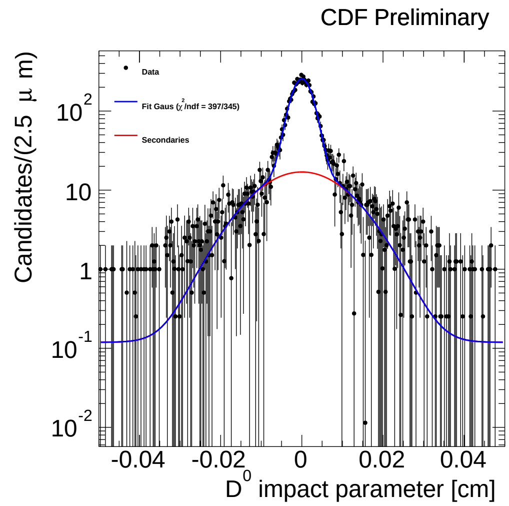

(b)

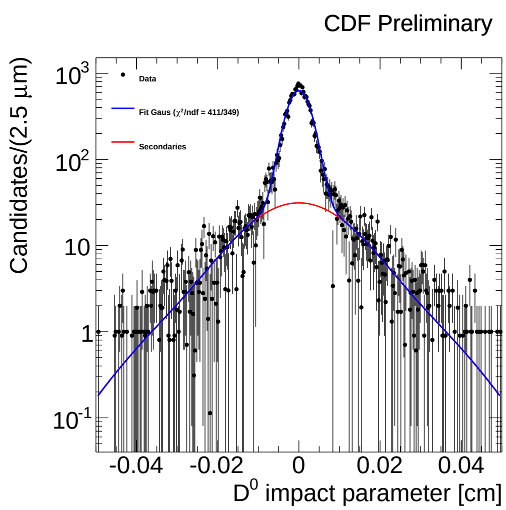

(c)

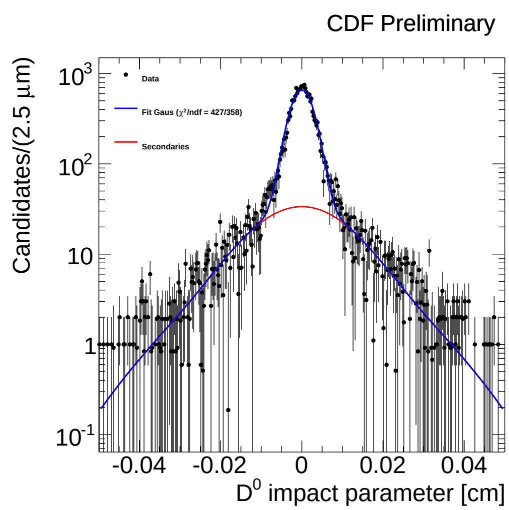

(d)

Figure 68: Impact parameter distributions of (a) $D^{*-} \to \overline{D}^0(\to \pi^+\pi^-)\pi_s^-$, (b) $D^{*+} \to D^0(\to \pi^+\pi^-)\pi_s^+$, (c) $D^{*-} \to \overline{D}^0(\to K^+K^-)\pi_s^-$ and (d) $D^{*+} \to D^0(\to K^+K^-)\pi_s^+$ candidates restricted in the decay-time bin 23, with fit projections overlaid.

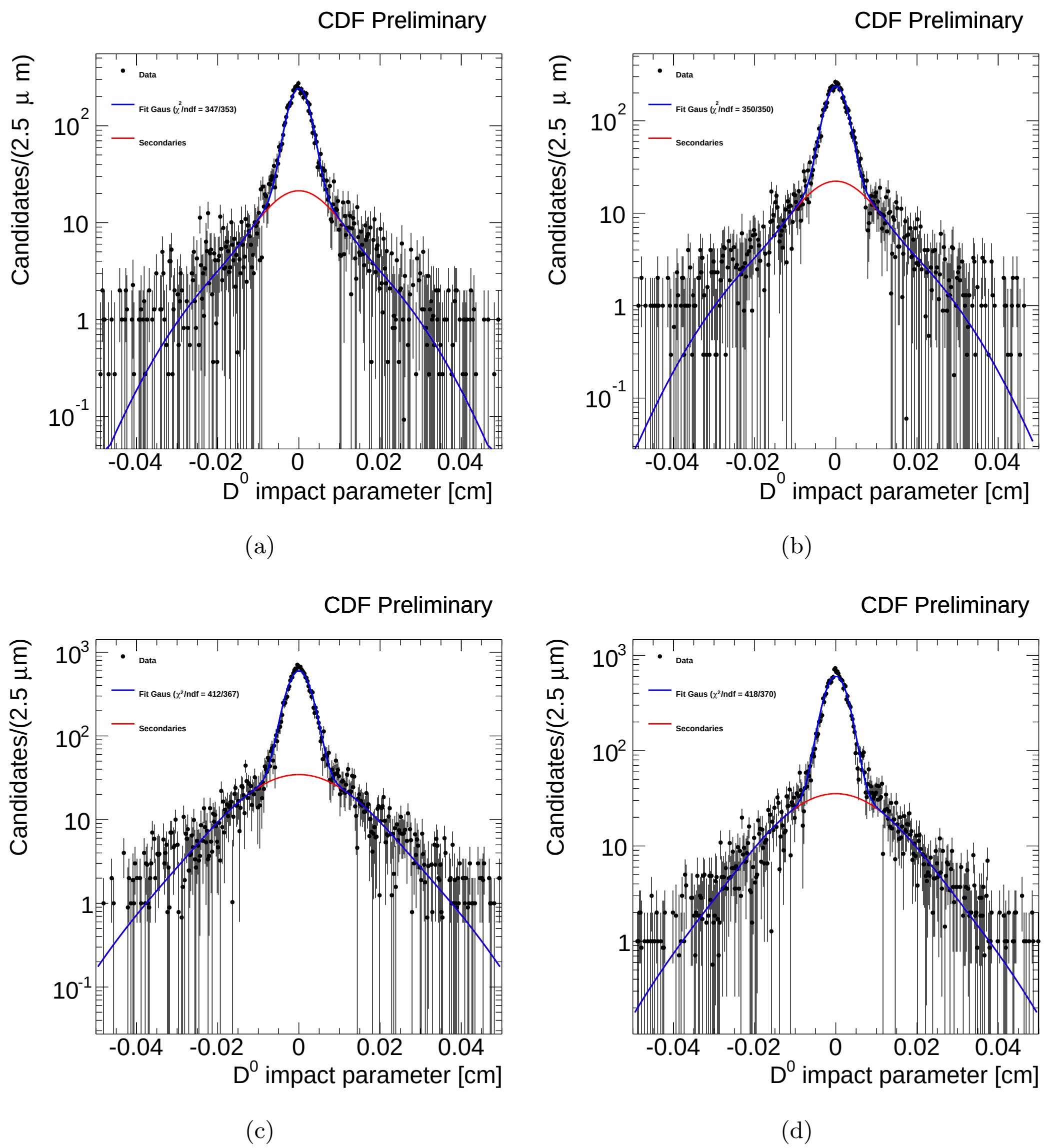

Figure 69: Impact parameter distributions of (a) $D^{*-} \to \overline{D}^0(\to \pi^+\pi^-)\pi_s^-$, (b) $D^{*+} \to D^0(\to \pi^+\pi^-)\pi_s^+$, (c) $D^{*-} \to \overline{D}^0(\to K^+K^-)\pi_s^-$ and (d) $D^{*+} \to D^0(\to K^+K^-)\pi_s^+$ candidates restricted in the decay-time bin 24, with fit projections overlaid.

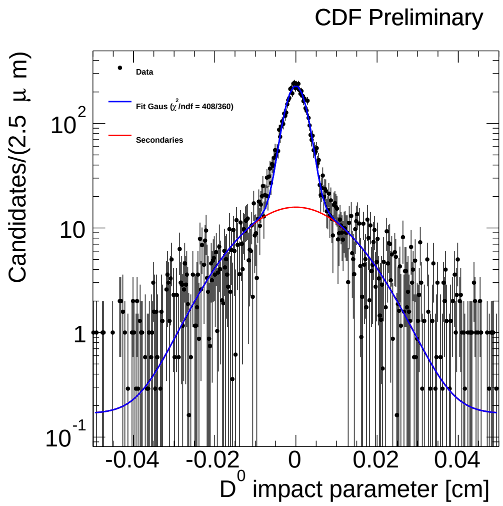

(a)

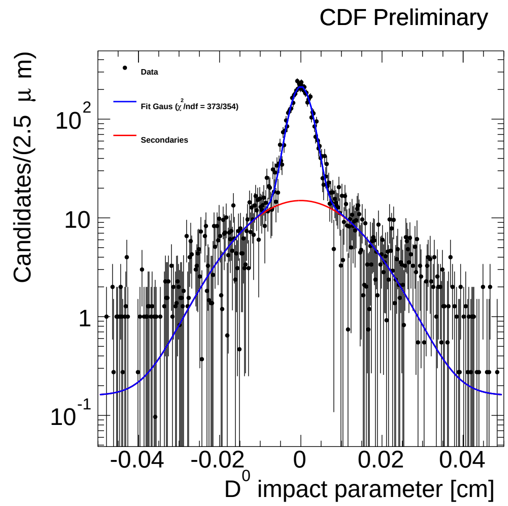

(b)

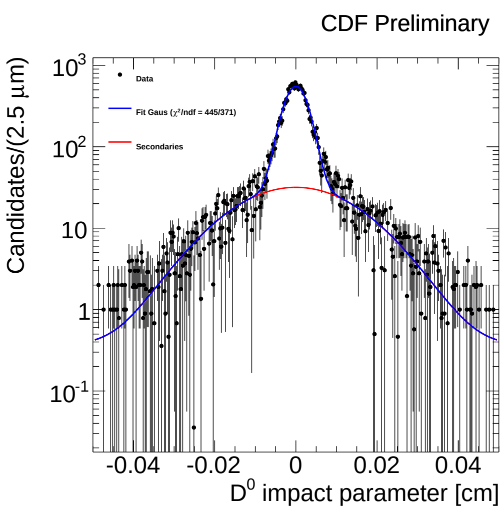

(c)

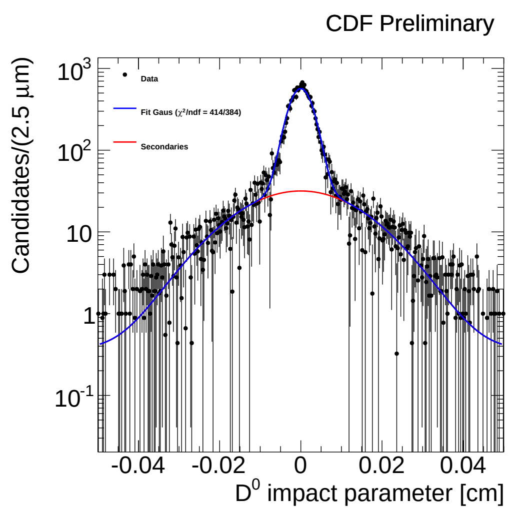

(d)

Figure 70: Impact parameter distributions of (a) $D^{*-} \to \overline{D}^0(\to \pi^+\pi^-)\pi_s^-$, (b) $D^{*+} \to D^0(\to \pi^+\pi^-)\pi_s^+$, (c) $D^{*-} \to \overline{D}^0(\to K^+K^-)\pi_s^-$ and (d) $D^{*+} \to D^0(\to K^+K^-)\pi_s^+$ candidates restricted in the decay-time bin 25, with fit projections overlaid.

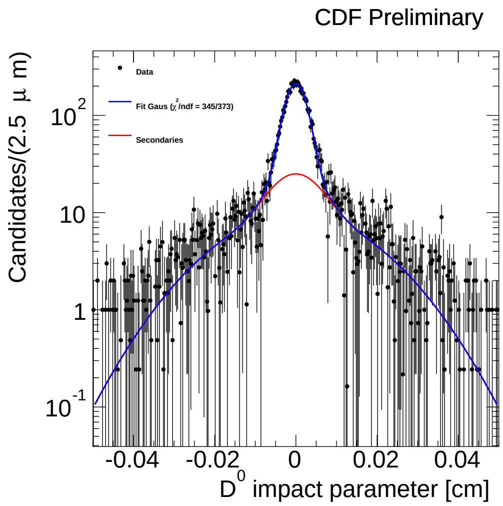

(a)

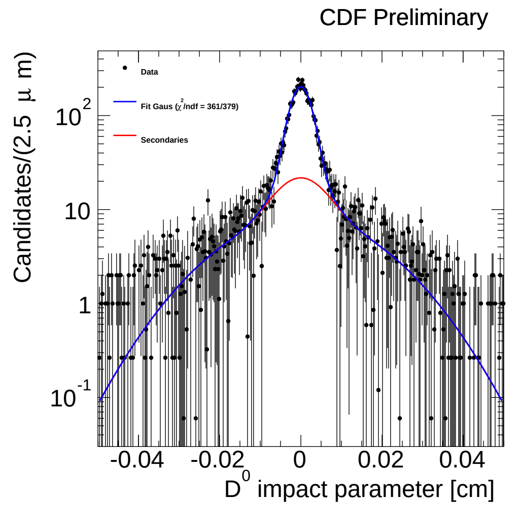

(b)

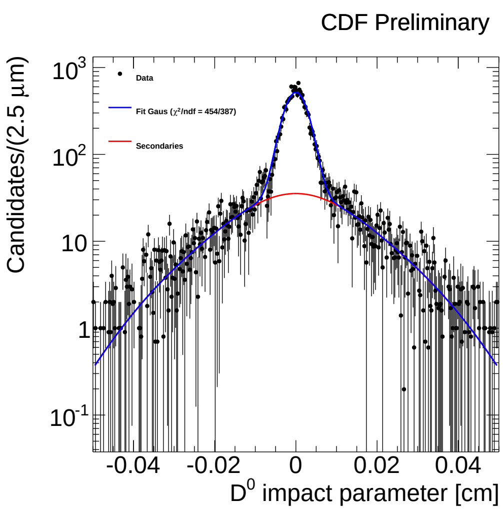

(c)

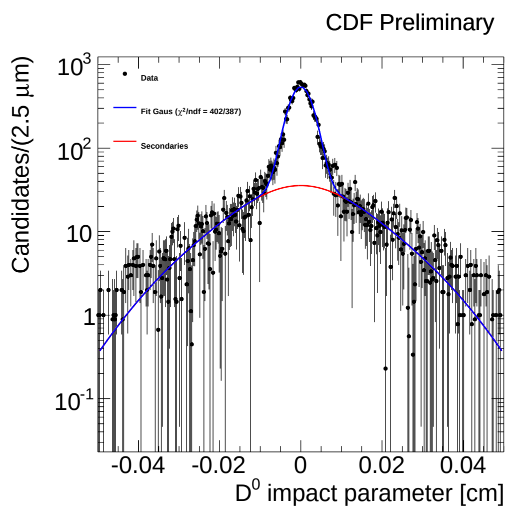

(d)

Figure 71: Impact parameter distributions of (a) $D^{*-} \to \overline{D}^0(\to \pi^+\pi^-)\pi_s^-$, (b) $D^{*+} \to D^0(\to \pi^+\pi^-)\pi_s^+$, (c) $D^{*-} \to \overline{D}^0(\to K^+K^-)\pi_s^-$ and (d) $D^{*+} \to D^0(\to K^+K^-)\pi_s^+$ candidates restricted in the decay-time bin 26, with fit projections overlaid.

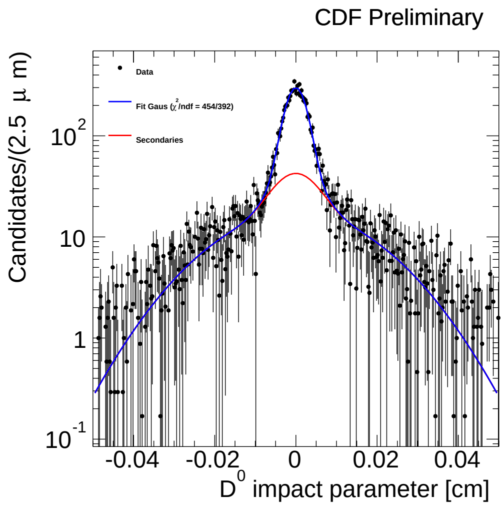

(a)

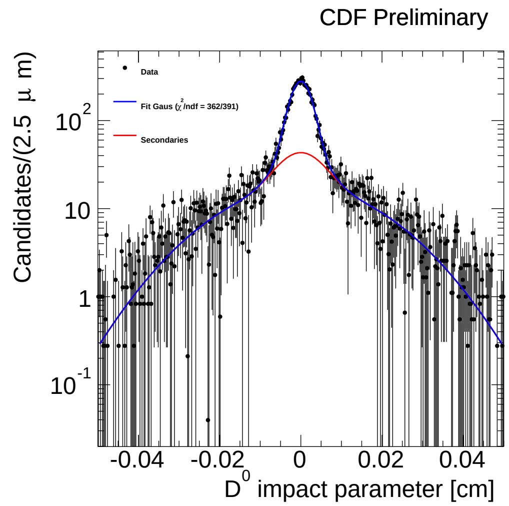

(b)

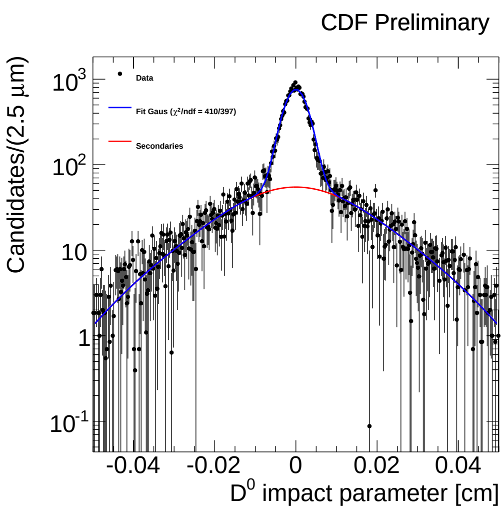

(c)

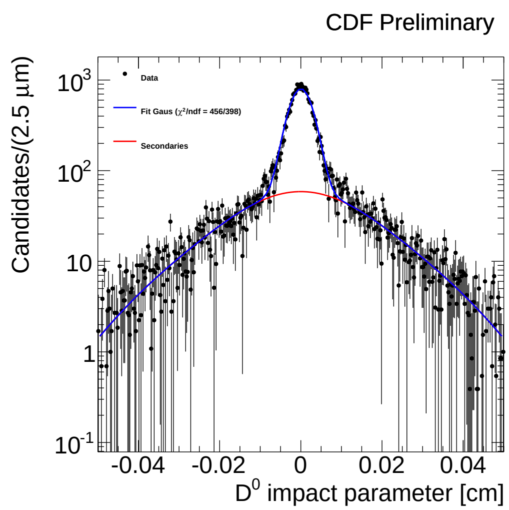

(d)

Figure 72: Impact parameter distributions of (a) $D^{*-} \to \overline{D}^0(\to \pi^+\pi^-)\pi_s^-$, (b) $D^{*+} \to D^0(\to \pi^+\pi^-)\pi_s^+$, (c) $D^{*-} \to \overline{D}^0(\to K^+K^-)\pi_s^-$ and (d) $D^{*+} \to D^0(\to K^+K^-)\pi_s^+$ candidates restricted in the decay-time bin 27, with fit projections overlaid.

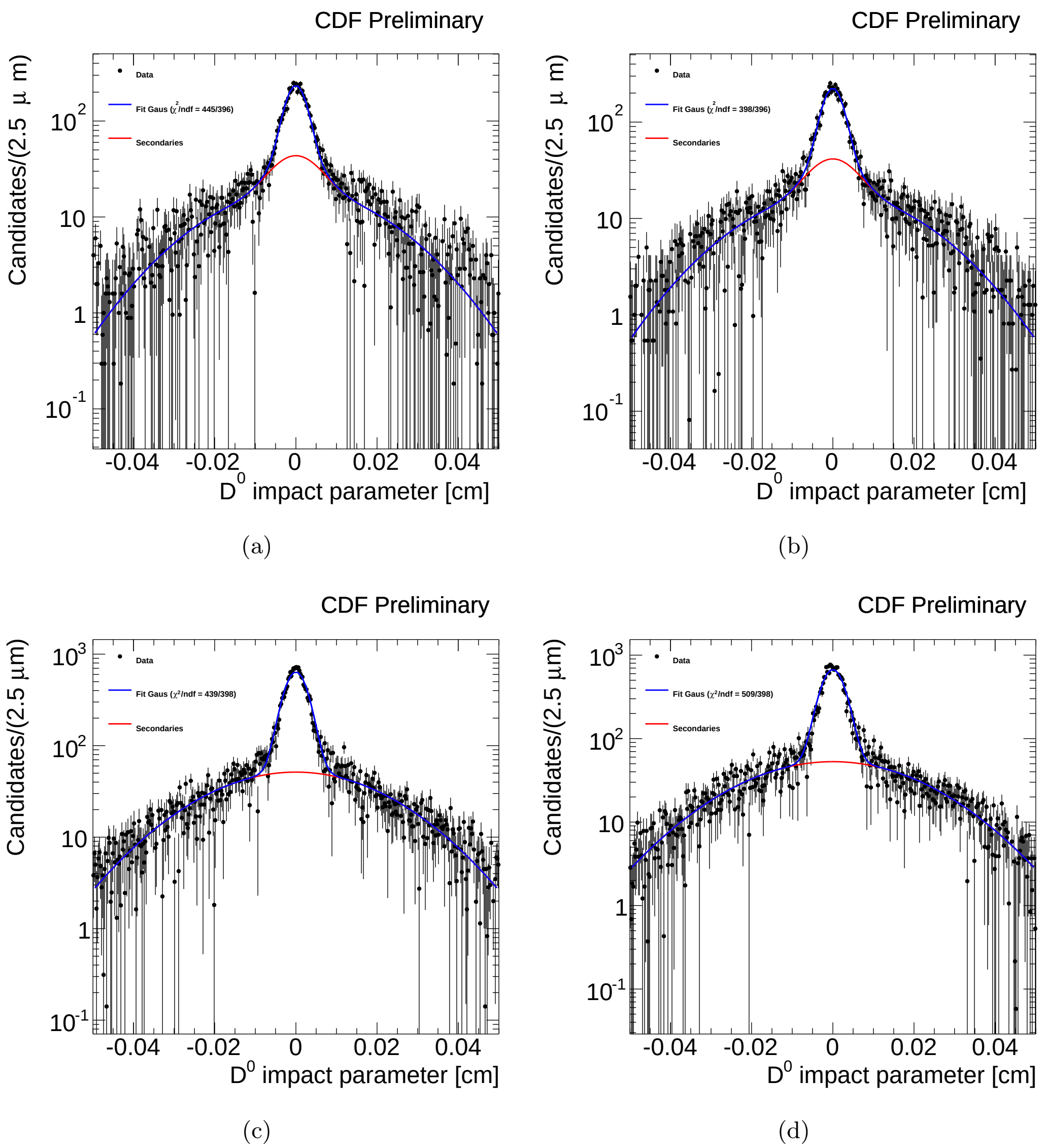

Figure 73: Impact parameter distributions of (a) $D^{*-} \to \overline{D}^0(\to \pi^+\pi^-)\pi_s^-$, (b) $D^{*+} \to D^0(\to \pi^+\pi^-)\pi_s^+$, (c) $D^{*-} \to \overline{D}^0(\to K^+K^-)\pi_s^-$ and (d) $D^{*+} \to D^0(\to K^+K^-)\pi_s^+$ candidates restricted in the decay-time bin 28, with fit projections overlaid.

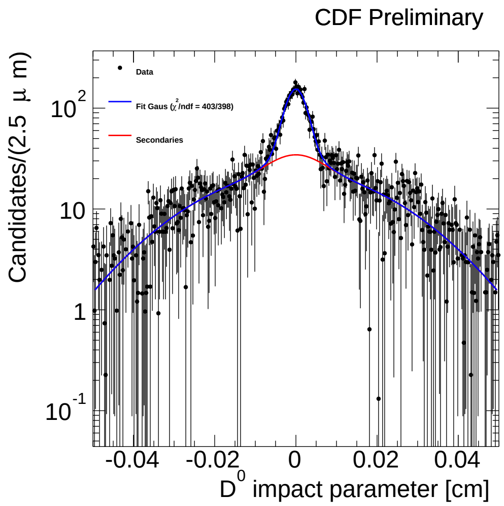

(a)

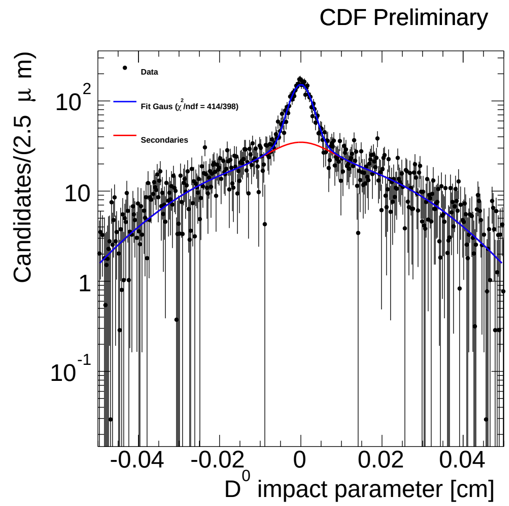

(b)

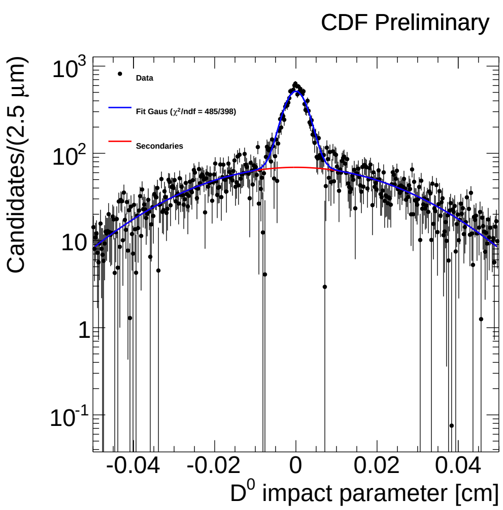

(c)

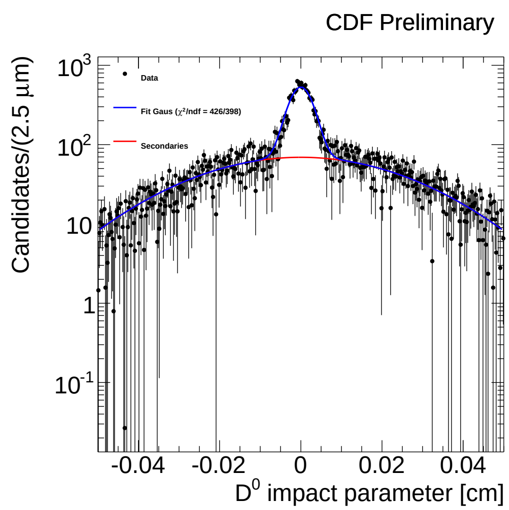

(d)

Figure 74: Impact parameter distributions of (a) $D^{*-} \to \overline{D}^0(\to \pi^+\pi^-)\pi_s^-$, (b) $D^{*+} \to D^0(\to \pi^+\pi^-)\pi_s^+$, (c) $D^{*-} \to \overline{D}^0(\to K^+K^-)\pi_s^-$ and (d) $D^{*+} \to D^0(\to K^+K^-)\pi_s^+$ candidates restricted in the decay-time bin 29, with fit projections overlaid.

C χ^2/ndf summary plots

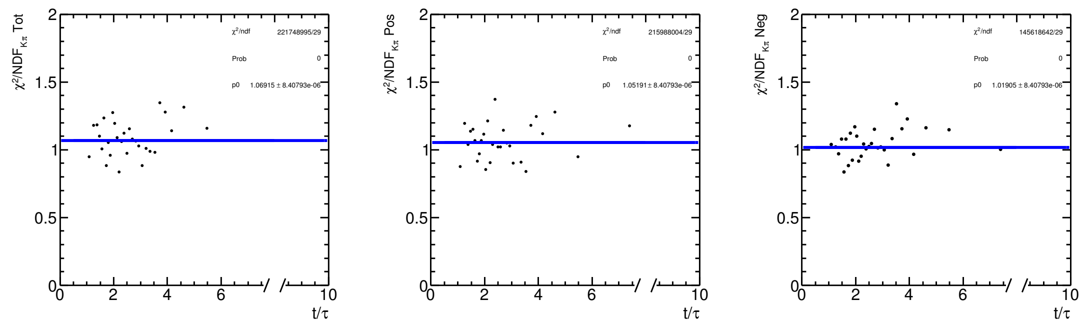

(a)

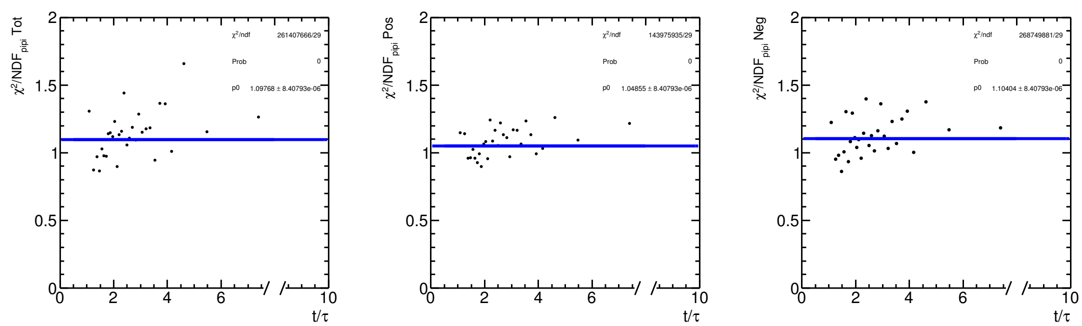

(b)

Figure 75: Mass fits χ^2/ndf distribution for (a,left) $D^* \to \overline{D}^0(\to K^-\pi^+)\pi_s$, (a,middle) $D^{*+} \to D^0(\to K^-\pi^+)\pi_s^+$, (a,right) $D^{*-} \to D^0(\to K^-\pi^+)\pi_s^-$ samples and mass fits χ^2/ndf distribution of (b,left) $D^* \to \overline{D}^0(\to \pi^-\pi^+)\pi_s$, (b,middle) $D^{*+} \to D^0(\to \pi^-\pi^+)\pi_s^+$, (a,right) $D^{*-} \to D^0(\to \pi^-\pi^+)\pi_s^-$ sample

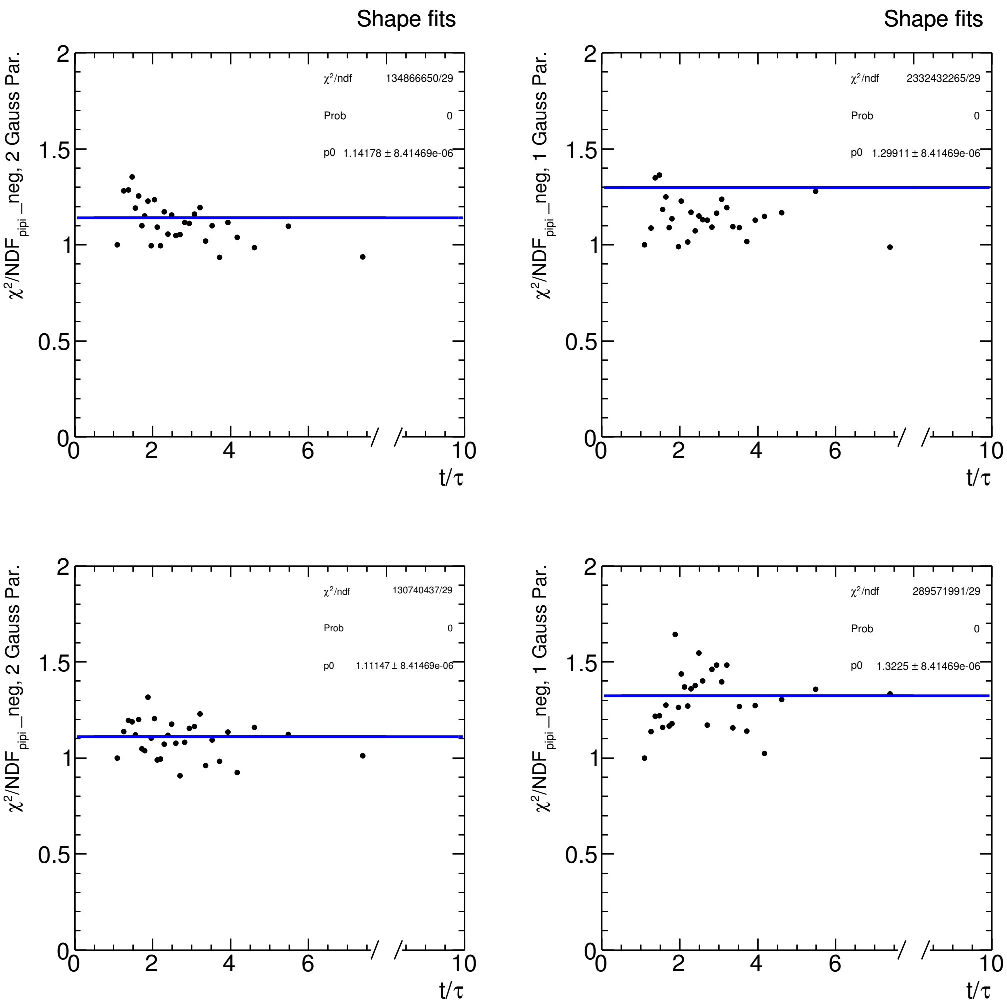

(a)

Figure 76: IP fits χ^2/ndf distribution for (top) $D^* \to \overline{D}^0(\to \pi^-\pi^+)\pi_s$ and (bottom) $D^{*-} \to D^0(\to \pi^-\pi^+)\pi_s^-$ samples. Left column refers to IP fits using default 2 gaussian parametrization, right column to IP fits with single gaussian parametrization with time-dependent width.

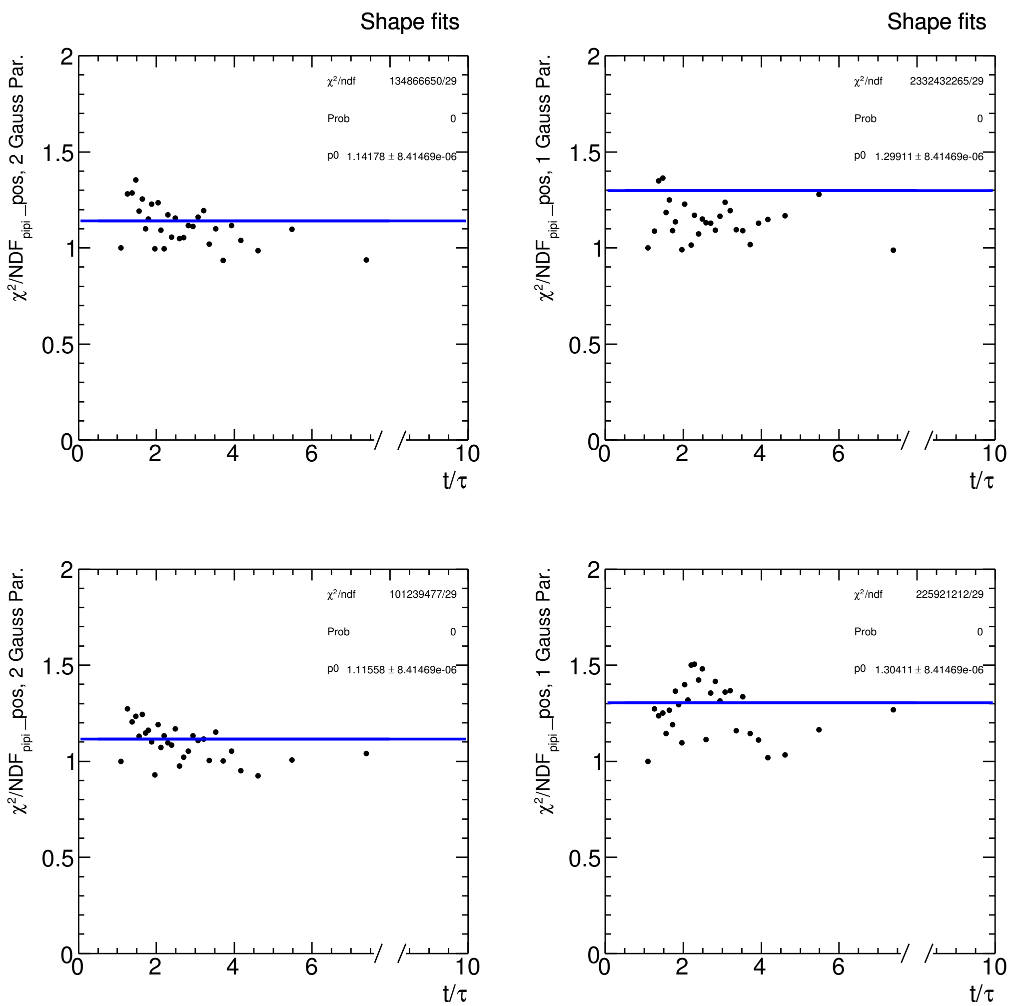

(a)

Figure 77: IP fits χ^2/ndf distribution for (top) $D^* \to \overline{D}^0(\to \pi^-\pi^+)\pi_s$ and (bottom) $D^{*+} \to D^0(\to \pi^-\pi^+)\pi_s^+$ samples. Left column refers to IP fits using gaussian parametrization, right column to IP fits with with single gaussian parametrization with time-dependent width.

D $K\pi$ mass fit projections

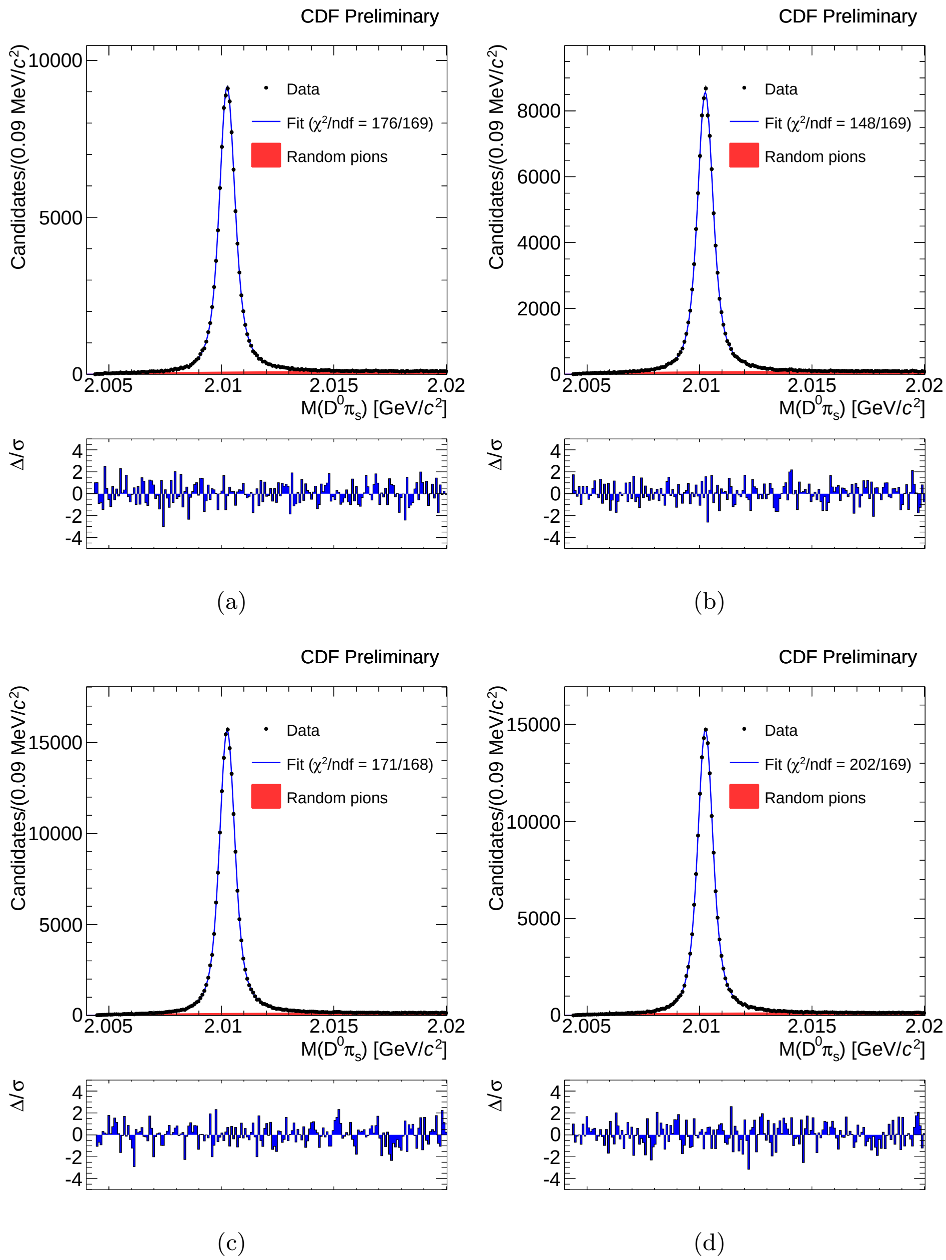

Figure 78: $D^0\pi_s$–mass distributions of (a,c) $D^{*-} \to \overline{D}^0(\to K^-\pi^+)\pi_s^-$ and (b,d) $D^{*+} \to D^0(\to K^-\pi^+)\pi_s^+$ candidates restricted in the decay-time bin (a,b) 0 ($t < 1.18\tau$) and (c,d) 1 ($1.18\tau < t < 1.32\tau$), with fit projections overlaid.

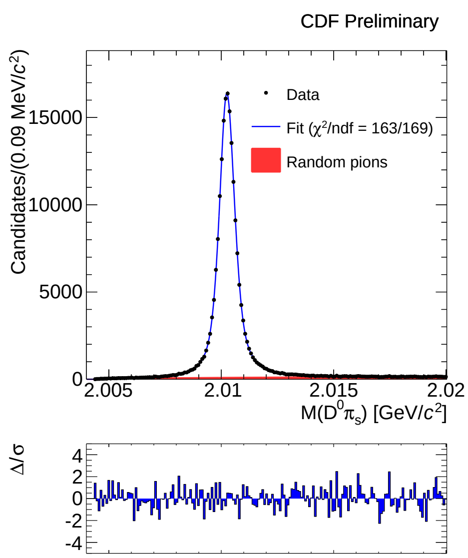

(a)

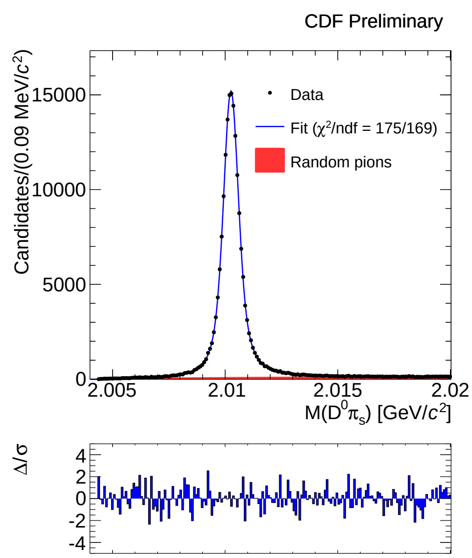

(b)

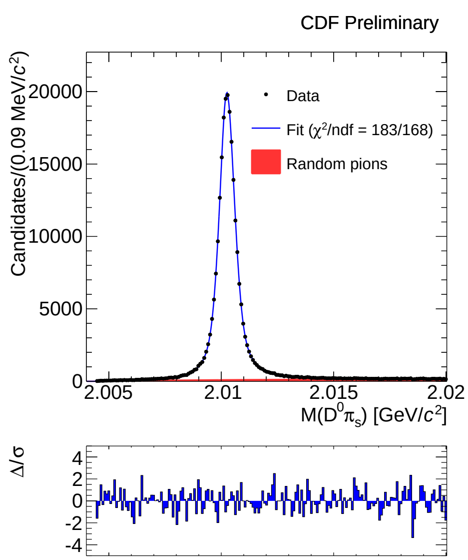

(c)

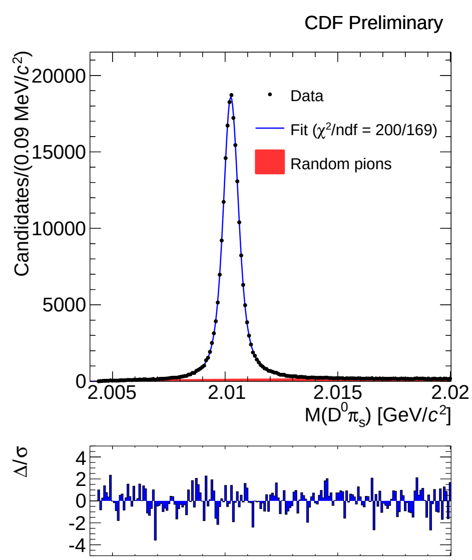

(d)

Figure 79: $D^0\pi_s$–mass distributions of (a,c) $D^{*-} \to \overline{D}^0(\to K^-\pi^+)\pi_s^-$ and (b,d) $D^{*+} \to D^0(\to K^-\pi^+)\pi_s^+$ candidates restricted in the decay-time bin (a,b) 2 ($1.32\tau < t < 1.42\tau$)and (c,d) 3 ($1.42\tau < t < 1.52\tau$), with fit projections overlaid.

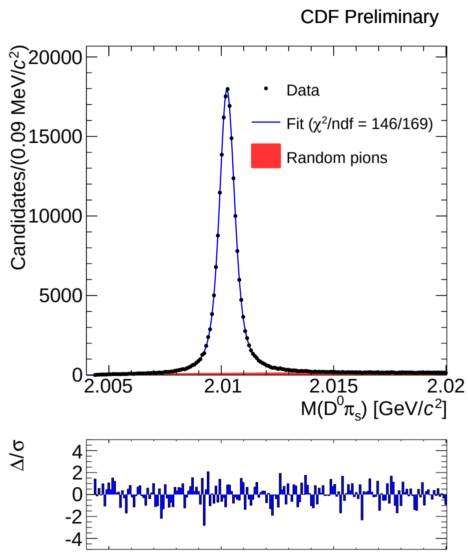

(a)

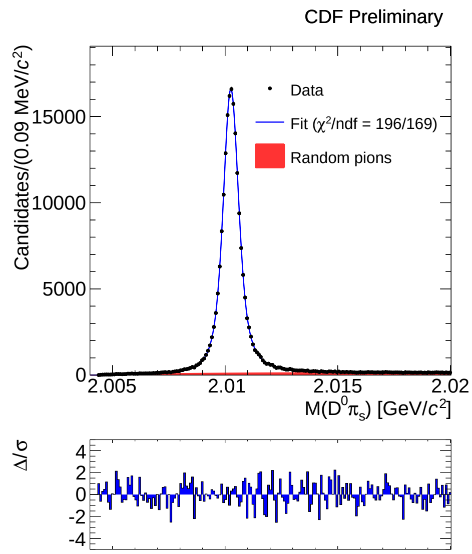

(b)

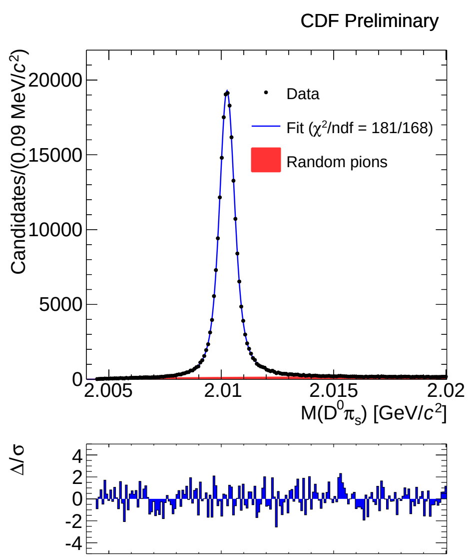

(c)

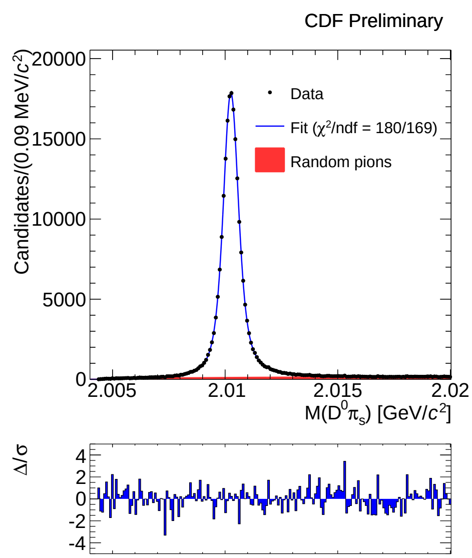

(d)

Figure 80: $D^0\pi_s$–mass distributions of (a,c) $D^{*-} \to \overline{D}^0(\to K^-\pi^+)\pi_s^-$ and (b,d) $D^{*+} \to D^0(\to K^-\pi^+)\pi_s^+$ candidates restricted in the decay-time bin (a,b) 4 ($1.52\tau < t < 1.60\tau$), and (c,d) 5 ($1.60\tau < t < 1.68\tau$), with fit projections overlaid.

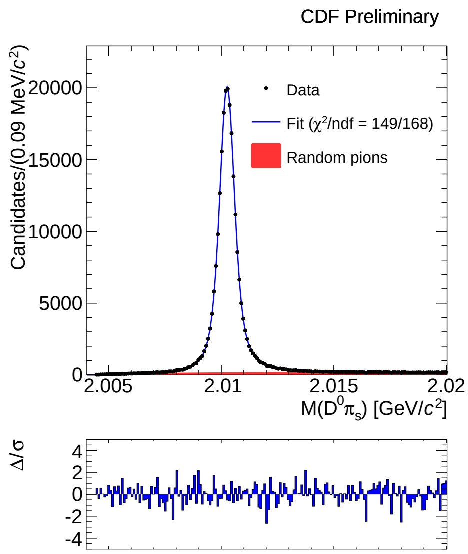

(a)

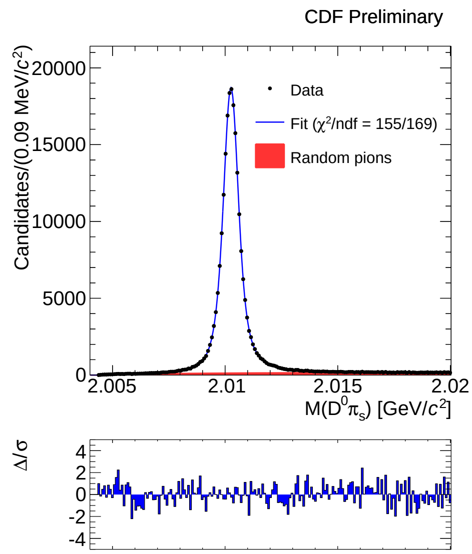

(b)

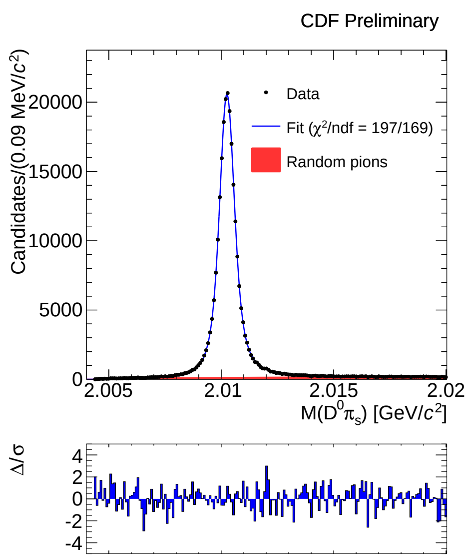

(c)

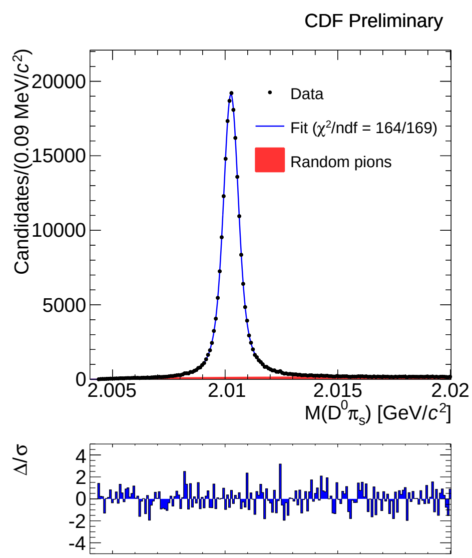

(d)

Figure 81: $D^0\pi_s$–mass distributions of (a,c) $D^{*-} \to \overline{D}^0(\to K^-\pi^+)\pi_s^-$ and (b,d) $D^{*+} \to D^0(\to K^-\pi^+)\pi_s^+$ candidates restricted in the decay-time bin (a,b) 6 ($1.68\tau < t < 1.76\tau$), and (c,d) 7 ($1.76\tau < t < 1.84\tau$), with fit projections overlaid.

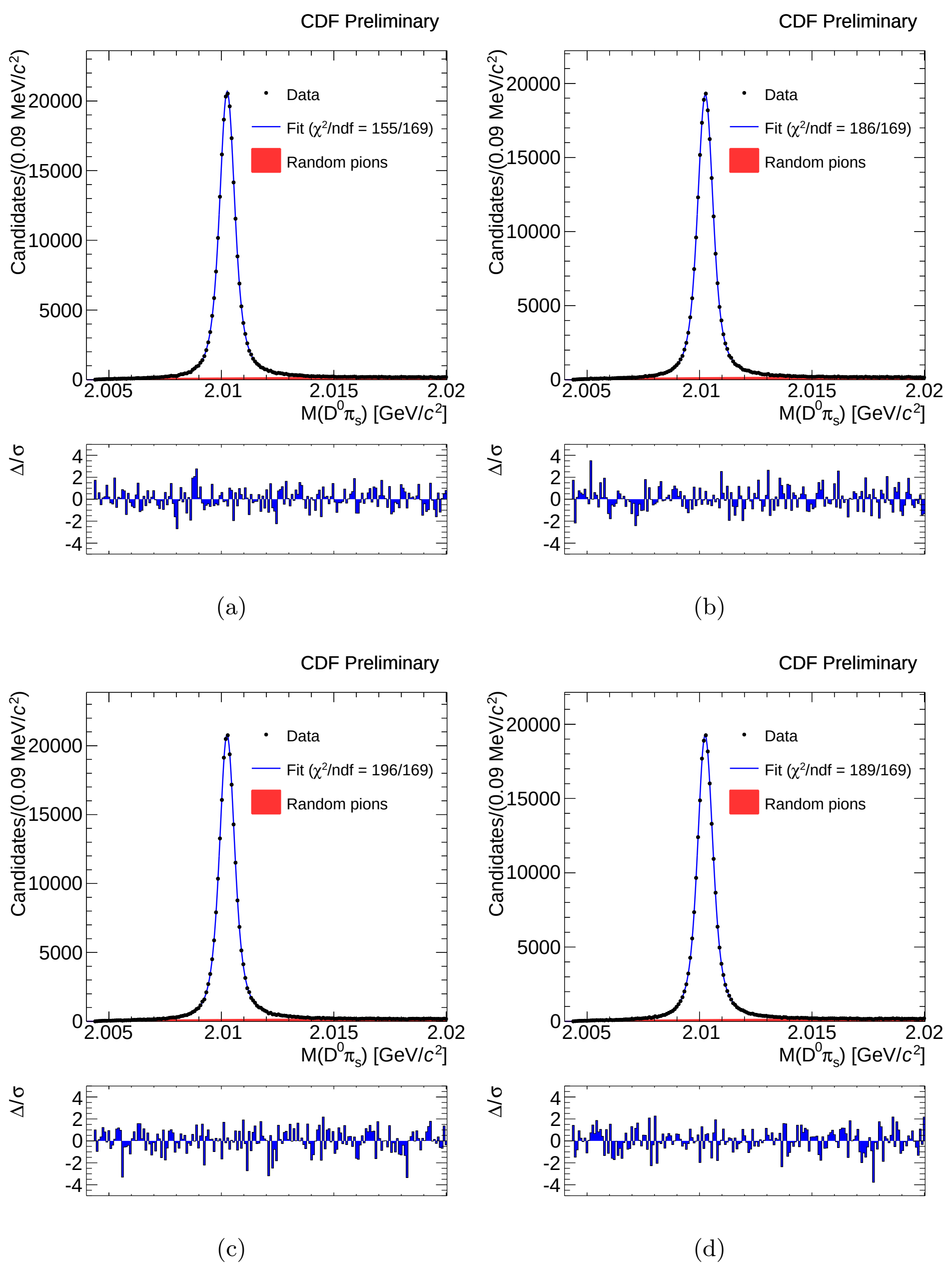

Figure 82: $D^0\pi_s$–mass distributions of (a,c) $D^{*-} \rightarrow \overline{D}^0(\rightarrow K^-\pi^+)\pi_s^-$ and (b,d) $D^{*+} \rightarrow D^0(\rightarrow K^-\pi^+)\pi_s^+$ candidates restricted in the decay-time bin (a,b) 8 ($1.84\tau < t < 1.92\tau$), and (c,d) 9 ($1.92\tau < t < 2.00\tau$), with fit projections overlaid.

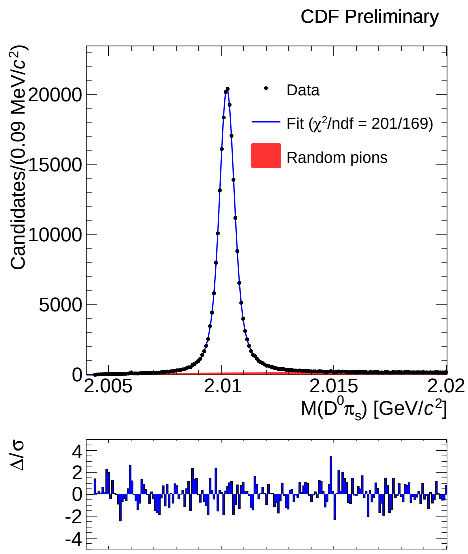

(a)

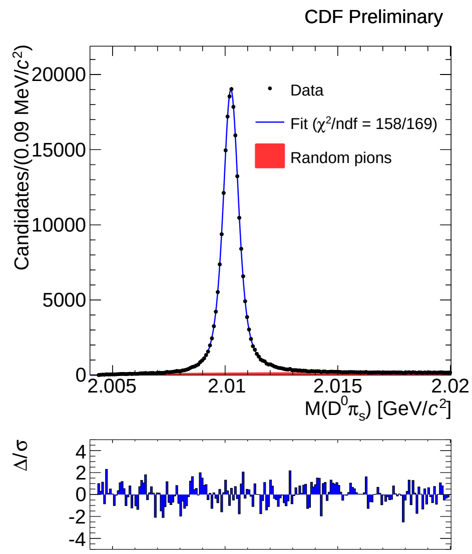

(b)

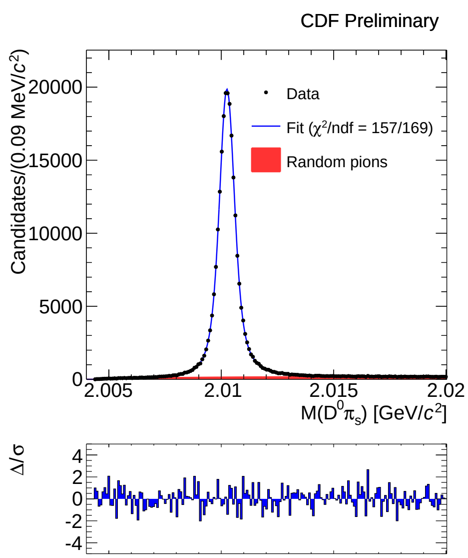

(c)

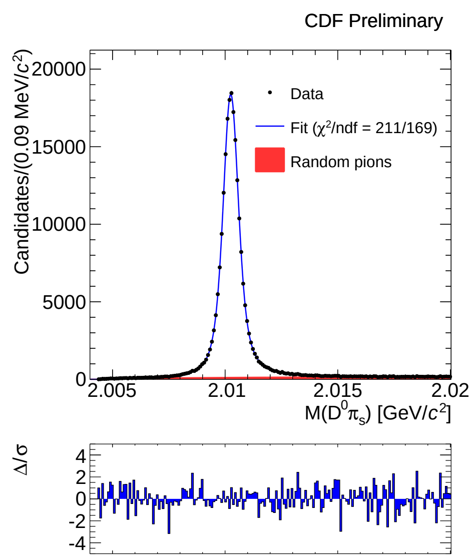

(d)

Figure 83: $D^0\pi_s$–mass distributions of (a,c) $D^{*-} \to \overline{D}^0(\to K^-\pi^+)\pi_s^-$ and (b,d) $D^{*+} \to D^0(\to K^-\pi^+)\pi_s^+$ candidates restricted in the decay-time bin (a,b) 10 ($2.00\tau < t < 2.08\tau$), and (c,d) 11 ($2.08\tau < t < 2.16\tau$), with fit projections overlaid.

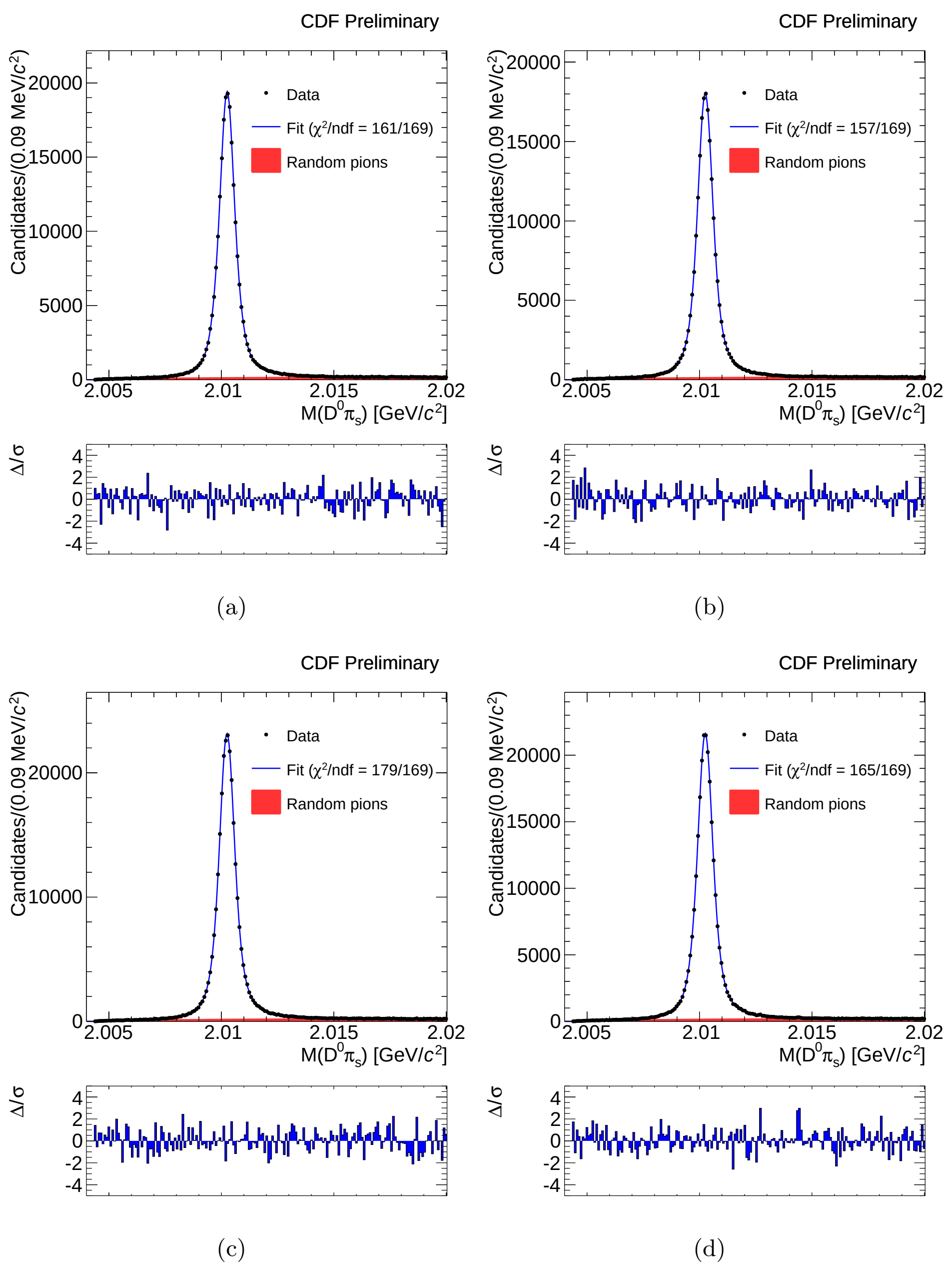

Figure 84: $D^0\pi_s$–mass distributions of (a,c) $D^{*-} \to \overline{D}^0(\to K^-\pi^+)\pi_s^-$ and (b,d) $D^{*+} \to D^0(\to K^-\pi^+)\pi_s^+$ candidates restricted in the decay-time bin (a,b) 12 ($2.16\tau < t < 2.24\tau$), and (c,d) 13 ($2.24\tau < t < 2.34\tau$), with fit projections overlaid.

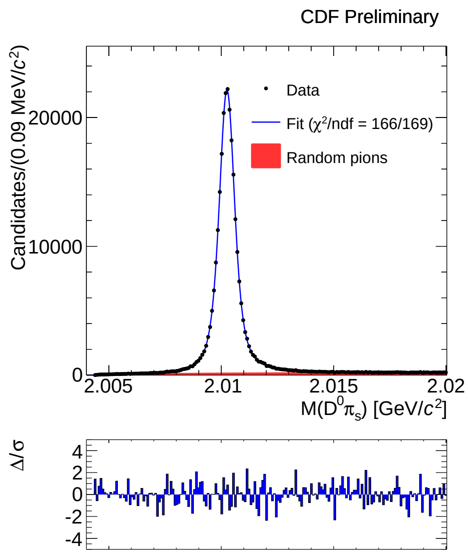

(a)

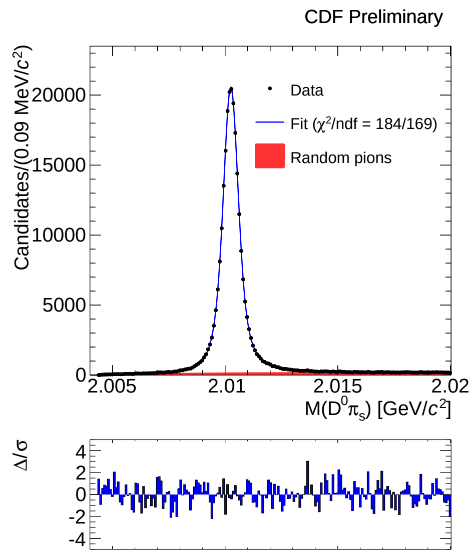

(b)

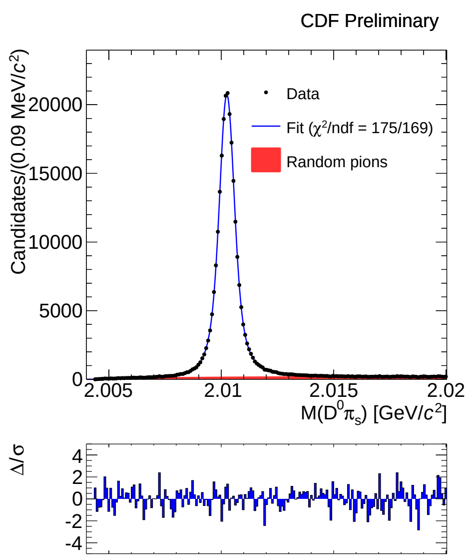

(c)

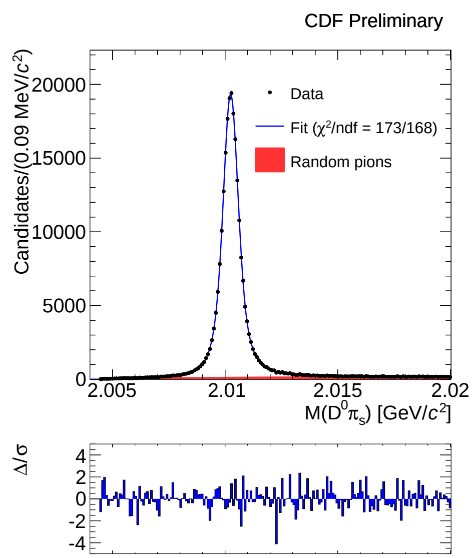

(d)

Figure 85: $D^0\pi_s$–mass distributions of (a,c) $D^{*-} \to \overline{D}^0(\to K^-\pi^+)\pi_s^-$ and (b,d) $D^{*+} \to D^0(\to K^-\pi^+)\pi_s^+$ candidates restricted in the decay-time bin (a,b) 14 ($2.34\tau < t < 2.44\tau$), and (c,d) 15 ($2.44\tau < t < 2.54\tau$), with fit projections overlaid.

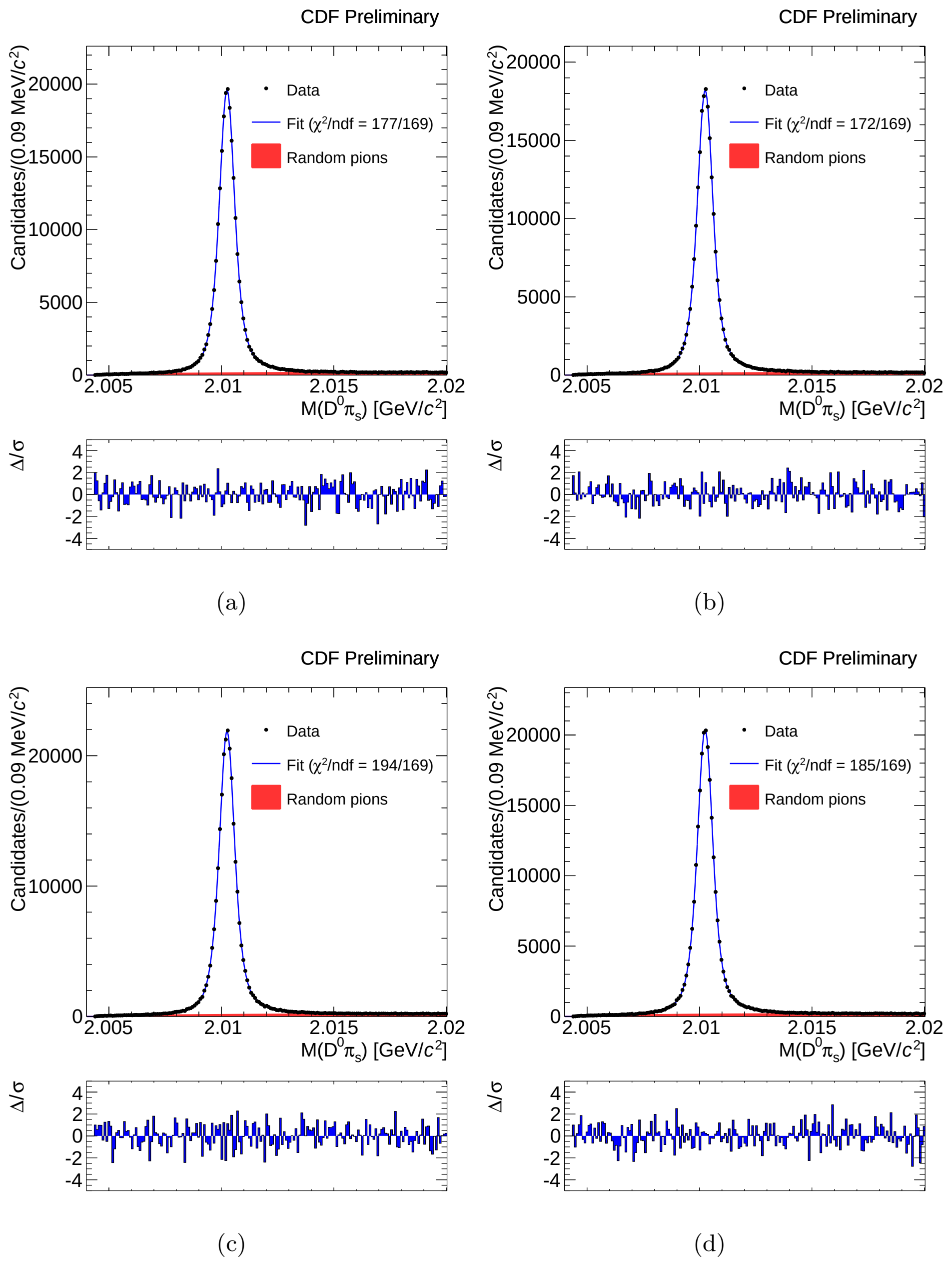

Figure 86: $D^0\pi_s$–mass distributions of (a,c) $D^{*-} \to \overline{D}^0(\to K^-\pi^+)\pi_s^-$ and (b,d) $D^{*+} \to D^0(\to K^-\pi^+)\pi_s^+$ candidates restricted in the decay-time bin (a,b) 16 ($2.54\tau < t < 2.64\tau$), and (c,d) 17 ($2.64\tau < t < 2.76\tau$), with fit projections overlaid.

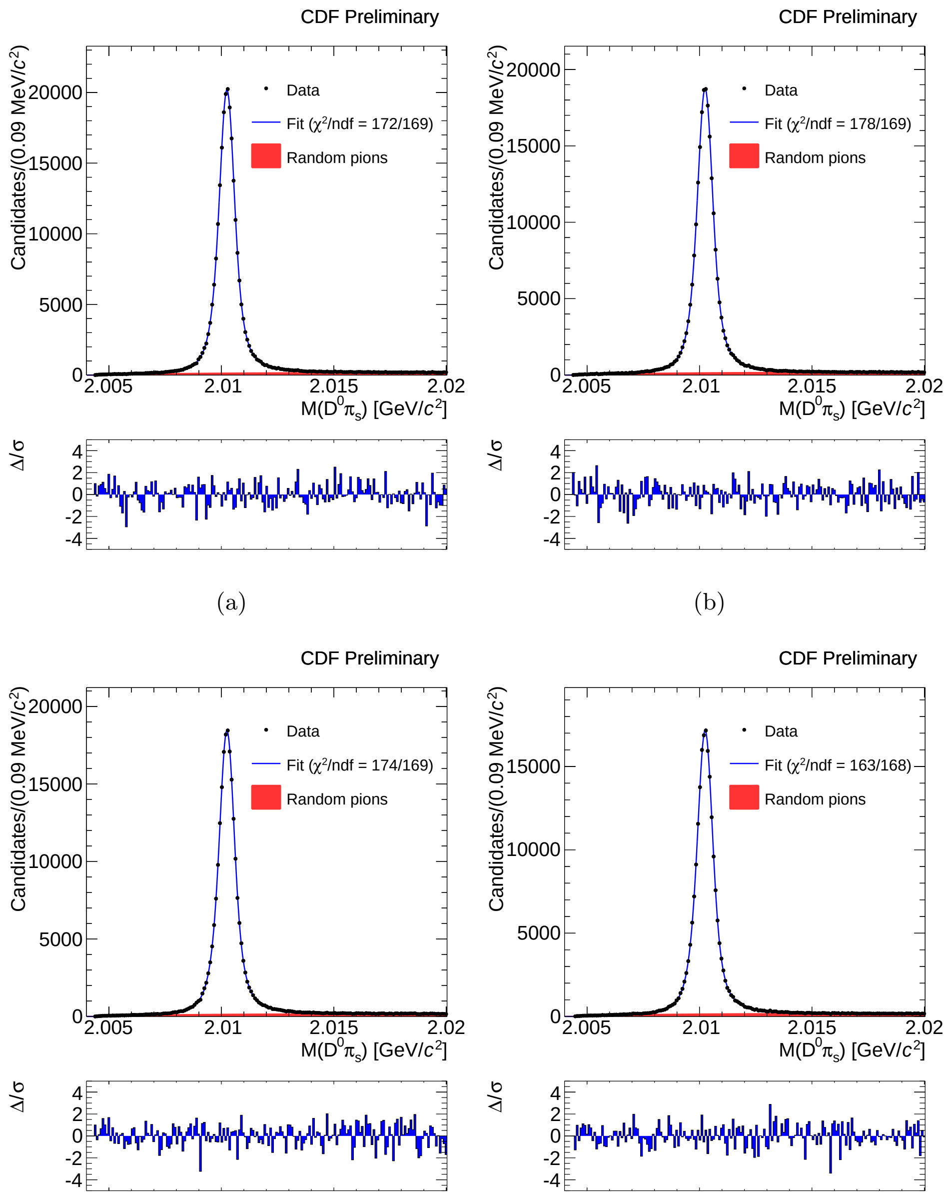

Figure 87: $D^0\pi_s$–mass distributions of (a,c) $D^{*-} \to \overline{D}^0(\to K^-\pi^+)\pi_s^-$ and (b,d) $D^{*+} \to D^0(\to K^-\pi^+)\pi_s^+$ candidates restricted in the decay-time bin (a,b) 18 ($2.76\tau < t < 2.88\tau$), and (c,d) 19 ($2.88\tau < t < 3.00\tau$), with fit projections overlaid.

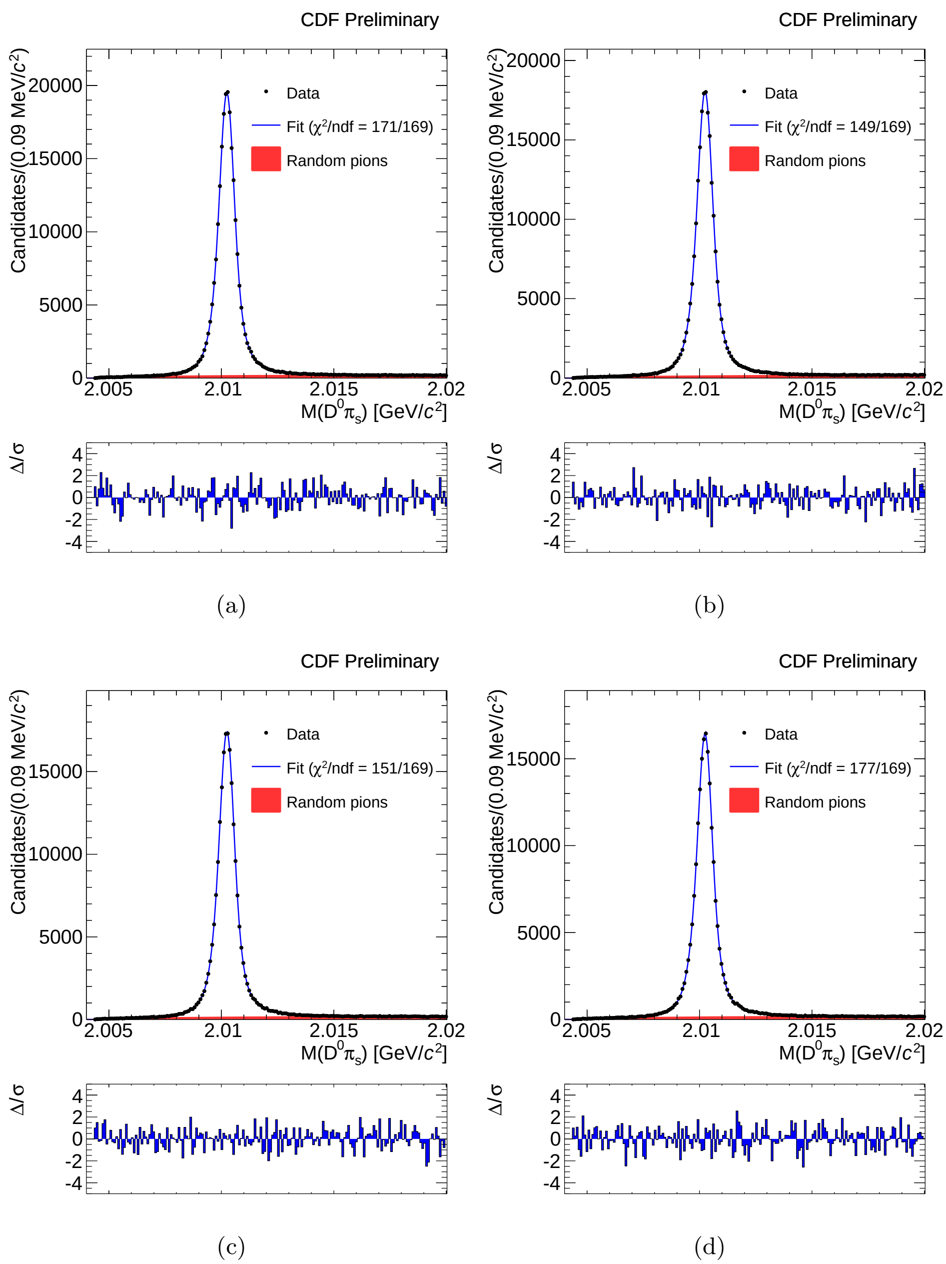

Figure 88: $D^0\pi_s$–mass distributions of (a,c) $D^{*-} \rightarrow \overline{D}^0(\rightarrow K^-\pi^+)\pi_s^-$ and (b,d) $D^{*+} \rightarrow D^0(\rightarrow K^-\pi^+)\pi_s^+$ candidates restricted in the decay-time bin (a,b) 20 ($3.00\tau < t < 3.14\tau$), and (c,d) 21 ($3.14\tau < t < 3.28\tau$), with fit projections overlaid.

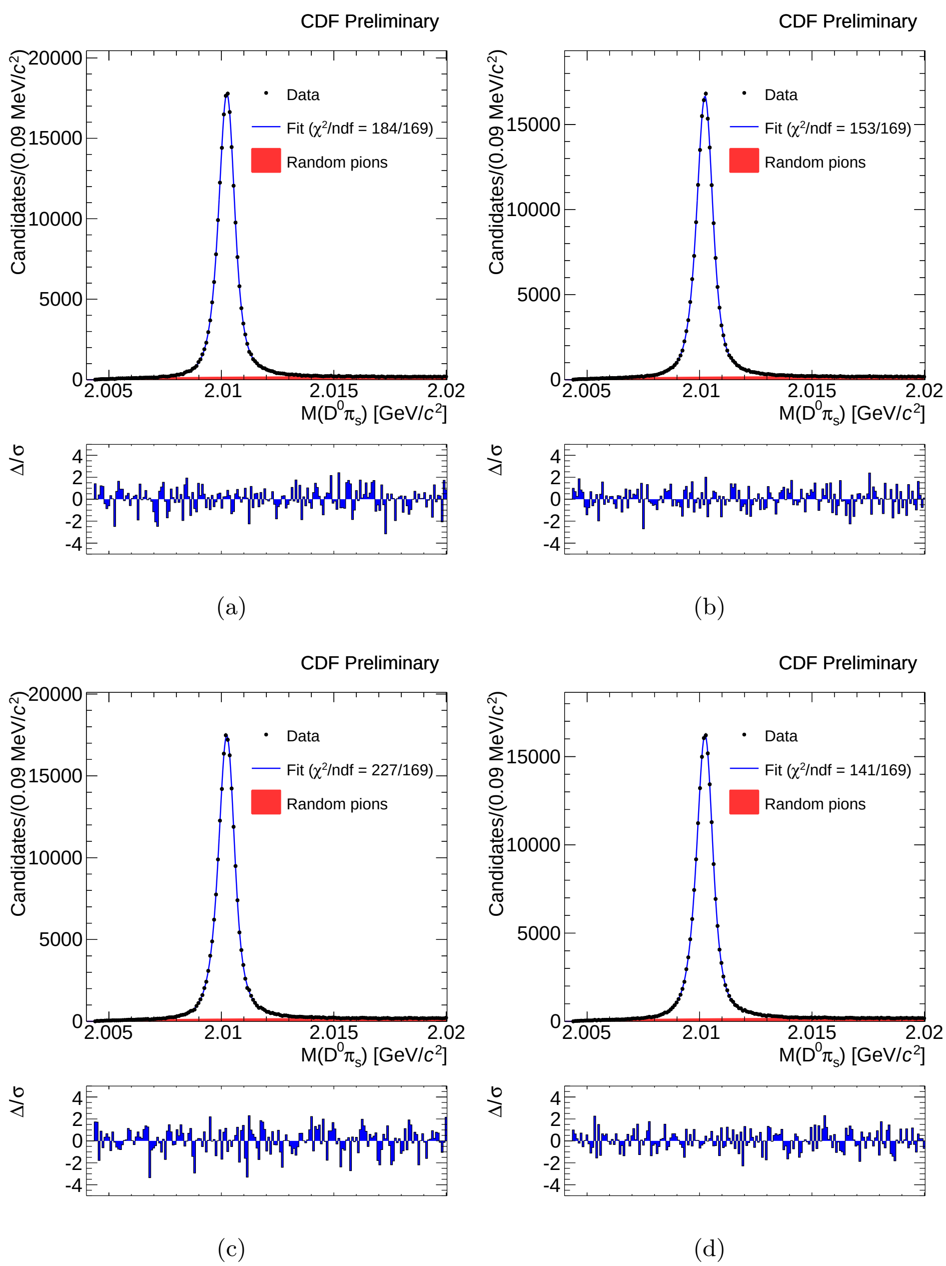

Figure 89: $D^0\pi_s$–mass distributions of (a,c) $D^{*-} \to \overline{D}^0(\to K^-\pi^+)\pi_s^-$ and (b,d) $D^{*+} \to D^0(\to K^-\pi^+)\pi_s^+$ candidates restricted in the decay-time bin (a,b) 22 ($3.28\tau < t < 3.44\tau$), and (c,d) 23 ($3.44\tau < t < 3.62\tau$), with fit projections overlaid.

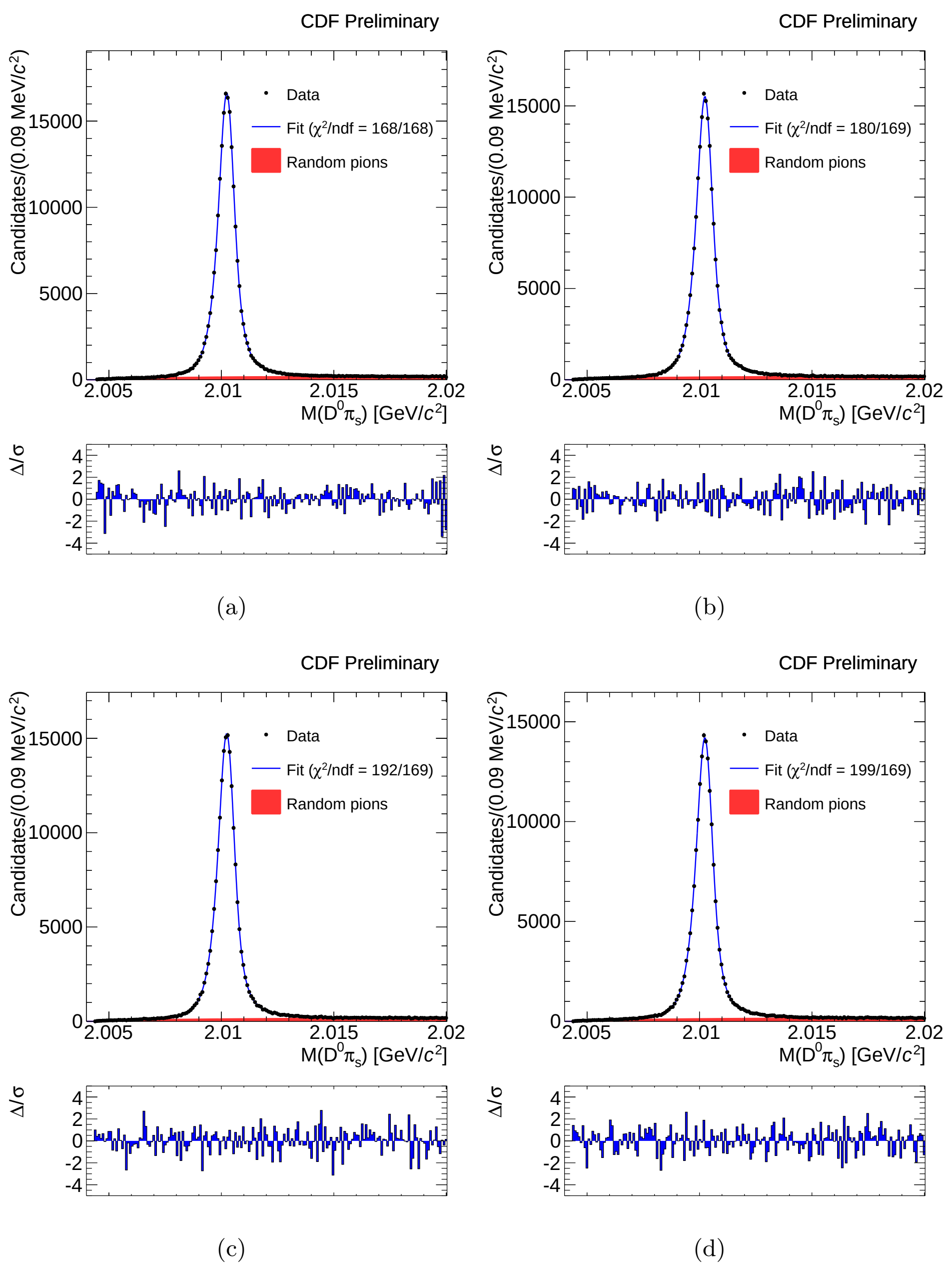

Figure 90: $D^0\pi_s$–mass distributions of (a,c) $D^{*-} \to \overline{D}^0(\to K^-\pi^+)\pi_s^-$ and (b,d) $D^{*+} \to D^0(\to K^-\pi^+)\pi_s^+$ candidates restricted in the decay-time bin (a,b) 24 ($3.62\tau < t < 3.82\tau$) and (c,d) 25 ($3.82\tau < t < 4.04\tau$), with fit projections overlaid.

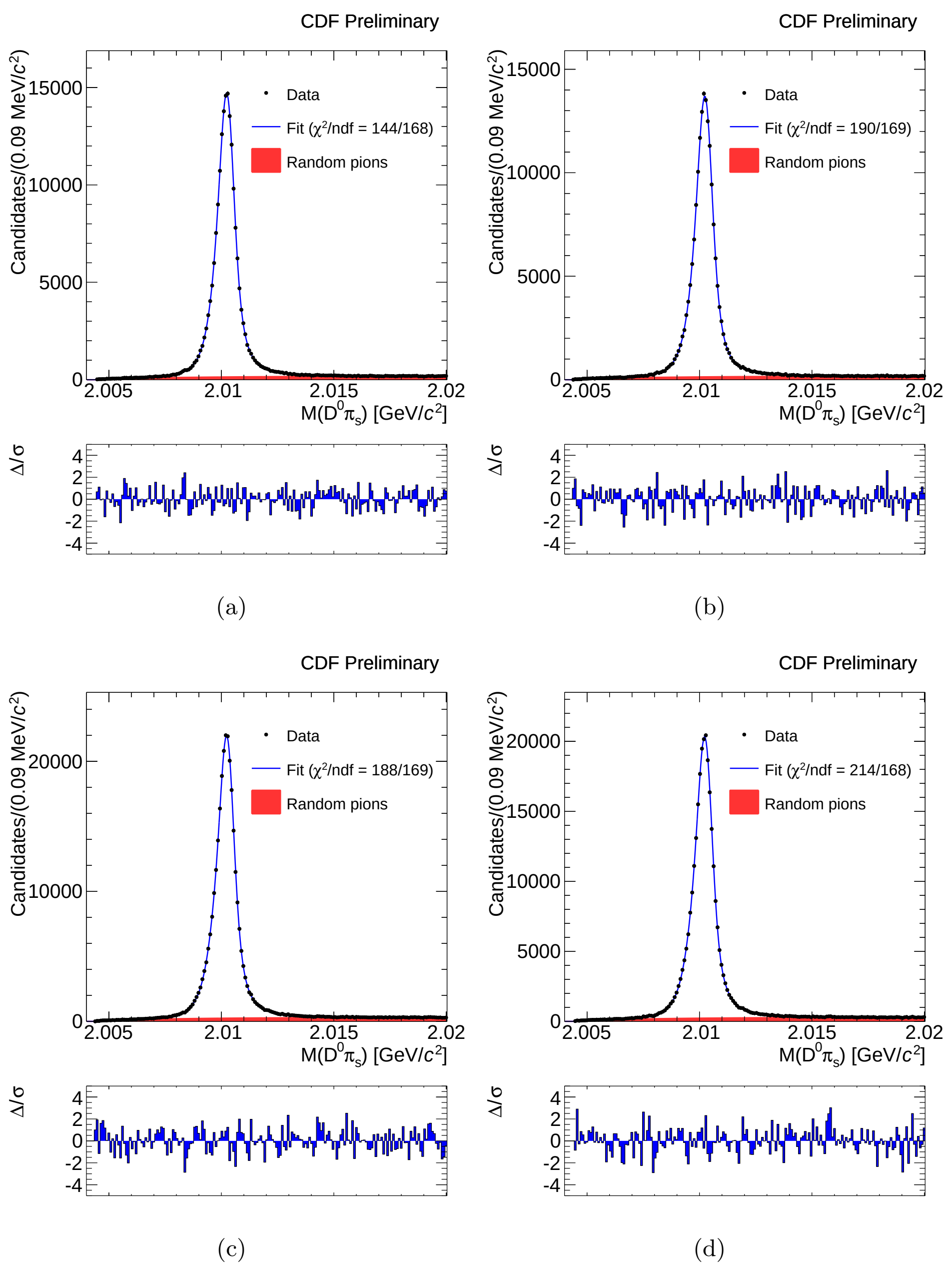

Figure 91: $D^0\pi_s$–mass distributions of (a,c) $D^{*-} \to \overline{D}^0(\to K^-\pi^+)\pi_s^-$ and (b,d) $D^{*+} \to D^0(\to K^-\pi^+)\pi_s^+$ candidates restricted in the decay-time bin (a,b) 26 ($4.04\tau < t < 4.30\tau$) and (c,d) 27 ($4.30\tau < t < 4.98\tau$), with fit projections overlaid.

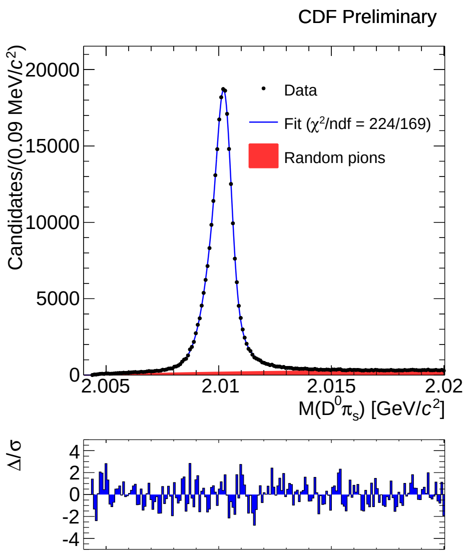

(a)

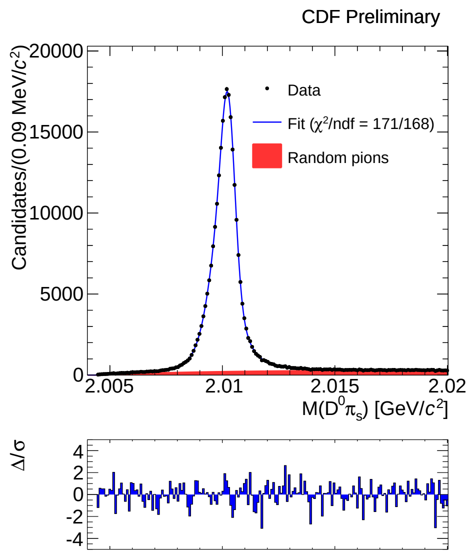

(b)

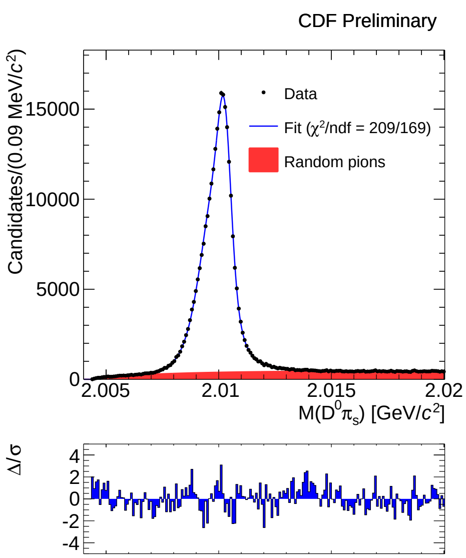

(c)

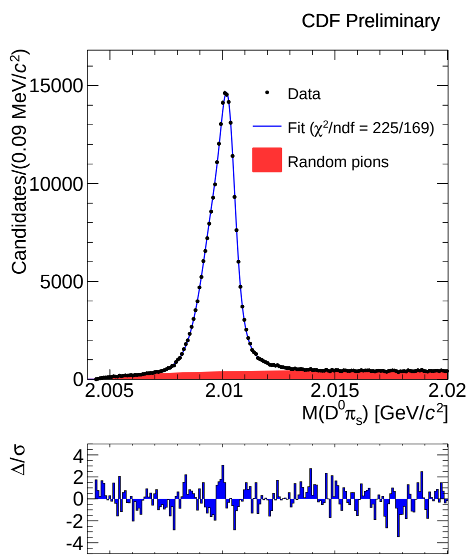

(d)

Figure 92: $D^0\pi_s$–mass distributions of (a,c) $D^{*-} \to \overline{D}^0(\to K^-\pi^+)\pi_s^-$ and (b,d) $D^{*+} \to D^0(\to K^-\pi^+)\pi_s^+$ candidates restricted in the decay-time bin (a,b) 28 ($4.98\tau < t < 6.16\tau$) and (c,d) 29 ($6.16\tau < t < 20\tau$), with fit projections overlaid.